

Trinity Term 2024

An Advanced Single Cell Surgery Photonics Platform

Seung-Bin Joo, Sean Mata, Alexander Peake, Xianming Liu, Tom Sharrock

Contents		
1 Introduction - Tom Sharrock	2	5.1 Phase-Contrast Microscopy 65 5.2 Camera sensor 77 5.3 Image Processing 81 5.4 Input To the CARS System 90 5.5 Summary 90
2 Optical tweezer system - Seung-Bin Joo	5	
2.1 Optical tweezer system design	5	
2.2 Optical trapping with Brownian motion	19	
2.3 Holographic optical tweezing	24	
2.4 Cost estimation for the optical tweezer system	33	
2.5 Summary	33	
3 Optical Tweezer dynamics and trajectory planning - Sean Mata	34	6 Chemical imaging system - Xianming Liu 92
3.1 Introduction	34	6.1 Introduction to Design Specifications 92 6.2 Overview of Microscopy Techniques and Limitations: 93
3.2 Dynamics of the optical tweezing . .	34	6.3 Working Principle of CARS Mi- croscopy System 95
3.3 Parameter uncertainty	39	6.4 Example Spectra 99
3.4 Trapping stiffness calibration	39	6.5 Optical layout of our CARS system . 101
3.5 Optical Tweezer Trajectory Planning	41	6.6 Cost Estimation 116
3.6 Summary	47	6.7 Safety Consideration 116
4 Laser ablation system - Sean Mata	48	6.8 Summary 117
4.1 Introduction	48	7 XY Control - Tom Sharrock 118
4.2 Design specification	49	7.1 Design Objectives of XY Control . 118
4.3 System overview/Optical Layout . .	49	7.2 XY Coarse-Control 119
4.4 Laser parameter analysis	52	7.3 XY Fine Control 120
4.5 Bessel beam analysis	58	7.4 Fine-Control Stage Mechanism Dy- namics 122
4.6 Safety Considerations	62	7.5 Finite Element (FE) Analysis of Stage Design 129
4.7 Summary	63	7.6 XY Controller Design 132
5 Widefield Imaging System - Alexander Peake	64	7.7 Z Control 141
		7.8 Control Costs 144
		7.9 Control System Summary 144
		8 Conclusion - Xianming Liu 145

1 Introduction - Tom Sharrock

Light is an incredibly versatile tool with a huge range of applications, ranging from optical sensing and measurement to laser processing and fabrication. An area with huge scope and current development is the micro-manipulation of biological matter: the ability to operate on individual cells using lasers. This 'single cell surgery' is novel as each cell in an in vitro sample is considered in isolation, providing unparalleled potential in genetic engineering, cellular cancer studies, and biomedicine. For instance, laser-based single cell surgery has been applied to fusion of embryonic cells [1], insertion of fetal mitochondria into adult cells for anti-aging gene expression [2], and cutting of chromosomes to understand its effects on cells and larger organisms [3].

Whilst successful, previously developed single cell surgery platforms have significant limitations. For example, some platforms are only able to manipulate cells (no drug or DNA delivery capabilities), whereas others lack control of exactly how much of a drug is delivered, relying on passive diffusion. This report, however, presents a novel, purpose-designed photonics platform that combines multiple techniques: our system is able to create micrometre-sized holes in cells, into which drug- or plasmid-coated microparticles are inserted. Thus, we will control exactly which particles, and how many, are inserted into any specific cell. Subsequently, we will use chemical spectroscopy imaging techniques to ensure successful operation. Our system is designed to operate on human, animal, and plant cells ranging from 20 to $30\mu m$ in diameter. A variety of cells such as human red blood cells, white blood cells, embryonic stem cells, lymphocytes, neurons, and some types of cancer cells are within this size range, giving our platform a wide array of applications.

An overview of the operation process is presented in Figure 1. Firstly, a femtosecond laser ablates the cell membrane, creating an opening for $2\mu m$ diameter microparticles to be inserted. The microparticles are then maneuvered into the desired cell using a separate optical 'tweezer' laser system. In the case of drug delivery or genetic engineering, the particles are coated with drug molecules or plasmids (strands of DNA molecule), so a controlled, known quantity is inserted. While the analysis assumes the use of these microparticles, our platform may also insert, for example, mitochondria and organelles. For our analysis here, we have chosen to use a transparent petri dish with a grid of many $50 \times 50\mu m$ squares, each containing a cell fixed to the bottom of the dish. They are submerged in a cell culture medium with the microparticles suspended randomly around.

A phase contrast microscope allows wide-field live-imaging of the cells and determines the positions of cells in the sample during the insertion process. Exploiting the scattering properties of different chemical compounds, the chemical imaging system obtains high-resolution images of the sample without requiring the addition of contaminating and damaging fluorescent dyes. These images are used to confirm the success of particle delivery into the cells. A purpose-designed, dual-stage control mechanism is presented, incorporating a robust, noise-rejecting controller, which provides nanometer-resolution positioning of the sample in three degrees of freedom. All these aspects are designed to maximise speed, cell viability and insertion efficiency, combining in parallel into an autonomous system with unique capabilities and precision. The complete optical layout is displayed in Figure 2.

The rest of the report is organised as follows. Section 2 details the optical tweezer system design and how multiple particles are trapped at once, whilst being robust to the effects of Brownian motion. This is complemented by Section 3, which specifies a calibration procedure for the optical traps and the planning for the stable trajectory of the particles. Creating a hole in the cell membrane for particles to be inserted into is explained in Section 4. The widefield imaging process of detecting particle positions in real time is developed in Section 5, and the chemical imaging system used to confirm the success of operation is discussed in Section 6. Designing a precision stage mechanism is detailed in Section 7, along with a robust controller. Finally, the findings are summarised in Section 8.

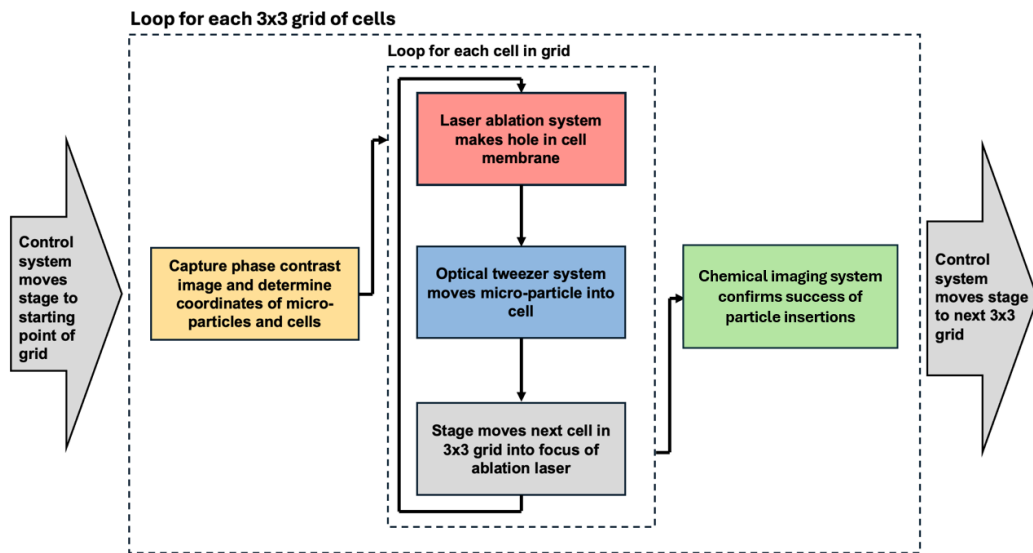


Figure 1: A simplified, overall process flow diagram of our system. It displays how each aspect of the operation relates to the others. Phase contrast imaging system is able to view 9 cells at a time (3×3 grid), so the stage must reposition for each grid. Laser ablation and optical tweezing operate on each cell within a grid.

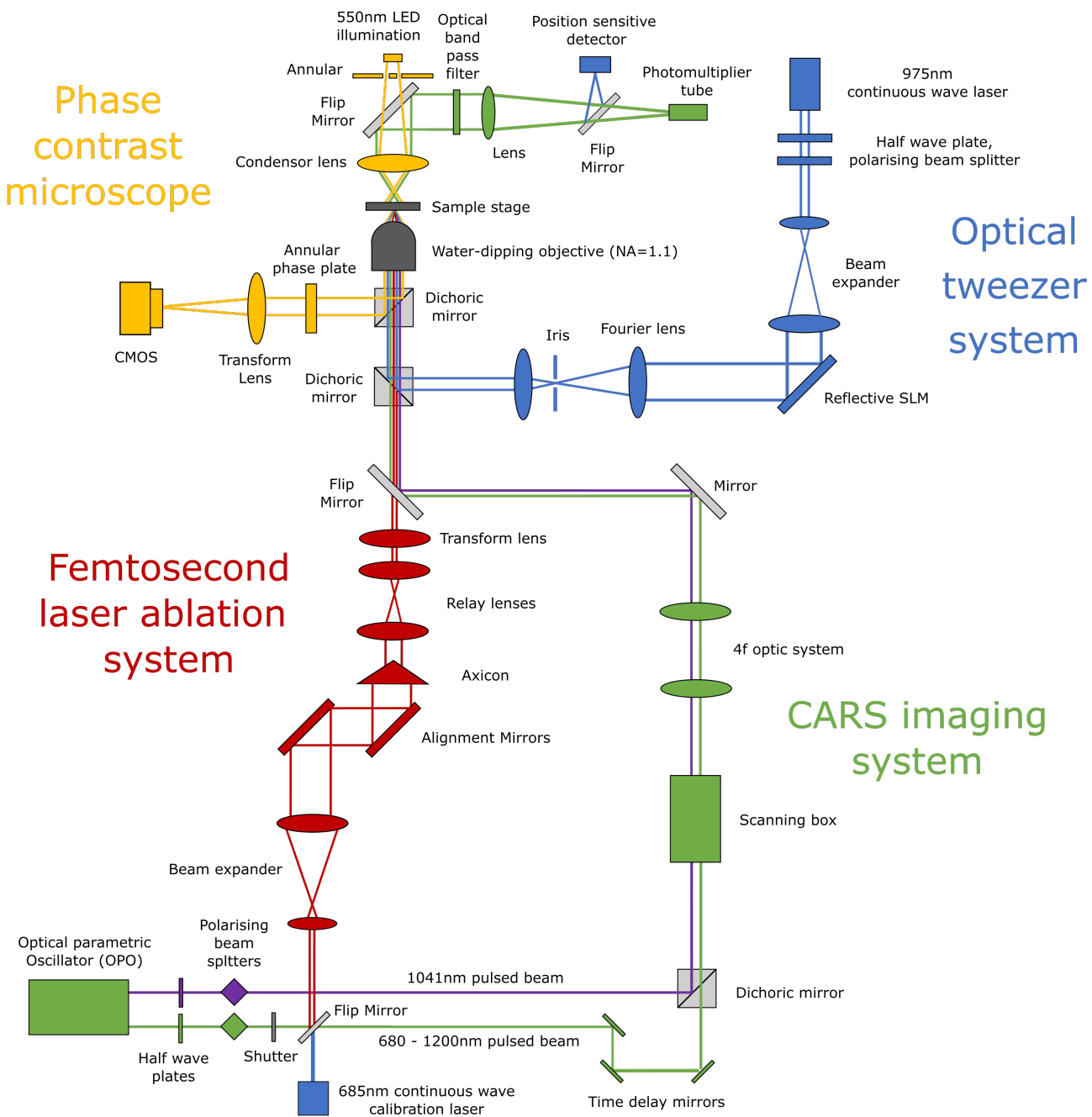


Figure 2: Our designed optical layout for an advanced cell surgery platform. It comprises several different subsystems that will be described in detail throughout this report.

2 Optical tweezer system - Seung-Bin Joo

2.1 Optical tweezer system design

Optical tweezing is a technique that generates 'optical traps' by tightly focusing a laser beam onto a diffraction-limited spot [4]. The optical traps allow us to hold, rotate, or manipulate microscopic particles. In our single cell surgery platform, the optical tweezer system aims to move the drug or plasmid-coated polystyrene microparticles into the cell, via the ablated hole. To ensure successful particle insertion into the cell, we require that the system fulfills the following design criteria:

1. **Sufficient trapping force, efficiency, and stiffness:** For the microparticle to remain stable and inside the optical trap, the trapping force, efficiency, and stiffness must be large enough in all three spatial dimensions. In particular, based on empirical values associated with stable trapping for micron-sized beads [5, 6, 7, 8], we require a trapping stiffness in the range of $0.5 \text{ pN}/\mu\text{m}$ to $25 \text{ pN}/\mu\text{m}$ in all directions (trapping stiffness is defined in Section 2.1.1). In the design process, we determine suitable values for numerical aperture, objective lens aperture size, beam radius at lens, and beam modes, and subsequently, validate that these chosen parameters satisfy the above design criteria using MATLAB optical trap simulations.
2. **Minimisation of photodamage:** A major application of the single cell surgery platform is for biomedical researchers to study how inserting plasmids, proteins, enzymes, etc. affects cell health. However, accurate studies cannot be carried out if our optical tweezing process causes noticeable deterioration of cell health. Since laser absorption by the cell sample can lead to photodamage [9], it is paramount to select the appropriate laser wavelength and power to reduce this effect. Thus, aiming for the optical tweezing to cause negligible photodamage, we require that the tweezing maintains approximately 100% cell cloning efficiency (an indicator of cell health).
3. **Stable trapping in the presence of Brownian motion:** Since the polystyrene microparticles are submerged in a cell culture fluid, random forces from surrounding molecules colliding with the particle will lead to fluctuations in particle position, i.e. Brownian motion. The designed optical trap must confine the particle within a volume small enough such that it can be inserted through the ablated hole. Given the hole diameter is predicted to be $3 \mu\text{m}$ (Section 4.4.5), and our particle diameter is $2 \mu\text{m}$, for successful insertion, the particle centre must remain inside a $1 \mu\text{m}$ -diameter sphere.
4. **Simultaneous and dynamic tweezing:** The system aims to perform optical tweezing on a 3x3 grid

(a $180 \mu\text{m} \times 180 \mu\text{m}$ field of view as discussed in Section 5.1.6) within the sample petri dish, where each grid square contains a cell. Thus, our system must generate 9 optical traps simultaneously. The traps must also be dynamic such that once a particle is confined, the trap must be able to move towards the ablated hole to achieve insertion.

We will now explore the design of a system that satisfies all four of the above criteria. The layout of the designed optical tweezer system is shown below in Figure 3. As an overview, a 975 nm continuous wave laser beam is passed through a half wave plate and polarising beam splitter to allow for laser power control. Subsequently, the beam is expanded to fill the active space of the reflective spatial light modulator (SLM). The SLM and Fourier lens setup allow us to multiplex the single beam into numerous independently controllable beams. Finally, the light is then reflected off a dichroic mirror and focused through the objective lens to create optical traps that manipulate the microparticles on the sample stage.

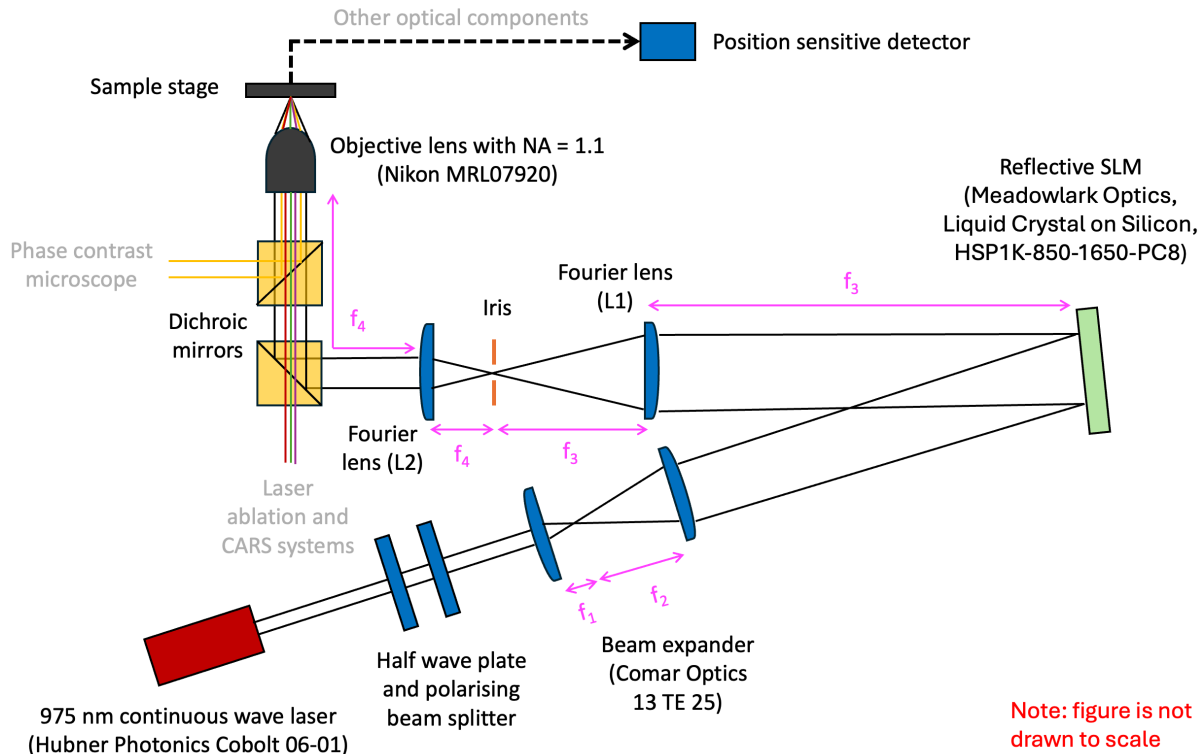


Figure 3: Layout of the designed optical tweezer system.

2.1.1 Principles of optical tweezing

Before delving into details of the system design, it is important to understand the basic principles of optical tweezing. Using a high numerical aperture (i.e. high focusing angle) objective, optical tweezers focus laser beams into optical traps—potential wells that attract microparticles whose refractive indices are greater than that of the surrounding medium [10]. As shown in Figure 4, the equilibrium position of a

trapped particle, i.e. the trap centre, is located near the beam's focal point. For small displacements from the trap centre, the particle experiences a trapping (restoring) force proportional to displacement. Thus, we can define *trap stiffnesses* κ in 3 spatial dimensions, and describe the optical trap using Hooke's law:

$$F_x = -\kappa_x(x - x_{eq}) \quad (1)$$

$$F_y = -\kappa_y(y - y_{eq}) \quad (2)$$

$$F_z = -\kappa_z(z - z_{eq}) \quad (3)$$

where $[x, y, z]$ and $[x_{eq}, y_{eq}, z_{eq}]$ are the particle positions and equilibrium positions, respectively.

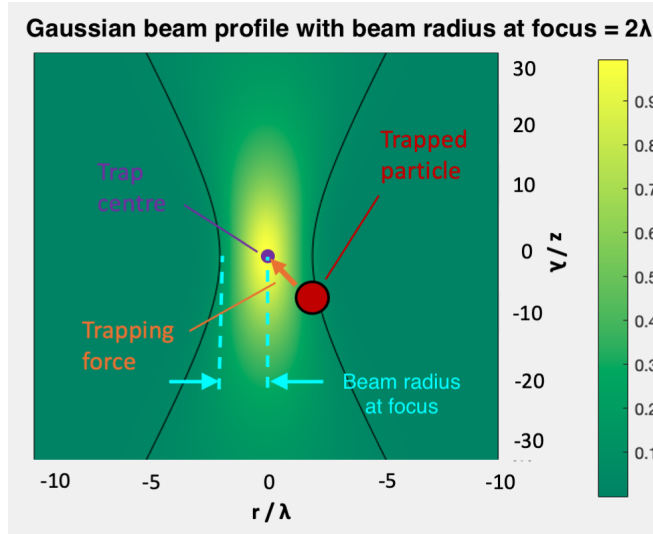


Figure 4: MATLAB Gaussian beam profile simulation overlayed with a theoretical microparticle to demonstrate optical trapping. λ is the laser wavelength. Color bar indicates relative intensity.

The analysis of optical forces $[F_x, F_y, F_z]$ exerted on trapped particles depends on the optical trapping regime [9]. If the radius of the trapped particle a is significantly larger than the wavelength of the trapping laser λ ('ray optics regime' where $\frac{a}{\lambda} \gg 1$), then a ray optics approximation is used to compute optical forces. If the particle radius a is much smaller than λ ('Rayleigh regime' where $\frac{a}{\lambda} \ll 1$), we analyse forces by approximating the particle as a small dipole. Lastly, if a is comparable to λ ('intermediate regime' where $\frac{a}{\lambda} \approx 1$), the aforementioned approximations become less valid, necessitating a full wave-optical modelling of the trapped particle using electromagnetic scattering theory [10]. While our system's use of a 975 nm laser and particles with 1000 nm radii indicates that we operate in the intermediate regime ($\frac{a}{\lambda} \approx 0.975$), the required electromagnetic analysis using Maxwell's stress tensors is far beyond the scope of this project. However, as indicated by the blue line in Figure 5, in some cases, the ray optics approximation-based calculation still relatively closely matches the trapping stiffness derived using the full electromagnetic

theory when $\frac{a}{\lambda} \approx 0.975$. Since our system will use similar refractive indices and NA, we will make the key assumption that our optical tweezing can be modelled using a ray optics approximation.

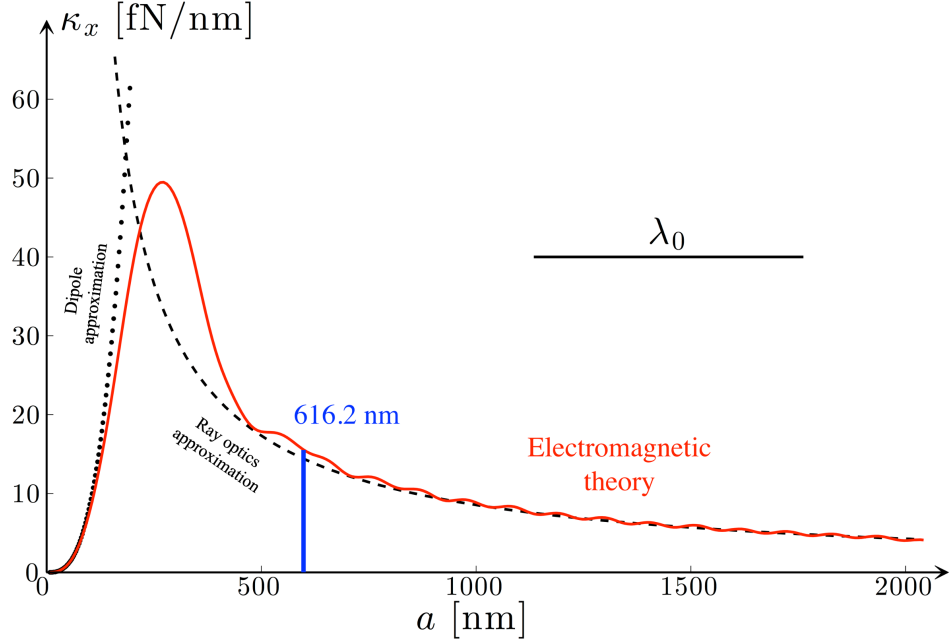


Figure 5: Comparison of theoretical trap stiffness calculation depending on the trapping regime. Plot shows trap stiffness κ_x vs. radius of trapped sphere a (where $\lambda_0 = 632$ nm, NA = 1.20, trapped sphere refractive index $n_p = 1.50$, and refractive index of surrounding medium $n_m = 1.33$). Left and right dotted line indicate trap stiffnesses obtained using dipole and ray optics approximations, respectively. Solid red line indicates exact theoretical trap stiffness based on electromagnetic theory. Blue line indicates where $\frac{a}{\lambda} = 0.975$, i.e. $632 \times 0.975 = 616.2$ nm. Modified and reproduced from Jones et. al [10].

To understand how ray optics can be used to model our system's optical tweezing, we first consider a simpler scenario of a single light ray exerting optical forces on a particle. In Figure 6, an initial light ray \mathbf{r}_i with power P_i is incident on a polystyrene particle at an angle of $\theta_i = 70$ degrees. At the point of incidence, the ray splits into a reflected ray $\mathbf{r}_{r,0}$ and transmitted ray $\mathbf{r}_{t,0}$, with each ray containing a fraction of the power of the initial ray ($P_i = P_t + P_r$). The angles at which the rays are reflected and transmitted are governed by the law of reflection ($\theta_i = \theta_r$) and Snell's law ($n_t \sin \theta_t = n_i \sin \theta_i$). The transmitted ray $\mathbf{r}_{t,0}$ travels across the particle's internal volume until it reaches the sphere boundary, at which point a similar scattering event occurs, producing another reflected ray $\mathbf{r}_{r,1}$ and transmitted ray $\mathbf{r}_{t,1}$. This process of reflection and transmission repeats until all light has asymptotically exited the particle.

For a light ray normally incident on an ideal mirror in direction $\hat{\mathbf{u}}$ with power P , the ideal rate of change of momentum, and hence the ideal optical force, the ray can exert on the mirror is $\frac{2P}{c}\hat{\mathbf{u}}$. Following a similar logic, for non-normal refractive and reflective scattering, the magnitude of the optical force exerted by an

incident ray is $\frac{n_i P_i}{c}$. Thus, the total force a single light ray exerts on the particle is given by summing the optical force contributions from all rays entering or exiting the sphere, and can be expressed as [11]:

$$\mathbf{F}_{ray} = \frac{n_i P_i}{c} \hat{\mathbf{r}}_i - \frac{n_i P_r}{c} \hat{\mathbf{r}}_{r,0} - \sum_{n=1}^{\infty} \frac{n_i P_{t,n}}{c} \hat{\mathbf{r}}_{t,n} \quad (4)$$

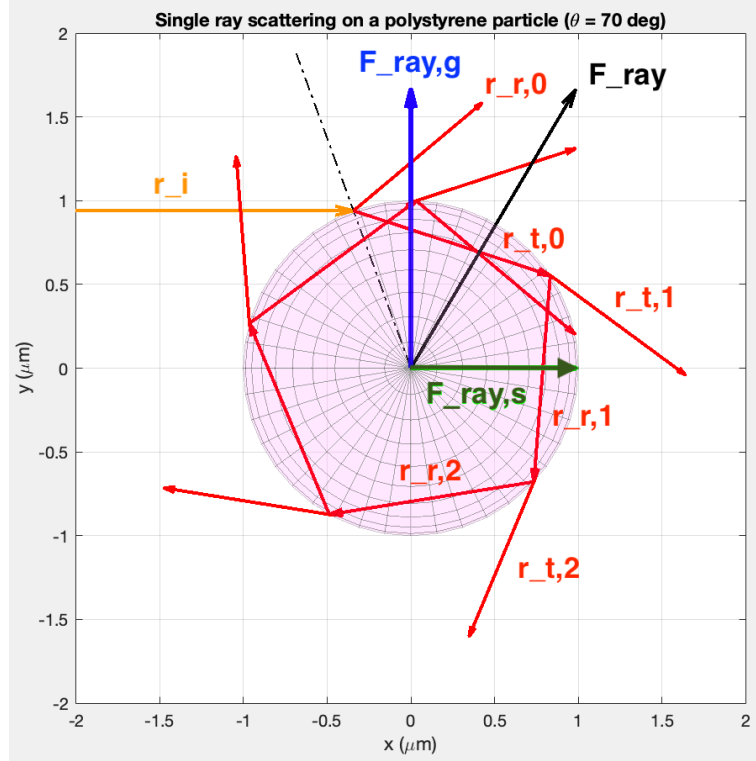


Figure 6: MATLAB simulation of a single ray reflecting and transmitting through a polystyrene particle of radius $1\mu m$. Incoming ray is at angle of incidence $\theta = 70$ deg. Scattering force (dark green), gradient force (blue), and resultant optical force (black) are also shown. MATLAB optics toolbox was used to compute scattering (throughout the optical tweezer section), as well as produce this Figure [11].

As indicated in Figure 6, the resultant optical force \mathbf{F}_{ray} can be decomposed into the gradient force $\mathbf{F}_{ray,g}$ (perpendicular to the initial ray) and the scattering force $\mathbf{F}_{ray,s}$ (parallel to the initial ray). In each direction, we can define dimensionless quantities called trapping efficiencies ($Q_{ray,g}$ and $Q_{ray,s}$) by dividing the magnitudes of the gradient and scattering forces by the maximum achievable optical force $\frac{n_i P_i}{c}$:

$$Q_{ray,g} = \frac{c}{n_i P_i} F_{ray,g} \quad (5)$$

$$Q_{ray,s} = \frac{c}{n_i P_i} F_{ray,s} \quad (6)$$

The overall trapping efficiency is then given by Pythagorean addition: $Q_{ray} = \sqrt{Q_{ray,g}^2 + Q_{ray,s}^2}$.

2.1.2 Ray optics-based optical trap simulation

Based on the above ray optics theory, an optical trap simulation was built in MATLAB. This simulation gives the 3D force vector field corresponding to the optical trap, and is crucial as it motivates numerous design decisions discussed in later sections. To simulate optical tweezing, as shown in Figure 7, a Gaussian beam was first created. The beam is simulated by creating a grid of rays (visualised as red lines in Figure 7), each ray with an associated intensity that corresponds to its $[x, y]$ coordinate within the 2D Gaussian (visualised as the blue surface). The Gaussian beam is passed through a circular iris, and the remaining m rays parallel to the z axis are denoted as $r_p^{(m)}$. In this simulation, we assume the lens is ideal and neglect diffraction and aberration effects. Thus, the effect of the focusing lens is to simply bend the rays $r_p^{(m)}$ to $r_f^{(m)}$, causing the rays to perfectly converge to point O shown in Figure 8.

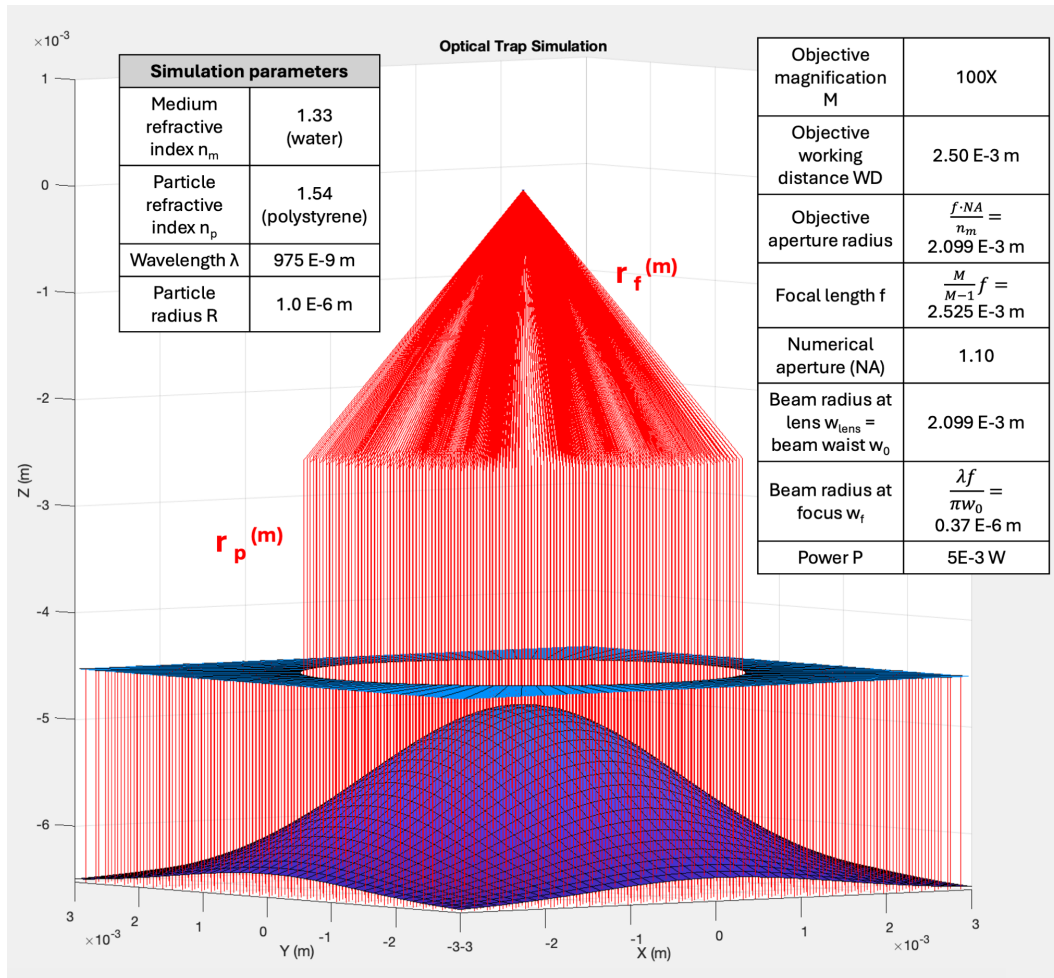


Figure 7: Custom MATLAB 3D simulation of the optical trap created by focusing a Gaussian beam ($NA = 1.10$). The simulation is based on linearly polarised light as we polarise light in one direction in our tweezer system setup. Simulation parameters are shown or calculated in the surrounding tables. $r_p^{(m)}$ and $r_f^{(m)}$ represent m parallel and focused rays, respectively.

The simulation now defines $[x, y, z]$ positions at which to calculate the optical force. For the force vector field shown in Figure 8, the x and y positions were $-1.6R$ to $1.6R$ in $0.32R$ increments, where $R = 1\mu m$ is the polystyrene particle radius. The positions along the z axis were from $-2.4R$ to $2.4R$ in $0.32R$ increments. As a result, this created a $11 \times 11 \times 16$ matrix representing points in $[x, y, z]$ space, which the simulation can iterate through. For each of the 1936 positions in 3D space (e.g. point C_1 in Figure 8), the centre of the polystyrene particle (yellow sphere) is placed at that point. Then, the optical force from one of the focused rays $\mathbf{r}_f^{(1)}$ is computed using Equation 4. The scattering events described by Equation 4 are simulated for 10 iterations or until the power of the scattered rays are 10^{-12} times smaller than the power of the initial ray. Using a loop with m iterations, the optical force from all of the focused rays $\mathbf{r}_f^{(m)}$ (i.e. from the laser beam) is computed and subsequently summed using the following equation [11]:

$$\mathbf{F}_{beam} = \sum_m \mathbf{F}_{ray}^{(m)} = \sum_m \left[\frac{n_i P_i^{(m)}}{c} \hat{\mathbf{r}}_i^{(m)} - \frac{n_i P_r^{(m)}}{c} \hat{\mathbf{r}}_{r,0}^{(m)} - \sum_{n=1}^{\infty} \frac{n_i P_{t,n}^{(m)}}{c} \hat{\mathbf{r}}_{t,n}^{(m)} \right] \quad (7)$$

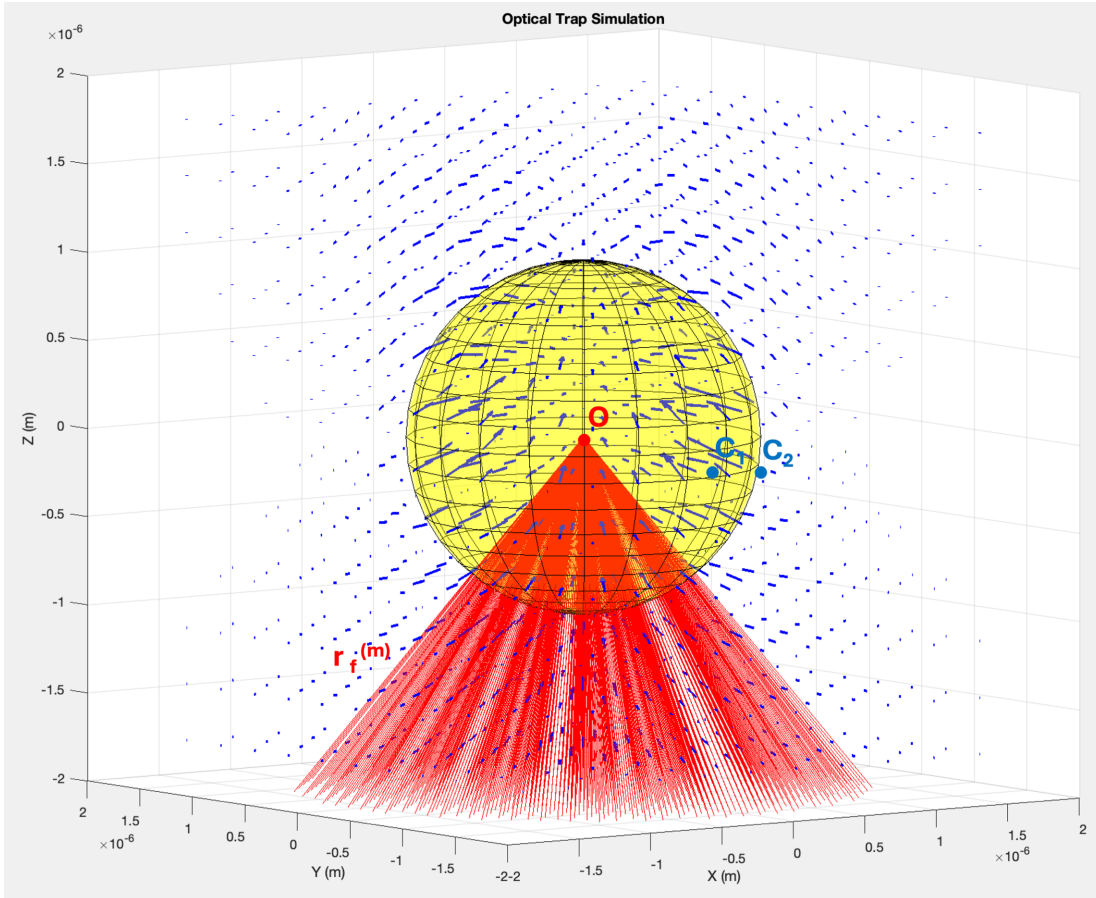


Figure 8: Zoomed in view of custom MATLAB optical trap simulation. The 3D force vector field is also shown as blue arrows. For reference, the polystyrene particle has been displayed and placed at point O .

Once the total optical force from the focused beam is computed, the simulation moves onto the next $[x, y, z]$ position (e.g. C_2), places the particle center at that position, then computes the total optical force resulting from the set of focused rays $\mathbf{r}_f^{(m)}$ using Equation 7. This process repeats for all 1936 points in the $11 \times 11 \times 16$ matrix, and result in the 3D force vector field shown in Figure 8. The blue arrows indicate the direction of the force and the arrow length represent the magnitude.

For our single cell surgery platform, we utilise a polystyrene particle coated with drugs, plasmids, enzymes, and potentially other types of bio-molecules. In this simulation, we assume the coating has negligible effects on the particle's refractive index which is taken to be $n_p = 1.54$. In addition, as detailed in Section 1, our cell samples and polystyrene particles will be submerged in cell culture media, e.g. Dulbecco's Modified Eagle Medium (DMEM). Research suggests that cell culture media such as DMEM have similar refractive indices compared to water [12], and thus, in our simulation we use the medium refractive index $n_m = 1.33$. Other key simulation parameters are listed and calculated in Figure 7.

2.1.3 Objective lens and numerical aperture

We are now ready to delve into the optical tweezer system design. One of the central design parameters of the tweezer and the single cell surgery platform is the numerical aperture (NA) of the objective lens. For the optical tweezers, the NA value can be determined by the following expression:

$$NA = n_m \sin(\theta_{max}) \quad (8)$$

where θ_{max} represents the maximum angle a focused ray $\mathbf{r}_f^{(m)}$ can make with the z axis, i.e. the optical axis. Thus, NA quantifies an objective's ability to create high focusing angle or convergent rays.

To determine the appropriate NA value for our system, the optical trap simulation discussed in Section 2.1.2 was executed for NA values of 0.5, 0.8, and 1.1 (typical values for many commercial objectives). To facilitate visualisation, 2D slices were taken across 3D optical force vector field in the transverse plane (x and y directions such that the plane is perpendicular to the light propagation direction), and in the longitudinal plane (x and z directions such that the plane is parallel to the light propagation direction). Trapping forces along the x and z axis were also plotted. The results are shown in Figure 9.

For all NA values tested, optical trapping in the transverse plane is maintained with sufficiently large gradient forces that range from 4 to 10 pN in magnitude.

However, longitudinal trapping force fields showed significant differences. For a low NA value such as

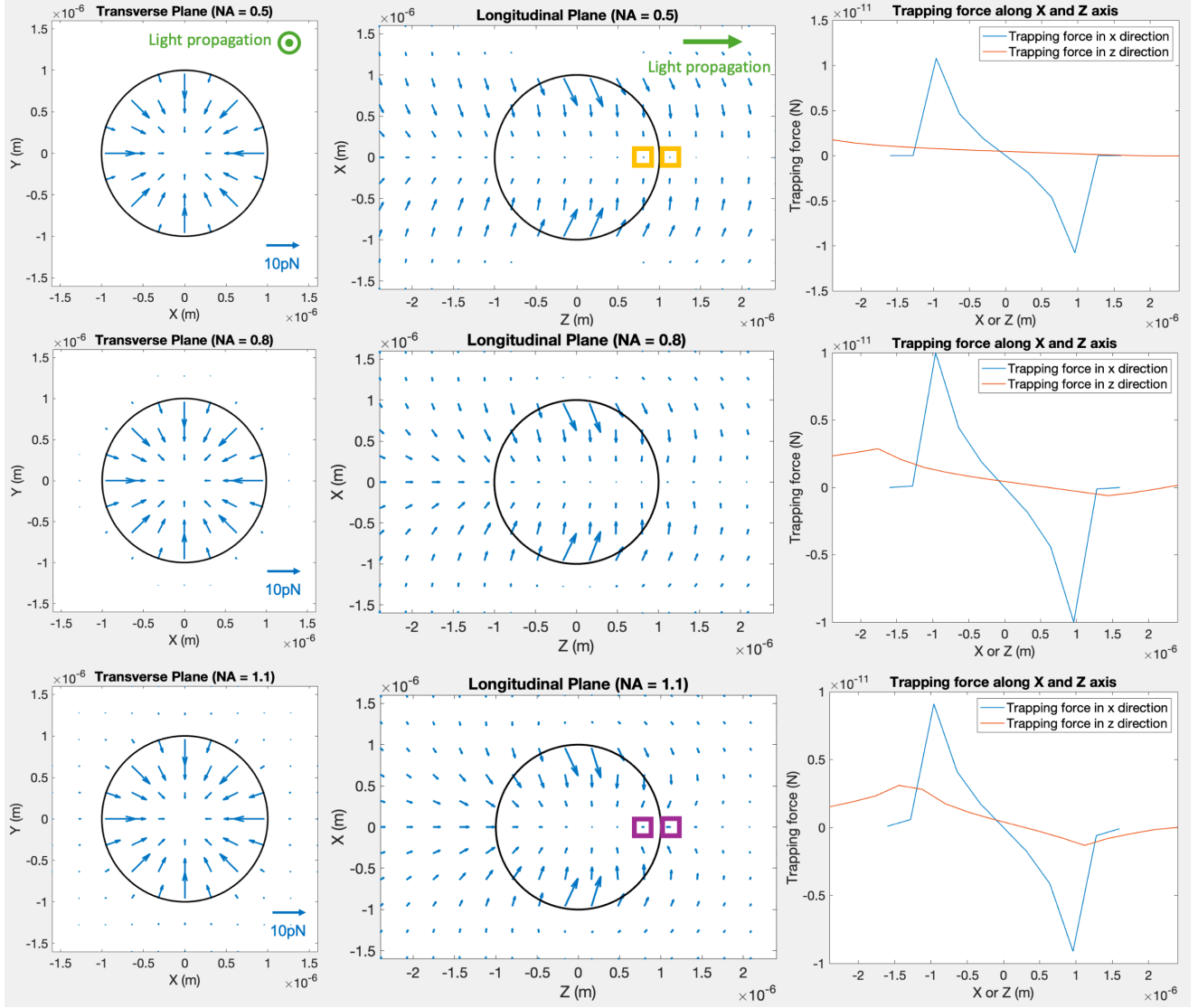


Figure 9: MATLAB simulations of the optical trap and 2D force vector fields in the transverse and longitudinal planes for $NA = 0.5$ (first row), $NA = 0.8$ (second row), and $NA = 1.1$ (third row). Blue arrows indicate force vectors and the green arrow indicates the light propagation direction. Black circle represents the polystyrene particle placed at the focal point, for size reference. Yellow and purple boxes are referred to in the text. Trapping force plots along x and z axes are shown in the last column.

0.5, a significant amount of optical trapping was lost in the axial (z) direction, particularly along the z positions ranging from $+0.2$ to $+0.8\mu m$. For example, the force vectors surrounded by yellow boxes in Figure 9 had small magnitudes of 0.24pN and 0.157pN . These force vectors also pointed away from the trap centre, meaning they pushed the particle away from the trap. Therefore, with $NA = 0.5$, the lack of highly convergent rays means that stable trapping cannot be achieved in the axial direction. With higher NA values of 0.8 and 1.1, the down-beam axial trapping forces are larger and point towards the trap centre, thus achieving longitudinal trapping. However, based on the trapping force plots (rightmost plots

in Figure 9) and Equation 1, the axial (z) trap stiffness for $NA = 0.8$ was $0.4 \text{ pN}/\mu\text{m}$, failing Design Criteria 1 posed in Section 2.1 which requires stiffness to be between 0.5 and $25 \text{ pN}/\mu\text{m}$. $NA = 1.1$ proved to be the optimal case, where the optical forces around $1 \mu\text{m}$ axially down-beam from the trap centre, indicated by the purple boxes, were -0.75 pN and -1.31 pN . The axial trap stiffness ranged from 0.83 to $1.25 \text{ pN}/\mu\text{m}$, and the transversal trap stiffness ranged from 5.83 to $22.8 \text{ pN}/\mu\text{m}$, thus satisfying the design criteria.

Ideally, to achieve higher levels of axial stability in the optical traps, we may consider a NA of 1.2 , 1.3 , or beyond. However, this requires the use of an oil-immersion objective lens. Our objective lens, the Nikon MRL07920 objective, is a component in the single cell surgery platform that is shared by all other subsystems, including the CARS imaging system. As discussed in Section 6.4, since the Raman spectrum of oil overlaps with that of the polystyrene beads, using an high-NA oil-immersion lens would interfere significantly with the CARS imaging process. Thus, NA of 1.1 was chosen so that a highly focused beam would be produced while allowing the use of a water-dipping objective lens.

Referring back to Figure 9, one point to highlight is that in all three NA cases, the trap centre (i.e. the equilibrium position where the force vector is zero), does not lie exactly at the focal point $[0, 0, 0]$. While the trap centre and focal point align in the transverse plane, in the longitudinal plane, the trap centre lies slightly down-beam due to the effect of scattering forces (with the effect being more prominent, the smaller the NA). For the chosen $NA = 1.1$, the trap centre coordinates are $[0, 0, 0.3] \mu\text{m}$.

2.1.4 Beam waist and trapping efficiency

Another important design parameter is the beam waist w_0 , equivalent to the beam radius at the lens w_{lens} . The size of the beam waist influences the amount by which we *fill* the aperture of the objective lens with the incoming beam. To understand why overfilling or underfilling the aperture may affect the trapping, we refer to Ashkin's analytical expressions for gradient and scattering trapping efficiencies when circularly polarised light rays are incident on a sphere [13]:

$$Q_{ray,g} = 1 + R \cos 2\theta - T^2 \frac{\cos(2\theta - 2r) + R \cos 2\theta}{1 + R^2 + 2R \cos 2r} \quad (9)$$

$$Q_{ray,s} = R \sin 2\theta - T^2 \frac{\sin(2\theta - 2r) + R \sin 2\theta}{1 + R^2 + 2R \cos 2r} \quad (10)$$

where θ and r represent the angles of incidence and refraction, and R and T are Fresnel reflection and transmission coefficients [4]. Using these equations to plot the trapping efficiencies against the angle of incidence of light rays, we obtain the plot shown in Figure 10. The plot indicates that the primary

contributors to high trapping efficiencies are the rays that have a high angle of incidence, i.e. the rays originating from the edges of the lens aperture. Although Ashkin's derivations are based on circularly polarised light, and as discussed in Section 2.1.2 and 2.1.6, our simulation and system's laser produce linearly polarised light, a similar principle is still applicable. This is because the beam's central light rays mostly contribute to scattering forces and the rays near the beam's outer edge are responsible for generating gradient forces [5]. Therefore, expanding a Gaussian beam to overfill the aperture of the objective lens allows higher intensity light rays to originate from the aperture edges, leading to a larger ratio of trapping force to scattering force, as well as increased trapping efficiencies [5, 14].

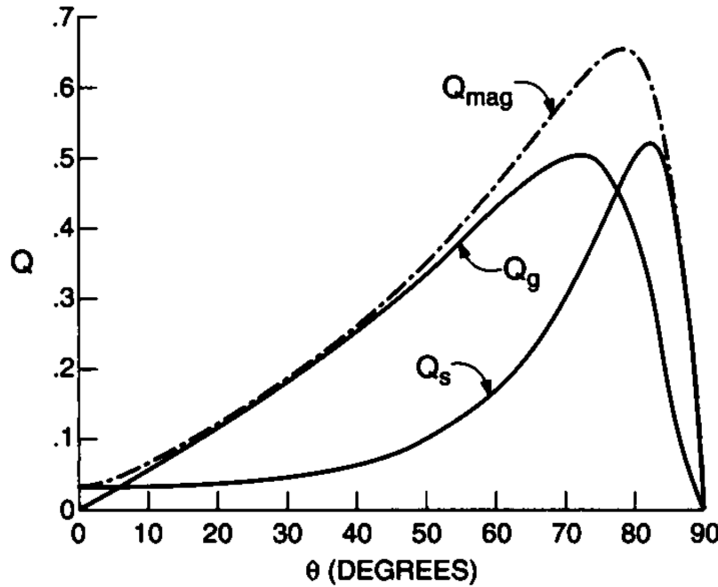


Figure 10: Scattering Q_s , gradient Q_g , and overall Q_{mag} trapping efficiencies for a single ray incident on a sphere of refractive index 1.2. Vertical axis shows efficiency value. Figure reproduced from Ashkin [13].

To determine the extent to which to increase the beam waist (and hence overfill the aperture), the ray optics simulation was modified to output 2D plots of trapping efficiency using Equation 5. Among the numerous values of beam waist that were tested, two cases (beam waist set to $w_0 = L$ and $w_0 = 0.3L$, where $L = 2.099$ mm is the Nikon MRL07920 objective aperture radius) are shown in Figure 11. In the transversal plane, both simulations show a circular (yellow) ring of relatively high trapping efficiencies. At their maxima, the smaller beam waist simulation gave trapping efficiencies around 0.51, which were marginally higher than the efficiencies of 0.42 from the larger beam waist simulation. The larger beam waist simulation also showed a more gradual drop off of trapping efficiency moving outwards from the ring of maximum efficiency. In both cases, the tweezed particle was in a stable transversal trap.

However, for $w_0 = 0.3L$, in the longitudinal plane, the trapping efficiency never rose beyond 0.02 on the z

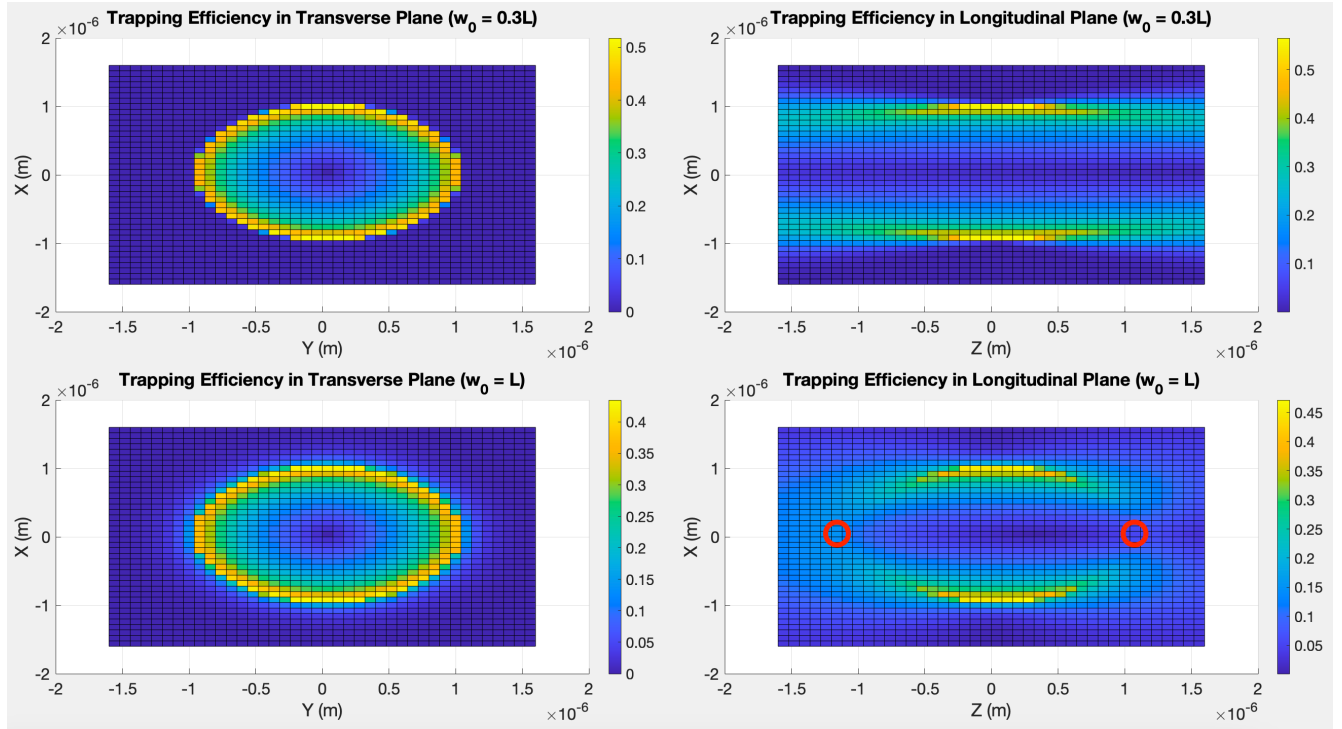


Figure 11: MATLAB simulation of gradient and scattering trapping efficiencies in transverse and longitudinal planes, respectively. Comparing trapping efficiencies when beam waist is large at $w_0 = L$ and small at $w_0 = 0.3L$, where L is the objective aperture radius.

axis (as indicated by the end-to-end horizontal dark blue region). On the other hand, for $w_0 = L$, trapping efficiencies reached 0.15 and 0.096 on the red circled regions of the z axis. The model demonstrates that a sufficiently large beam waist, such as $w_0 = L$, is essential to obtain z axis trapping efficiencies large enough for stable trapping. When $w_0 = L$, the $\frac{1}{e^2}$ intensity points are aligned on the edge of the aperture, meaning that approximately 87% of the incident power is transmitted [5]. Therefore, to prevent further power loss, the beam waist w_0 was not increased further. It is shown that the combination of $w_0 = L$ and the chosen NA of 1.1 is sufficient to create stable trapping dynamics in Section 2.2.

Lastly, we have thus far discussed overfilling the aperture of the objective; however, our setup is a holographic optical tweezer which contains a SLM (see Section 2.3). So in reality, we will be overfilling the SLM (in the same manner described above), which results in the overfilling of the aperture [15].

2.1.5 Beam mode and trapping efficiency

So far, we have assumed that the designed optical tweezer uses a Gaussian beam due to its simplicity and because the trapping laser produces a Gaussian beam as mentioned in Section 2.1.6. However, it may be beneficial to produce beams that exploit the fact that rays originating from the aperture edge disproportionately contribute to increased trapping efficiencies. For instance, as shown in Figure 12,

we may generate higher-order beam modes (which have more complex intensity distributions), such as Laguerre-Gaussian beams with radial index $p = 0$ and azimuthal index $l = 3$ or Hermite-Gaussian beams with the mode $n = 0$ and $m = 1$. Laguerre-Gaussian beams with azimuthal index $l = 3$ have been shown to improve axial trapping efficiency, and allow optical tweezer systems to obtain equivalent trapping forces with half the laser power [16]. This may potentially be important for our single cell surgery platform, if the user is handling cells that are particularly prone to photodamage. As the tweezer system employs a SLM to multiplex the beams, the SLM can also easily be used to generate higher-order beam modes (instead of standard Gaussian beams). This section highlights that possibility of using more complex beams if needed, but for the design process and analysis moving forward, we consider Gaussian traps as they are simpler and sufficient for our use case.

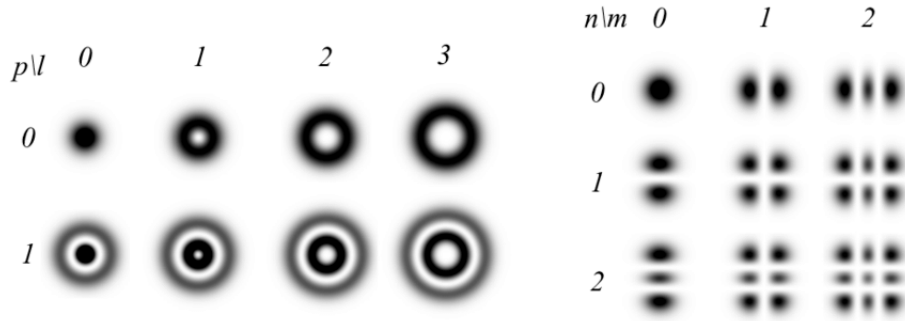


Figure 12: Laguerre-Gaussian and Hermite-Gaussian beams. Reproduced from Walbron *et. al* [17].

2.1.6 Laser design: wavelength and power

The laser selection is a crucial aspect of the optical tweezer design. Our system will be using the Hubner Photonics Cobolt 06-01 continuous wave 975 nm laser. The near-infrared wavelength of 975 nm was chosen to fulfill Design Criteria 2 in Section 2.1, regarding minimisation of photodamage to the cell near the tweezed microparticles. Numerous studies have previously shown that particular wavelengths reduce optical damage, laser absorption and thermal effects on cells [5, 9]. For instance, Liang *et. al* measured cloning efficiency of Chinese hamster ovary (CHO) cells as a function of trapping laser wavelength [18]. As shown by the dashed line in Figure 13, cloning efficiency is greatest (and thus there is least photodamage) around 980 nm, followed by the peak at 830 nm. Our system's tweezing operation lasts for 124 ms on average per particle (justified in Section 3.5.4), and transmits around 5 mW of power per cell (because each cell has one optical trap in its vicinity). Since the dashed plot in Figure 13 is based on 5 minutes of trapping at 88 mW, assuming CHO cells are approximately representative of general cell photo-sensitivity, our system will achieve nearly 100% cloning efficiency and satisfy Design Criteria 2. Moreover, Neuman

et. al also conducted studies on the effect of optical trapping on *Escherichia coli* bacteria. The group tethered bacteria to a surface with a single flagella, which caused them to swim around in a rotational motion, where the rotational rate was linked to bacterial health and metabolic rates [19, 20]. The solid line in Figure 13 represents the lethal dose time, i.e. the time taken for the rotational rate to reduce to 50% of its initial value, as a function of trapping laser wavelength. Although *Neuman et. al*'s study was independently completed, it confirms that 980 nm and 830 nm were the least photodamaging wavelengths. Based on evidence presented in these studies, the more commonly used 1064 nm trapping lasers were ruled out, and 975 nm was chosen for our single cell surgery application.

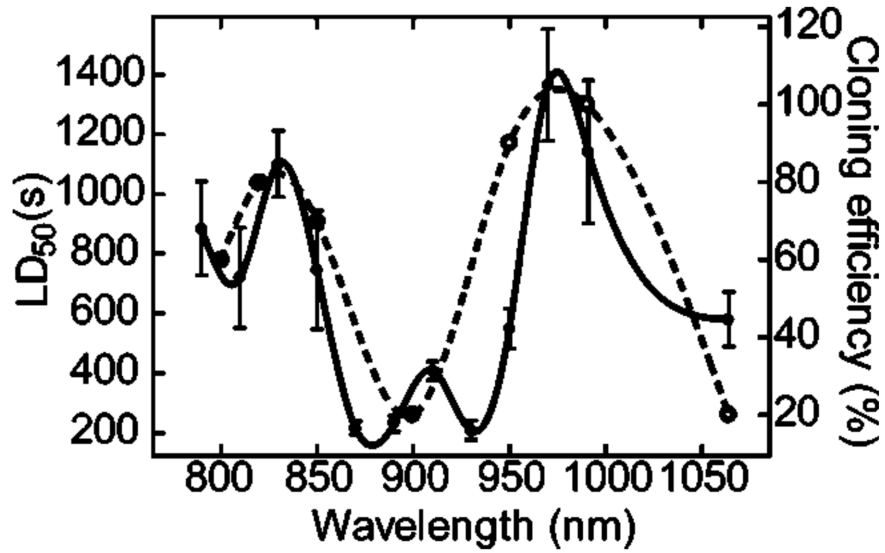


Figure 13: Plots showing the effect of laser wavelength on photodamage to cells. The closed circles and solid line (with the left axis) indicate half lethal dose time for *Escherichia coli* bacteria. The open circles and dashed line (with the right axis) represent the cloning efficiency of CHO cells after 5 minutes of trapping at 88 mW. Reproduced from Neuman *et. al* [19]

The Cobolt 06-01 975 nm laser produces a high-quality linearly polarised TEM₀₀ beam, a beam whose intensity profile closely matches a Gaussian and does not vary throughout propagation. The beam diameter at the laser aperture is $2 \times w_{laser} = 700\mu\text{m}$. In addition, the laser power is 250 mW. With this initial laser power P_{laser} , the power allocated to each particle in an optical trap P is given by:

$$N \times P = P_{laser} \times \eta_{hwp,pbs} \times \eta_{be} \times \eta_{of} \times \eta_{1,diff} \times \eta_{gs} \times \eta_{dm} \times T_{obj} \quad (11)$$

where N is the number of particles to simultaneously tweeze, $\eta_{hwp,pbs}$ is the fraction of power transmitted through the half wave plate and polarising beam splitter, $\eta_{be} \approx 0.95$ is an estimate of the beam expander transmission efficiency, $\eta_{of} = 0.87$ is the fraction of power after beam overfilling, $\eta_{1,diff} = 0.99$ is the SLM

1st order diffraction efficiency (discussed in Section 2.3.2), $\eta_{gs} = 0.93$ is the efficiency of the Gerchberg-Saxton phase retrieval algorithm (introduced later in Section 2.3.3 and 2.3.4), $\eta_{dm} = 0.9$ is the dichroic mirror transmission efficiency (justified in Section 6.5.2), and $T_{obj} = 0.68$ is the objective lens transmission efficiency. Setting the number of particles N to its maximum of 9, and $\eta_{hwp,pbs} = 1$ (no intensity attenuation), the maximum trapping power available for each particle is 12.9 mW. This is comfortably greater than 5 mW, the power that was used in simulations in Section 2.1.2 and will be used in Section 2.2 to demonstrate stable trapping dynamics. To generate 5 mW optical traps for each microparticle, the user can configure the half wave plate and polarising beam splitter as detailed in Section 2.1.7; however, should the user require stronger traps (e.g. if they are using larger microparticles), they have the option to significantly increase the power per optical trap.

2.1.7 Half wave plate and polarising beam splitter

If the user desires to produce optical traps with 5 mW of power (which is less than the maximum available power per trap of 12.9 mW), they must control the intensity of the incoming laser beam using the half wave plate (HWP) and polarising beam splitter (PBS) setup. More details on the HWP and PBS theory can be found in Section 4.3.2 (as the laser ablation system has this identical component). The key operating principle is that the HWP can be rotated to control the intensity of the output laser beam I according to:

$$I = I_0 \cos^2(2\phi) \quad (12)$$

where I_0 is the input beam intensity and ϕ is the HWP azimuthal angle. For instance, to obtain 5 mW of power per trap, the ratio for attenuation is $\frac{I}{I_0} = \frac{5}{13.3}$, and thus the HWP must be rotated by $\phi = 34^\circ$.

2.1.8 Beam expander

As shown in the designed optical layout in Figure 3, after the laser beam has passed through the HWP and PBS setup, it will be expanded, from its initial diameter of $0.7 \mu\text{m}$ to fill the active space of the HSP1K-850-1650-PC8 SLM, which is $17.40 \text{ mm} \times 17.4 \text{ mm}$. This means that the magnification M and the ratio of focal lengths f_1 and f_2 (from Figure 3) must be $M = \frac{f_2}{f_1} = \frac{17.40}{0.7} \approx 25$. Thus, the Comar Optics 13 TE 25 beam expander, which has a magnification of 25X, will be used in our optical tweezer design.

2.2 Optical trapping with Brownian motion

In Section 2.1, optical traps were modelled using ray optics simulations and the results were subsequently used to inform design parameters of the optical tweezers. These simulations, however, did not account for Brownian motion, i.e. the random motion of particles suspended in a medium. Since our polystyrene

microparticles exist in a cell culture (primarily water-like) medium, the microparticle will perpetually exhibit random movements caused by collisions with numerous molecules from the surrounding medium. Thus, the behaviour and motion of the optically trapped particle is governed by the combined effect of the deterministic optical forces and random Brownian motion. In this section, we will explore whether the designed optical trap performs as intended in the presence of Brownian motion, and hence check whether Design Criteria 3 is satisfied.

2.2.1 Model and simulation of Brownian microparticle in optical trap

The position x of a Brownian particle in an optical trap in single dimension can be modelled by the Langevin equation [21]:

$$m\ddot{x}(t) = -\gamma\dot{x}(t) + \kappa x(t) + \sqrt{2k_B T \gamma} W(t) \quad (13)$$

where the $m\ddot{x}(t)$ term represents inertia, $-\gamma\dot{x}(t)$ represents friction, $\kappa x(t)$ represents the optical restoring force, and $\sqrt{2k_B T \gamma} W(t)$ represents the random forces due to collisions with neighbouring molecules. Here, γ is the particle friction coefficient, which is given by $\gamma = 6\pi\eta a$, where η is the surrounding medium's viscosity and a is the particle radius. k_B is the Boltzmann constant, and $W(t)$ represents white noise. In this model, we ignore gravitational and buoyant forces since they are negligible as proven in Section 3.2.

In fluids with a low Reynolds number (ratio of inertial to viscous forces), it is possible to ignore the inertial term to give the overdamped Langevin equation (this is justified in more detail in Section 3.2):

$$0 = -\gamma\dot{x}(t) + \kappa x(t) + \sqrt{2k_B T \gamma} W(t) \quad (14)$$

To obtain a numerical solution to the above stochastic differential equation, we apply the finite difference method. This can be done by substituting the continuous-time functions with discrete-time sequences, i.e. $x(t)$ with x_n , $\dot{x}(t)$ with $\frac{x_n - x_{n-1}}{\Delta t}$, and $\ddot{x}(t)$ with:

$$\frac{\frac{x_n - x_{n-1}}{\Delta t} - \frac{x_{n-1} - x_{n-2}}{\Delta t}}{\Delta t} = \frac{x_n - 2x_{n-1} + x_{n-2}}{\Delta t^2} \quad (15)$$

where Δt is the time step. We can then solve for x_n to obtain an approximate solution to Equation 13.

Before evaluating the solution, we must modify the white noise term $W(t)$. White noise obeys the following three properties. The ensemble average of white noise $\langle W(t) \rangle = 0$ for all t . White noise has unitary power: $\langle W(t)^2 \rangle = 1$. And lastly, given $t_1 \neq t_2$, $W(t_1)$ and $W(t_2)$ are independent of one another. Due

to these properties and the fact that white noise has infinite variance and discontinuities, it cannot be treated as a standard function when using the finite difference method [10]. In our analysis, we will follow Volpe's approach [21] of treating white noise as a discrete sequence of random numbers W_n . Consider the random trajectory of a Brownian particle described by the following equation:

$$\dot{x}(t) = W(t) \quad (16)$$

To obtain a discrete sequence W_n that emulates white noise properties, we take W_n as random numbers with zero mean. Similar to the unitary power property, we also require that $\frac{\langle W_n \Delta t^2 \rangle}{\Delta t} = 1$ [21]. Lastly, given $n \neq k$, we assume W_n and W_k are independent. With this in mind, in order to generate W_n in MATLAB, a sequence of Gaussian random numbers w_n with mean $\mu = 0$ and variance $\sigma = 1$ was first produced. Then, the sequence was scaled according to $W_n = \frac{w_n}{\sqrt{\Delta t}}$ to match the variance of the distribution to $\frac{1}{\Delta t}$.

Substituting $\dot{x}(t)$ in Equation 16 with $\frac{x_n - x_{n-1}}{\Delta t}$, and rearranging gives:

$$x_n = x_{n-1} + \sqrt{\Delta t} w_i \quad (17)$$

Using Equation 17, Brownian particle trajectories can be simulated in all 3 spatial dimensions. Example trajectories in $[x, y, z]$ directions are shown in Figure 14.

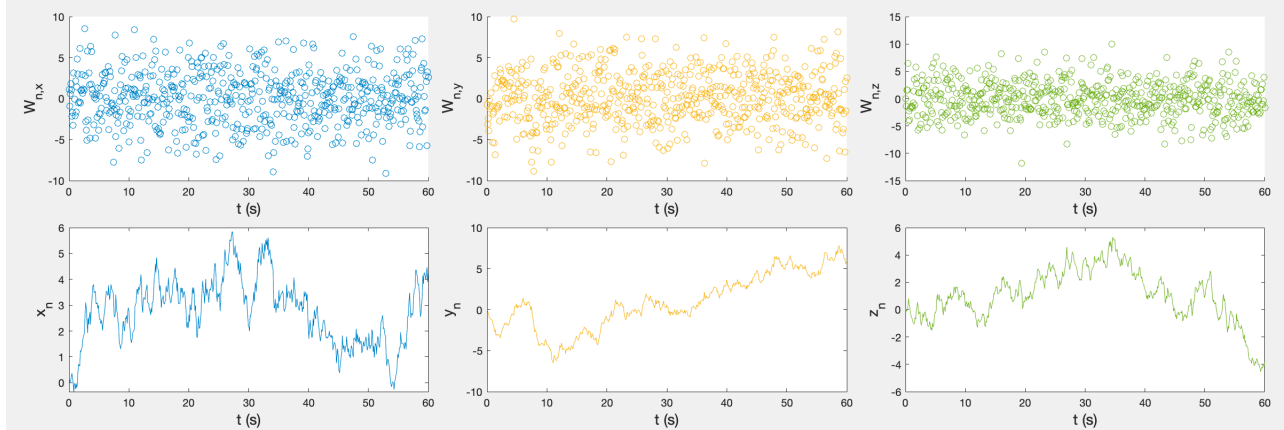


Figure 14: MATLAB simulation of discrete white noise sequence W_n (first row) and position trajectory $[x_n, y_n, z_n]$ in $[x, y, z]$ directions (second row). $\Delta t = 0.1\text{s}$

By modelling white noise as a discrete sequence, we can now solve the overdamped Langevin Equation 14 with the finite difference method. In 3D, this evaluates to [21]:

$$\mathbf{r}_n = \mathbf{r}_{n-1} - \frac{\kappa}{\gamma} \Delta t \mathbf{r}_{n-1} + \sqrt{2D\Delta t} \mathbf{w}_i \quad (18)$$

where $\mathbf{r}_n = [x_n, y_n, z_n]$ is the vector containing $[x, y, z]$ positions at time t_n , $\kappa = [\kappa_x, \kappa_y, \kappa_z]$ contains the trapping stiffnesses in $[x, y, z]$ directions, $\mathbf{w}_i = [w_{x,i}, w_{y,i}, w_{z,i}]$ contains the random number sequence associated with each direction, and $D = \frac{k_B T}{\gamma}$.

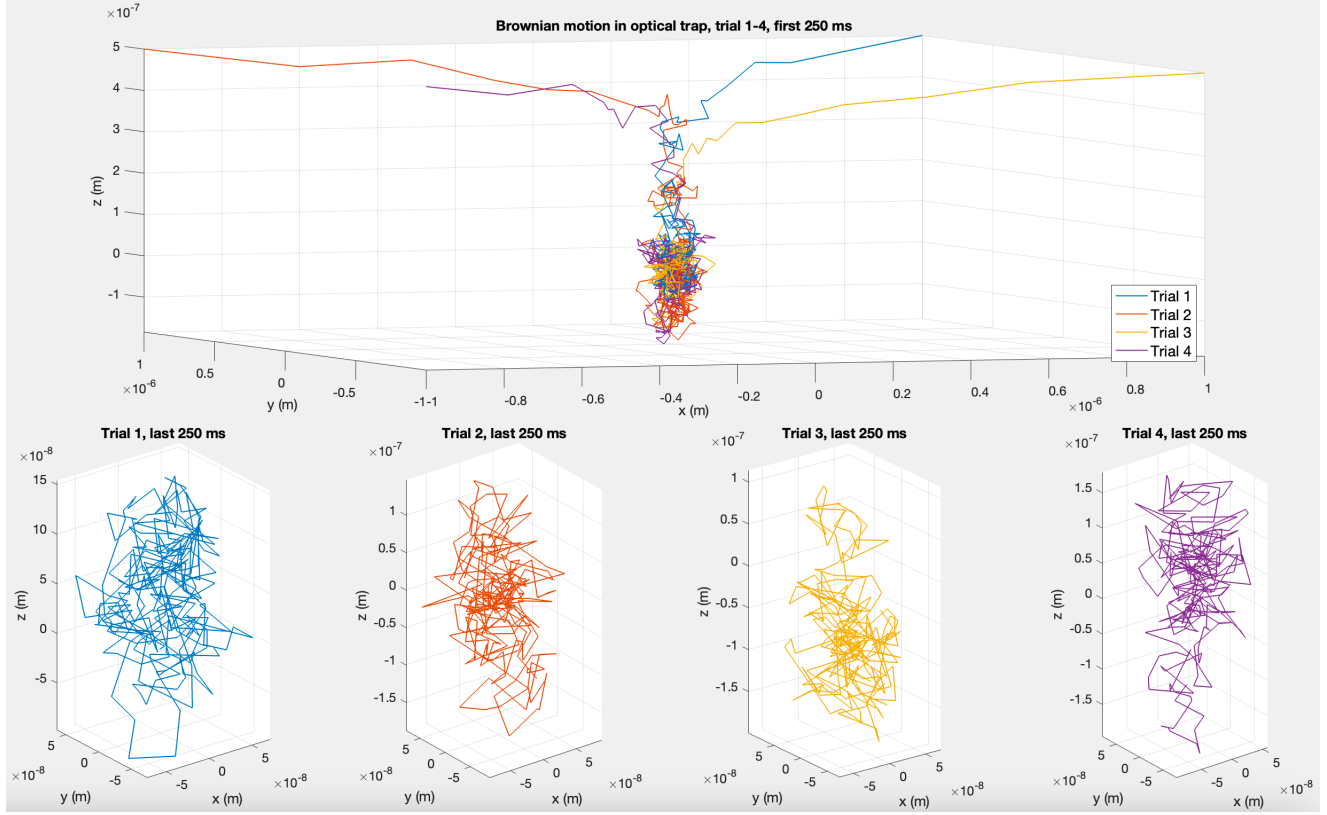


Figure 15: MATLAB optical trap and Brownian motion simulation. Top plot shows four distinct particle at initial positions $[\pm R, \pm R, 0.5R]$ falling into the optical trap in the first 250 ms of simulation. Bottom plots show the final 250 ms, where the particles are optically trapped but fluctuate within an ellipsoidal volume. All plots show particle centre positions. All bottom plots satisfy Design Criteria 3.

Using Equation 18, the optical trap simulation in Section 2.1.2 was augmented. The simulation begins by placing the trapped particle at a specified initial position. Using ray optics as previously discussed, the simulation computes the optical force at the current position based on trap stiffness values. Minimum trap stiffness values obtained in Section 2.1.3 of $\kappa_x = 0.83 \text{ pN}/\mu\text{m}$ and $\kappa_z = 5.83 \text{ pN}/\mu\text{m}$ were used to simulate the worst-case performance of the optical trap. Subsequently, the position is updated using Equation 18, hence taking into account the effect of friction, optical trapping, and Brownian forces. This process repeats and the trajectory of the centre of the particle is plotted. The time step Δt was set to 1 ms, and 500 iterations were executed. To ensure that the simulation results were not divergent, Δt was chosen to be lower than $\tau_{ot} = \frac{\gamma}{\kappa} = 3.23 \text{ ms}$, the timescale at which the optical tweezing forces acts [10].

The results are shown in Figure 15. The particle was initially placed away from the trap centre at 4

arbitrary locations $[x, y, z] = [\pm R, \pm R, 0.5R]$. In the first 250 ms seconds (top plot), the particles at all four positions immediately head towards the trap centre and remain within a localised volume. During the last 250 ms (bottom plots), all particles occupied an ellipsoidal volume, where the major axis is in the z direction. Such ellipsoidal geometry is caused by stronger transversal confinement due to gradient forces being greater than scattering forces (shown in Section 2.1.3). In the transversal plane, the x and y positions ranged from -0.05 to 0.05 μm . z positions, at most, varied from around -0.2 μm to 0.2 μm . Based on these simulations, Design Criteria 3, i.e. containing the trapped particle within a 1 μm -diameter sphere, has been satisfied. The results show that with our design (NA of 1.1, beam waist $w_0 = L$, $P = 5$ mW) and chosen optical components, the system generates sufficient trapping for particle insertion into the ablated hole, even in the presence of Brownian forces.

2.2.2 Analysing the performance of the optical trap under Brownian motion

Brownian motion in an optical trap is a stochastic process. Although it is important to simulate specific particle trajectories as done in the previous section, we must characterise the *average* behaviour of particles. Mean square displacement (MSD) is commonly used to quantify the amount of space explored by a Brownian particle in a particular direction, and is defined using an ensemble average:

$$MSD_x(\tau) = \langle (x(t + \tau) - x(t))^2 \rangle \quad (19)$$

The MSD of a Brownian particle in an optical trap is given by the MSD of a Brownian particle in a harmonic oscillator, which can be shown to be [22]:

$$MSD_x(\tau) = \frac{2k_B T}{\kappa_x} \left[1 - e^{-\frac{\tau}{\tau_{ot}}} \right] \quad (20)$$

Figure 16 shows plots of MSD for various trap stiffnesses. All plots exhibit plateauing behaviour, indicating that beyond a particular time lag τ , the distance the particle explores does not increase further. This limiting τ value increases, as the trap stiffness decreases (i.e. as the trap becomes weaker). For the longitudinal trap stiffness of 0.83 pN/ μm (lower than the transversal stiffness of 5.83 pN/ μm), the MSD plateaus at approximately 0.01 μm^2 , meaning that on average, the particle does not explore a distance larger than 0.1 μm in a particular direction. We thus confirm that, on average, our particle can be successfully inserted into the ablated hole as it stays well within the 0.5 μm radius (1 μm diameter) sphere defined by Design Criteria 3.

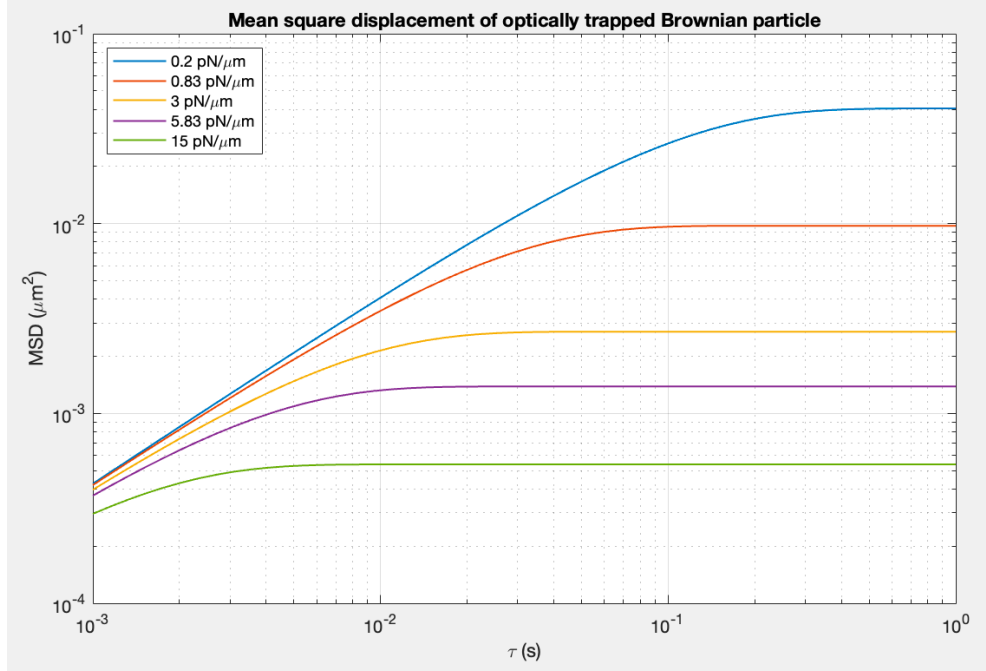


Figure 16: Plots of MSD for various κ values. Recall that $0.83 \text{ pN}/\mu\text{m}$ and $5.83 \text{ pN}/\mu\text{m}$ are the worst-case longitudinal and transversal trap stiffnesses for our designed optical trap, as calculated in Section 2.1.3.

2.3 Holographic optical tweezing

Up to this point, the design, analysis, and simulations considered the generation of a single 5 mW optical trap. However, Design Criteria 4 requires us to simultaneously and dynamically tweeze up to 9 microparticles. While it is possible to move traps through mechanical components, the optical setups involved tend to be complex. Additionally, as mentioned in Section 2.1.5, it would be beneficial to design a versatile optical tweezer which can produce higher order beams or more beams if needed. Therefore, our design will be a holographic optical tweezer (HOT) which uses a diffractive optical element (DOE) to modify and multiplex the single incoming 250 mW laser beam into multiple 5 mW beams as desired. As the DOE is computer controlled, a sequence of holograms can be generated to achieve dynamic tweezing.

2.3.1 Working principle of HOTs

In order to effectively design our HOT, we must first understand the theory underlying HOTs. Figure 17 demonstrates the operating principle of HOTs. Suppose we have the transverse profile of an incoming laser beam $E_{beam}(x, y)$, where z is the propagation direction. In our optical tweezer, $E_{beam}(x, y)$ would be the profile of a single Gaussian beam after the initial laser beam has passed through the HWP, PBS, and beam expander. The core objective is to configure a DOE and Fourier lens setup and determine the required mask of the DOE that allows us to modify the incoming beam in such a way that the beam profile at the front focal plane $E_{focus}(x, y)$ shows multiple Gaussian traps.

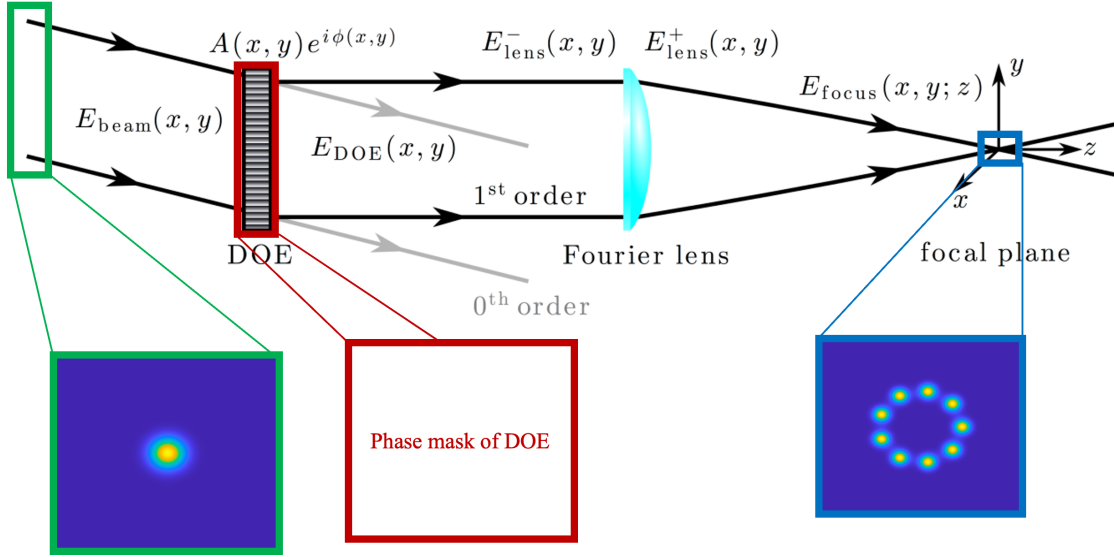


Figure 17: Diagram of HOT working principle. Reproduced and modified from Jones et. al [10].

To achieve this, we place the DOE at the back focal plane of the Fourier lens, called the DOE plane. Then we can model the propagation of the beam as follows [10]. As the incoming beam $E_{beam}(x, y)$ in Figure 17 passes through the DOE, we consider the first order diffraction beam E_{DOE} , which modifies the amplitude and phase of the incoming beam according to $A(x, y)e^{i\phi(x,y)}$ where $A(x, y)$ and $\phi(x, y)$ express the amplitude and phase modulation profiles of the DOE:

$$E_{DOE} = A(x, y)e^{i\phi(x,y)}E_{beam}(x, y) \quad (21)$$

We then model the profile as the beam propagates to the plane immediately before the Fourier lens $E_{lens}^-(x, y)$. To that end, we use the Fresnel diffraction integral which allows us to evaluate the beam profile at position z , i.e. $E(x, y, z)$, given the electromagnetic field profile at $z = 0$, i.e. $E(x', y', 0)$ [23]:

$$E(x, y, z) = \frac{e^{ik_0 z}}{i\lambda_0 z} \int_{-\infty}^{+\infty} \int_{-\infty}^{+\infty} E(x', y', 0) e^{-\frac{ik_0 z}{2z}((x-x')^2 + (y-y')^2)} dx' dy' \quad (22)$$

where k_0 and λ_0 are vacuum wavenumber and wavelength. Applying Fresnel diffraction to E_{DOE} gives us the following expression for $E_{lens}^-(x, y)$:

$$E_{lens}^-(x, y) = \frac{e^{ik_0 f}}{i\lambda_0 f} e^{i\frac{k_0}{2f}(x^2+y^2)} \int_{-\infty}^{+\infty} \int_{-\infty}^{+\infty} E_{DOE}(x', y') e^{i\frac{k_0}{2f}(x'^2+y'^2)} e^{i\frac{k_0}{2f}(xx'+yy')} dx' dy' \quad (23)$$

where f is the focal length of the Fourier lens. To model the effect of the Fourier lens from $E_{lens}^-(x, y)$ to

$E_{lens}^+(x, y)$, we use the approximation that a Fourier lens transforms the lens incident plane to the lens exit plane by multiplying a quadratic phase factor $e^{-i\frac{k_0}{2f}(x^2+y^2)}$ [24]. Thus $E_{lens}^+(x, y)$ is simply given by:

$$E_{lens}^+(x, y) = E_{lens}^-(x, y)e^{-i\frac{k_0}{2f}(x^2+y^2)} \quad (24)$$

The quadratic phase factor in Equation 24 cancels with the $e^{i\frac{k_0}{2f}(x^2+y^2)}$ term in Equation 23. So $E_{lens}^+(x, y)$ becomes:

$$E_{lens}^+(x, y) = \frac{e^{ik_0 f}}{i\lambda_0 f} \int_{-\infty}^{+\infty} \int_{-\infty}^{+\infty} E_{lens}^+(x', y') e^{i\frac{k_0}{2f}(x'^2+y'^2)} e^{i\frac{k_0}{2f}(xx'+yy')} dx' dy' \quad (25)$$

Once again, to propagate the beam profile from $E_{lens}^+(x, y)$ to the front focal plane profile $E_{focus}(x, y)$, we use Fresnel diffraction, which gives us:

$$E_{focus}(x, y) = \frac{e^{ik_0 f}}{i\lambda_0 f} e^{i\frac{k_0}{2f}(x^2+y^2)} \int_{-\infty}^{+\infty} \int_{-\infty}^{+\infty} E_{lens}^+(x', y') e^{i\frac{k_0}{2f}(x'^2+y'^2)} e^{i\frac{k_0}{2f}(xx'+yy')} dx' dy' \quad (26)$$

We now substitute Equation 25 into the expression for $E_{focus}(x, y)$, and find that, after much simplifying, $E_{focus}(x, y)$ can be expressed in terms of a 2D Fourier Transform [10]:

$$E_{focus}(x, y) = \frac{e^{ik_0 f}}{i\lambda_0 f} 4\pi^2 \text{2DFT}[E_{DOE}] \quad (27)$$

where $\text{2DFT}[E_{DOE}]$ is given by the standard definition of a 2D Fourier Transform:

$$\text{2DFT}[E_{DOE}] = \frac{1}{(2\pi)^2} \int_{-\infty}^{+\infty} \int_{-\infty}^{+\infty} E_{DOE} e^{-i2\pi(ux+vy)} dx dy \quad (28)$$

Here, u and v are spatial frequencies in x and y directions, and are calculated as $u = \frac{x}{f\lambda_0}$ and $v = \frac{y}{f\lambda_0}$.

Equation 27 is an important and foundational result to the operation and design of our HOT. It states that the Fourier transform of the profile at the DOE plane is proportional to the profile at the focal plane. This result is powerful as it means that by controlling the magnitude of spatial frequencies u and v of the DOE mask, we can control the magnitude of the beam intensity at certain spatial positions x and y at the focal plane. To determine the appropriate DOE mask that will generate our desired target beam distribution (multiple optical traps) at the focal plane, we will exploit this property.

2.3.2 Spatial light modulator

Before discussing how the DOE mask will be computed, it is important to discuss the device in our tweezers design that will act as the DOE. In our system, a spatial light modulator (SLM) will function as the DOE.

A SLM is a programmable device that can modulate the amplitude, phase, or polarisation of incoming light. The goal of the SLM is to take the incoming beam and create an appropriate computer-generated hologram (CGH). A hologram is simply a recording of the light field (containing amplitude and phase information). The output beam from the SLM, then contains the phase or amplitude information from the CGH, and when this output beam is converged (using a Fourier lens), and thus a Fourier transform is applied, the desired light field is reconstructed. The use of a CGH is why our setup is called a HOT.

To choose an appropriate SLM for our optical tweezing application, a multi-criterion analysis, shown in Table 1, was completed.

Table 1: Multi-criterion analysis of SLMs. Each SLM and category pair was given a score ranging from 1 to 10. Weightings of each category are shown in the column headers. Total scores shown in red.

SLM	Modulation type (20%)	Resolution (15%)	Switching rate (20%)	Phase levels (20%)	1st order diff. efficiency (20%)	Cost (5%)	Total
DMD	3	8	9	0	8	4	5.4
Transmissive SLM	5	8	7	7	8	5	6.85
Nematic LCoS	10	8	7	9	8	5	8.25
Ferroelectric LCoS	10	8	9	3	8	4	7.4

A summary of the justifications for the scores are below:

1. **Modulation type:** Digital micromirror devices (DMDs) are amplitude modulation SLMs that operate by tilting an array of micromirrors to control light intensity. Since a large fraction of the incoming beam is directed away, the intensity is significantly reduced. Transmissive SLMs are often pixelated liquid crystal displays that can provide amplitude and phase modulation. For our HOT application, we will be using phase-only masks to minimise intensity loss, and thus, DMDs and transmissive SLMs received a low score of 3 and 5. On the other hand, a reflective liquid crystal on silicon (LCoS) SLM consists of a birefringent (i.e. refractive index depends on polarisation and direction of light) liquid crystal layer which is placed between a silicon backplane and cover glass. The pixels on the silicon backplane consist of capacitors, whose voltages can be controlled to rotate the liquid crystals, and hence vary the phase of incoming light. Reflective SLMs are further categorised into nematic and ferroelectric, according to the liquid crystal type. Both nematic and ferroelectric LCoS are phase-only modulators, and thus are most suitable for our HOT application with a score of 10.

2. **Resolution:** A high spatial resolution allows us to generate more accurate reconstructed beams that are less discretised. Modern DMDs, transmissive SLMs, and LCoS SLMs, all typically have sufficient resolutions on the order of 1000×1000 pixels, and thus all SLMs received a score of 8.
3. **Switching rate:** Switching rate influences the rate at which we can produce different light fields, and thus the rate at which we can move the optical traps to achieve dynamic tweezing. DMDs and ferroelectric LCoS SLMs have the highest switching frequencies, up to 5 to 10 kHz. Nematic LCoS and transmissive SLMs have switching rates up to approximately 1.5 kHz, which is also sufficient for our application (see Section 3.5.3). Thus the scores, for the latter two were only slightly lower.
4. **Phase levels:** For accurate focal plane reconstruction, we desire many levels of phase retardation for the SLM. DMDs do not modulate phase so this category was not applicable. Nematic LCoS typically offer analogue or up to 8-bit (256 levels of) phase retardation between 0 and 2π , while the ferroelectric counterparts only offer two phase levels at 0 and 2π . Therefore, nematic LCoS has a clear advantage in this category.
5. **1st order diffraction efficiency:** 1st order diffraction efficiency refers to the fraction of incident light that is present in the first order diffraction beam exiting the SLM. Since the 1st order beam is converged and used for reconstruction, we require a high diffraction efficiency to prevent power loss. Most modern SLMs of all kinds have high first order diffraction efficiencies in the range of 80 to 95 % at 16 to 32 levels of phase retardation. Thus, all SLMs received identical scores.
6. **Cost:** Cost varies significantly depending on the specifications, but SLMs tend to be around \$10,000 to \$20,000. High speed DMDs and ferroelectric LCoS SLMs can be slightly more expensive, and thus received a marginally lower score.

In total, nematic LCoS reflective SLMs obtained the highest score of 8.25 and was chosen for the HOT system. The particular nematic LCoS SLM we will utilise in our design is the Meadowlark Optics HSP1K-850-1650-PC8, which provides a resolution of 1024×1024 . The SLM can achieve a switching rate of 1436.1 Hz, and features analogue phase control with high phase stability. The 1st order diffraction efficiency (at 32 levels of phase retardation) is 99%.

2.3.3 Phase retrieval with Gerchberg-Saxton algorithm

In Section 2.3.1, it was established that the field at the focal plane is proportional to a Fourier transform of the field at the SLM. We now use this relationship to determine the phase modulation field the SLM

needs to generate to achieve a target field at the focal plane, i.e. we *retrieve* the required phase mask.

Theoretically, it is possible to simply apply an inverse Fourier transform to a desired focal plane image; however, this results in a field at the SLM which consists of both amplitude and phase modulation. To preserve beam power, we are interested in algorithms that allow us to generate target beam distributions through phase-only modulation. To that end, we use a powerful phase retrieval algorithm called the Gerchberg-Saxton (GS) algorithm.

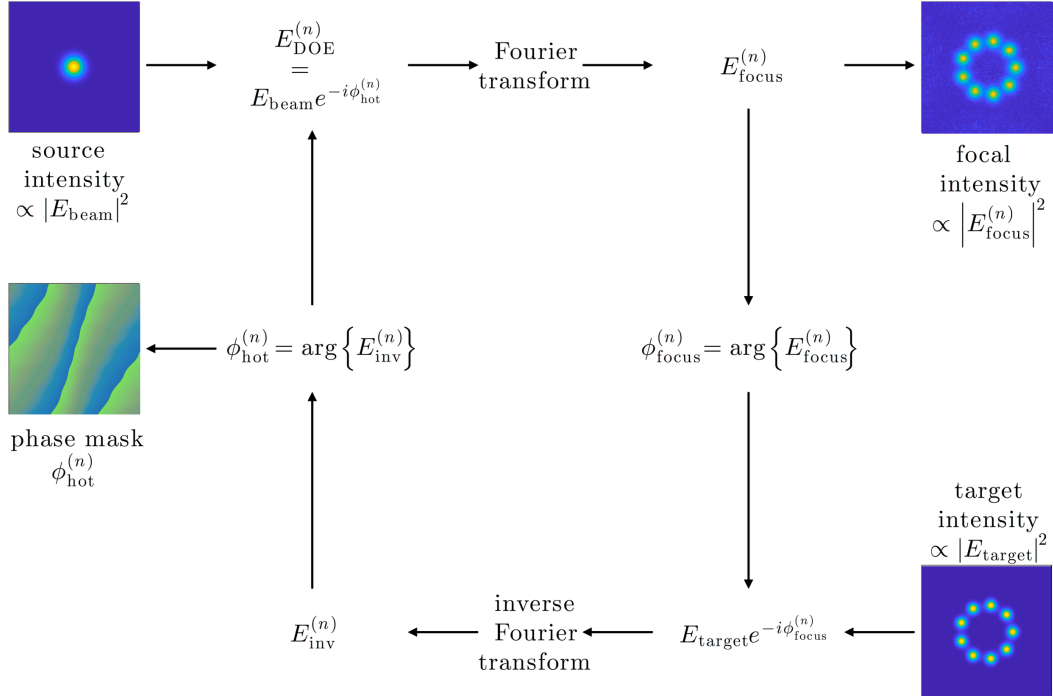


Figure 18: Diagram which shows the iterative computations involved in the Gerchberg-Saxton algorithm. Reproduced and modified from Jones et. al [10].

The GS algorithm is visualised in Figure 18. At the first iteration, the algorithm begins with the DOE (SLM) plane distribution $E_{DOE}^{(1)}$ which is obtained by combining the amplitude distribution of the incoming E_{beam} (a single Gaussian beam) with the phase distribution of the SLM phase mask $\phi_{hot}^{(1)}$. According to Equation 27, given the current phase mask, we compute the reconstructed distribution $E_{focus}^{(1)}$ at the focal plane by applying a Fourier transform. Initially, the reconstructed distribution will not resemble the target distribution. The algorithm however continues and extracts the phase information from $E_{focus}^{(1)}$ and combines this with the amplitude distribution of the target image, giving $E_{target}e^{-i\phi_{focus}^{(1)}}$. An inverse Fourier transform is applied to $E_{target}e^{-i\phi_{focus}^{(1)}}$ to obtain $E_{inv}^{(1)}$. Lastly, the appropriate phase mask for the next iteration $\phi_{hot}^{(2)}$ is obtained by extracting the phase distribution from $E_{inv}^{(1)}$. As many iterations are executed, and as $n \rightarrow \infty$, the reconstructed focal plane closely resembles the target distribution. After

sufficient iterations, the phase mask $\phi_{hot}^{(n)}$ can be extracted and generated at the SLM to produce our desired target image of multiple Gaussian traps.

Herein, we demonstrate how our designed optical tweezer uses the GS algorithm. The incoming beam profile is a 17.40 mm diameter single Gaussian beam as shown in Figure 19. The target distribution is a set of 9 Gaussian optical traps, each placed 30 μm away from each other. The beam radius of the optical traps at the focal plane w_f is 0.37 μm and was calculated in Figure 7. The target beam image in Figure 19 shows a 150 $\mu\text{m} \times 150 \mu\text{m}$ area, which corresponds to a 3 by 3 grid of cells in the sample petri dish.

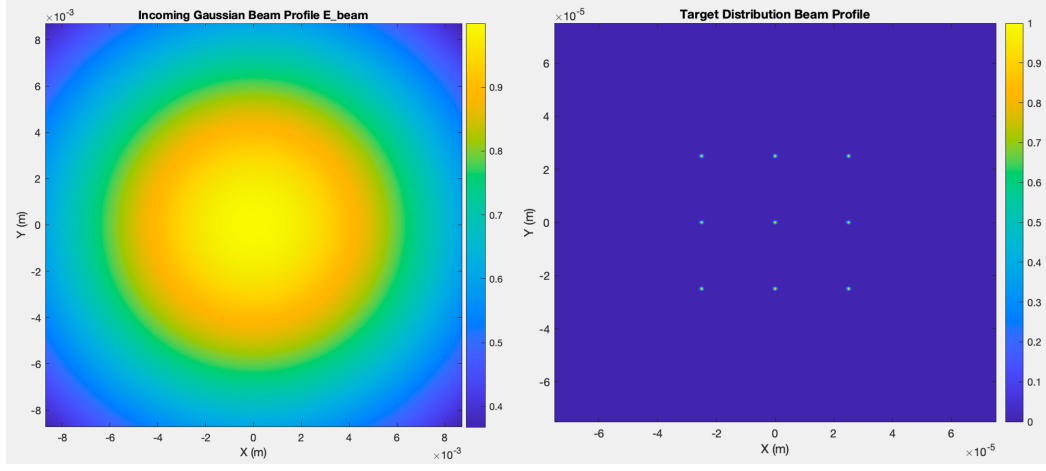


Figure 19: Incoming beam distribution (left) and target beam distribution (right).

2.3.4 Results and evaluation of the phase retrieval

25 iterations of the GS algorithm were executed. The final reconstructed focal plane and extracted SLM phase mask at iteration 25 is shown below in Figure 20. While the reconstructed focal plane seemingly closely resembles the target beam distribution, we must quantify the performance of the phase retrieval. This was done by measuring the phase retrieval efficiency I_{total} , which is given by [10]:

$$I_{total} = \sum_{n=1}^N I_n \quad (29)$$

where I_n represents the intensity of the n th Gaussian optical trap. The extracted phase mask produced a high efficiency of 0.93 (discussion on whether this efficiency is sufficient was in Section 2.1.6).

In addition, over iterations, the percentage standard error σ between the reconstructed focal plane and target beam distribution was tracked:

$$\sigma = \frac{\sqrt{\sum_{n=1}^N (I_n - \langle I_n \rangle)^2}}{N \langle I \rangle} \times 100 \quad (30)$$

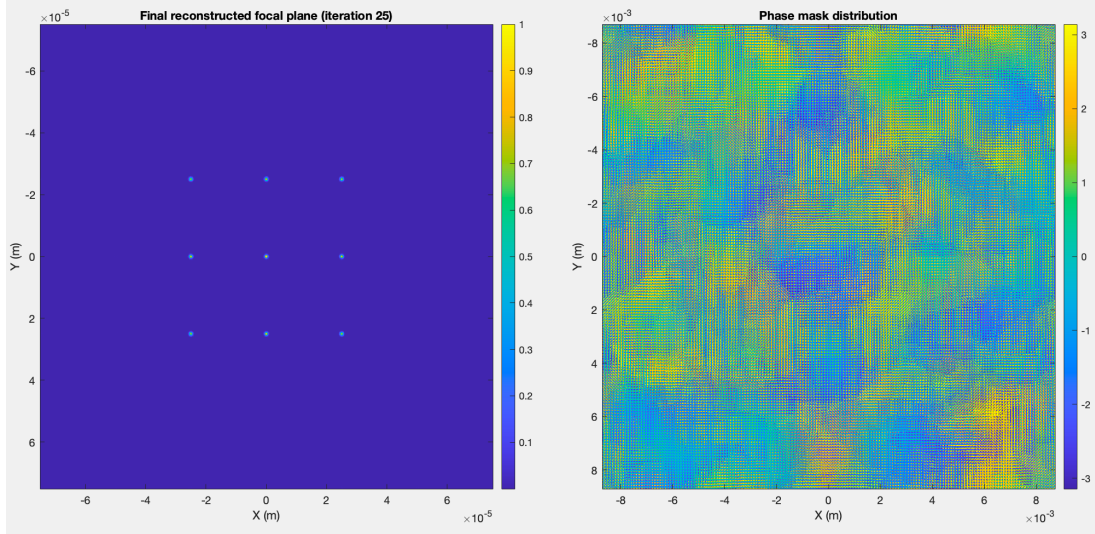


Figure 20: MATLAB simulation of phase retrieval for the SLM using GS algorithm. Reconstructed focal plane (left) and retrieved phase mask for SLM (right).

where $\langle I \rangle = \frac{I_{total}}{N}$. As shown in Figure 21, the standard error decreases significantly as the algorithm progresses. 25 iterations was chosen as the error had plateaued beyond 20 iterations at around 0.6%. In addition, we clearly observe that the individual multiplexed traps gradually resemble the target Gaussian trap with many iterations of the phase retrieval, thus giving qualitative confirmation of success.

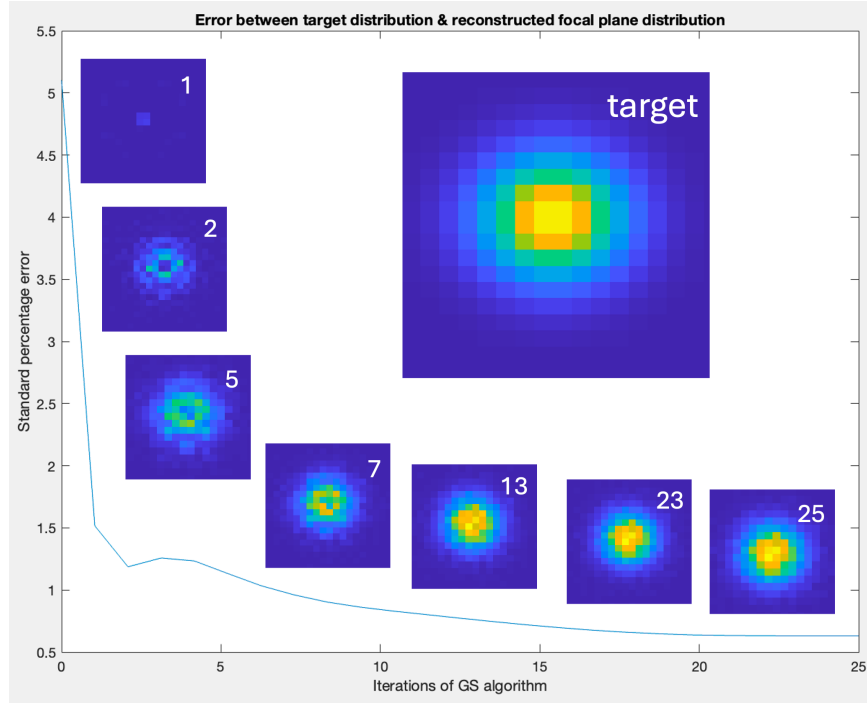


Figure 21: Standard percentage error of the reconstructed focal plane (with respect to the target distribution) σ vs. iterations. The zoomed-in images show the progression of the intensity distribution of the 5th trap (central trap in the grid of 9 traps) over iterations. White number indicates iteration number. The target intensity distribution of the 5th trap is also shown for reference.

2.3.5 Dynamic tweezing procedure

The same process described above can be used to generate up to 9 traps simultaneously in any location within the $180 \mu\text{m} \times 180 \mu\text{m}$ field of view. As required by Design Criteria 4, we will also be able to move each trap in the $[x, y]$ direction by incrementally shifting the trap positions each time the SLM refreshes. As discussed in Section 3.5.3 and 3.5.4, we will operate the SLM at frequency 1436.1 Hz, where in each successive frame each trap can be moved by $0.136 \mu\text{m}$, and thus we will achieve a tweezing speed of $190 \mu\text{m/s}$. With this in mind, the general dynamic tweezing procedure is detailed in Figure 22.

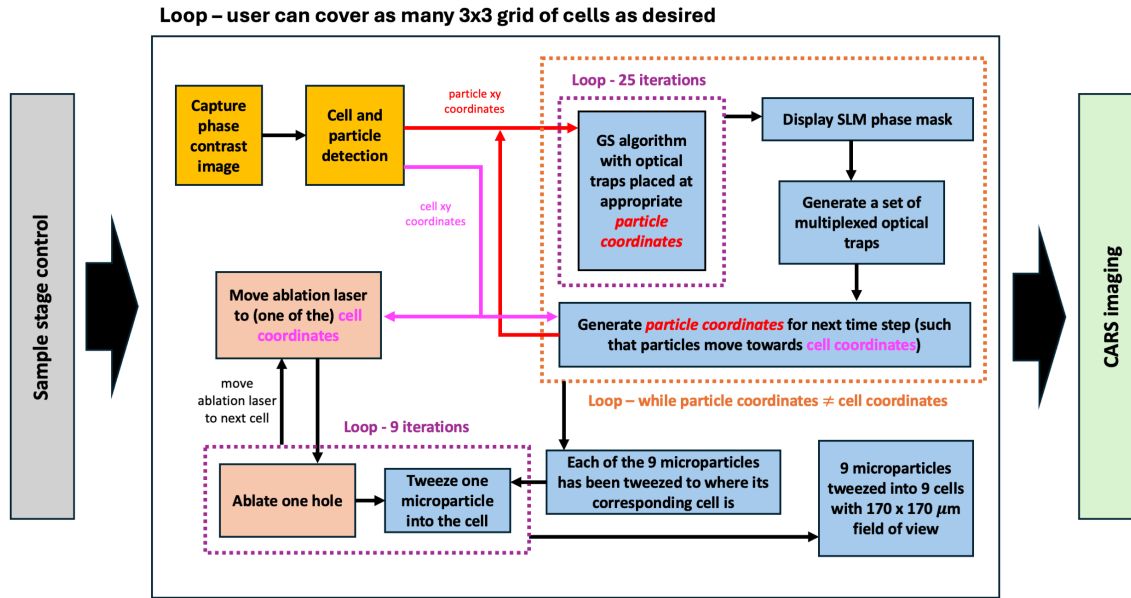


Figure 22: Block diagram demonstrating the dynamic tweezing procedure designed for our system. The diagram also shows how the optical tweezer system receives inputs from other systems within the single cell surgery platform. Blocks are color coded such that blue = optical tweezer system, yellow = phase contrast microscopy system, red = laser ablation system, and green = CARS imaging system.

The optical tweezer system receives $[x, y]$ coordinates of 9 cells and 9 target microparticles (red arrows in Figure 22) from the phase contrast microscope (yellow blocks). By successively updating the position of the optical traps using the GS algorithm and phase mask, the microparticles are moved towards their corresponding cell coordinates (orange dashed-line box). Meanwhile, the ablation laser is moved to one of the cell coordinates. A microparticle is then inserted into the ablated hole via a process detailed further in Section 3.5.4 and 7.7, and this operation repeats 9 times to achieve insertion into all 9 cells.

2.3.6 Holographic optical tweezer setup

The physical setup of the HOT is beyond the scope of this report, but herein, we present a brief overview. The HOT setup will follow the commonly used 4-f configuration. That is, the SLM is placed one focal

length in front of the first Fourier lens and the objective back aperture is placed one focal length behind the second Fourier lens, as shown by f_3 and f_4 in Figure 3. There will be an iris in the intermediate focal plane which blocks any remaining and unnecessary 0th order diffraction beam.

2.4 Cost estimation for the optical tweezer system

The estimated cost of the optical tweezer system is £16,530 (see Table 2). This estimate excludes the objective lens cost as the component belongs to all the systems. The cost is roughly in line with other commercial and cost-effective modular optical tweezers, such as those provided by Thorlabs (£17,821).

Table 2: Estimated cost table for the optical tweezer system.

Component	Quantity	Price per item (£)	Total price (£)
Cobolt 06-01 975 nm laser	1	3,000	3,000
Half wave plate	1	200	200
Polarising beam splitter	1	200	200
Comar Optics 13 TE 25 beam expander	1	700	700
Meadowlark Optics HSP1K-850-1650-PC8 SLM	1	10,000	10,000
Fourier lens	2	100	200
Iris for Fourier lens setup	1	150	150
Position sensitive detector	1	500	500
Dichroic mirror (DM1)	1	1,500	1,500
685 nm calibration laser	1	80	80
Nikon MRL07920 objective	1	28,000	28,000
Optical tweezer system price (excluding objective): £16,530			

2.5 Summary

In Section 2, a powerful holographic optical tweezer appropriate for microparticle insertion into cells was designed. Using ray optics simulations, it was shown that our design and chosen NA value, beam waist, objective lens, beam type, etc. generate optical traps with sufficiently large trapping forces, stiffnesses, and efficiencies to hold the target $2\mu m$ diameter drug-coated microparticles (Section 2.1). Laser wavelength and power were carefully selected and designed to ensure minimum photodamage to cells. Through Brownian motion simulations and MSD analysis, it was demonstrated that the designed optical trap confines the particle into a small enough ellipsoidal volume to guarantee successful insertion into the ablated hole (Section 2.2). Lastly, the holographic optical tweezing and phase retrieval process were analysed, and shown to be able to simultaneously and dynamically manipulate 9 particles into 9 cells within a $180 \mu m \times 180 \mu m$ field of view (Section 2.3). Overall, the designed optical tweezer system plays a crucial role in delivering the drug or plasmid-coated microparticles into the target cell, and performing single cell surgery in a cost-effective manner.

3 Optical Tweezer dynamics and trajectory planning - Sean Mata

3.1 Introduction

This section is concerned with the analysis of the dynamics of a particle in an optical trap and applying this to be able to plan a stable trajectory for the movement of particle(s) in a series of optical traps in the x-y plane. To do this, in Section 3.2 there is a complete overview of the forces on an optically trapped particle and the modelling assumptions that can be made, such as using Stoke's law for the drag force and a low Reynold's number leading to zero inertial force. These assumptions are also referenced above in Section 2 which simulates the movement of a particle in a single optical trap. Furthermore, Section 3.3 specifies how trap stiffness may significantly vary from theoretical calculations, which necessitates the selection of a calibration procedure to be able to implement this system in practice, which is covered in Section 3.4. Finally, in Section 3.5 the modelling assumptions in Section 3.2 are used to model the movement of a particle for the purpose of planning a stable trajectory to be able to move the particle as quickly as possible while remaining robust to Brownian motion and trapping force or drag force variations.

3.2 Dynamics of the optical tweezing

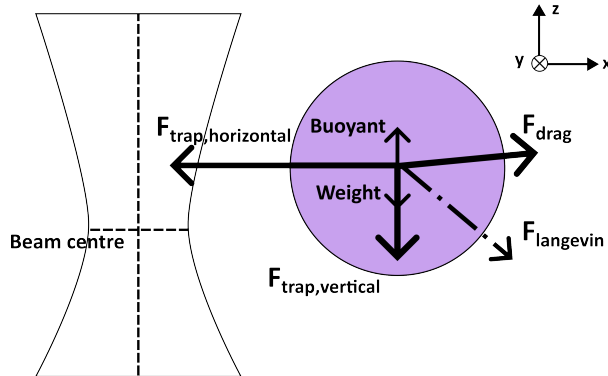


Figure 23: Free body diagram of the forces on an optically trapped microparticle

Understanding the dynamics of an optically trapped particle is important to be able to model and predict its motion so an optimal trajectory can be planned. The first step in doing this is reviewing all the forces which act on an optically trapped particle, which are depicted in Figure 23. An optically trapped particle experiences 5 main forces: optical force, gravitational force, buoyant force, viscous drag force and Langevin force (the cause of Brownian motion) [25] [26]. The optical force can be separated into a force in the x-y plane and the z-axis. For a stable optical tweezer the main z-axis forces: the buoyant force, gravitational force, and optical force in the z-direction, are considered to reach equilibrium. After reaching equilibrium, the forces in the z-axis have no impact on the lateral motion hence they will not be

considered for most of this analysis. Restricting motion to the x-y plane also means the drag force will only act in the x-y plane. Additionally, the difference between the buoyant force and gravitational force results in a force of $F = 4/3\pi R^3(\rho_s - \rho_w) = 4.19 \times 10^{-19} N$ where R is the radius of the particle, ρ_w and ρ_s are the densities of water $1000 kg m^{-3}$ and the polystyrene bead $1100 kg m^{-3}$. This is several magnitudes less than the axial trapping force so is not significant in the axial trapping analysis in Section 2.

Then in the x-y plane, there are three remaining forces, the optical force in x-y plane, the viscous drag force and the Langevin force which causes Brownian motion. Hence the dynamics of the particle are

$$m\ddot{x} = F_{trap} - F_{drag} + F_{langevin}, \quad (31)$$

where m is the cell's mass, $x \in R^{2x1}$ is the position of the particle in the x-y plane, F_{trap} is the optical trapping force, and F_{drag} is the drag force. The maximum Reynolds number of this system is

$$Re = \rho_w v D / \nu = 1 \times 10^{-3},$$

where Re is the Reynolds number, $v = 500 \mu m s^{-1}$ is the maximum velocity of the particles, $D = 2 \mu m$ is the diameter of the particles, ν is the dynamic viscosity of the medium. The effect of the inertia force in low Reynolds environments can be neglected [26], which is common in studies in cellular domain[27]. Since $Re \ll 1$, the low Reynolds environment simplification can be used. This model of fluid mechanics leads to results that would be unintuitive at macroscopic scales, such as instantaneous changes in velocity of the particle occurring. The dynamics of Equation 32 are simplified as

$$0 = F_{trap} - F_{drag} + F_{langevin}. \quad (32)$$

3.2.1 Trapping force

Having a larger trapping force is very important for the speed of the system, which is evident from Equation 36 in Section 3.2.3. To be able to model the trapping force on the particle, two ray optics simulations were used for the purposes of trajectory planning. I created the first ray-optics simulation, which is based on the method presented by Gauthier and Wallace [28] in Matlab, integrating the change in momentum of the photon stream numerically to find the trapping force. This simulation also relaxes the requirement of a strongly converging Gaussian beam and considers fewer reflections compared to the second written by Seung-bin Joo, which is presented in detail in Section 2, alongside the background of ray-optics models.

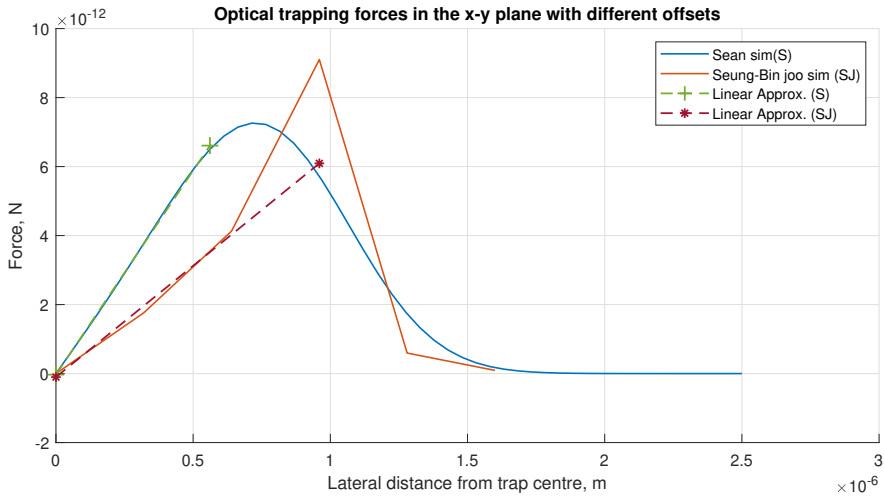


Figure 24: The x-y trapping force from the optical tweezers as offset changes. Results from Sean’s ray-optics simulation and Seung-Bin Joo’s ray optics simulation are plotted, as well line fit to the approximate linear region for each simulation using the least-squares approach. Note that the line for Seung-Bin Joo’s simulation is extrapolated to x_0 , the maximum trapping range. Line (S) gradient, $\kappa = 11.8 \text{ pN}/\mu\text{m}$, line (SJ) gradient $\kappa = 6.45 \text{ pN}/\mu\text{m}$

The principles of these two models are the same, so Section 2 can be referred to for detail on the ray-optics modelling. The assumptions in the first model still produces accurate results in the transverse direction, while greatly reducing the complexity of the simulation so it can be programmed and run more quickly. By using the first model to gain a good initial estimate of key parameters such as the trapping force magnitude and its range, this allowed the design of the trajectory planning to be completed before the second simulation in Section 2 had been finished. While the design of the trajectory planning in Section 3.5 is based on the first simulation, for this report the values from the second model in Section 2 are referenced for calculations and final estimates of speed and stability because the model of convergent rays is more representative of the physical system. It is also equivalent to taking the lowest estimate between the two simulations, leading to a lower bound estimate on the speed.

Furthermore, as specified in Section 2.1.1 and Section 3.3, there may be significant differences between theory and experiment for the trapping force. Hence, when this platform is fabricated the trap stiffness will be calibrated experimentally to get the most accurate measure to be able to plan a suitable trajectory, which is detailed in Section 3.4.

Figure 24 shows plots of the trapping force for different lateral offsets for the two ray-optics simulations. Seung-Bin Joo discusses the choice to use this type of model in detail in Section 2.1.1. The different simulations show a good general agreement given the different modelling assumptions. Both simulations

correctly show that the lateral trapping force is zero when the trap focus and microparticle are perfectly aligned. F_{trap} also increases approximately linearly until a point x_0 where F_{trap} reaches its maximum value, after which point it decreases until it zero outside the trap. Between the simulations, the maximum trapping forces are within 25% of each other, and there is a 35% difference in the distance where the maximum trapping force is achieved. One interesting difference between the graphs is that in the second simulation (SJ) the gradient of the curve increases before the maximum force after roughly $0.5\mu m$ while in the first simulation (S) the gradient of the curve decreases before the maximum force is reached. This leads to a very large difference in trap stiffness once a line is fit to these curves, even though the maximum forces and displacements aren't as different.

The trapping force is approximated as

$$F_{trap}(x) = \begin{cases} \kappa_t x, & \text{if } 0 < x < r_0 \\ 0 & \text{if otherwise,} \end{cases} \quad (33)$$

where κ is the "trap stiffness" of the optical trap, and κ_t is the trap stiffness measured for trajectory planning. This leads to a value of $\kappa_t = 6.45 pN/\mu m$ being used from the second simulation. This is the minimum gradient in the approximately linear region of trapping force in Figure 24, which is used as having an underestimate of the force in the region near r_0 is preferable to overestimating the trap stiffness which can lead to a trajectory that leads the particle escaping. The trajectory will be planned so that the offset x is always less than r_0 so that Equation 33 is valid. If the particle has an offset greater than r_0 , the magnitude of F_{trap} will decrease regardless and lead to the particle escaping.

3.2.2 Drag force

The drag force on the particle can be calculated with Stoke's Law — an empirical law for calculating the drag force on spherical objects with very small Reynolds numbers in a viscous fluid as follows:

$$F_{drag} = \beta \dot{x}. \quad (34)$$

Where

$$\beta = \frac{6\pi\eta R}{1 - \frac{9}{16}(r/h) + \frac{1}{8}(r/h)^3 - \frac{45}{256}(R/h)^4 - \frac{1}{16}(R/h)^5} \quad (35)$$

is the drag coefficient, η is the solution viscosity, and h is the distance from the bottom surface of the container to the particle center. The denominator of 35 is from Faxén's law which is a correction to

Stokes' law for the friction on spherical objects in a viscous fluid, which is valid when the object moves close to a wall of the container[29]. In Stoke's law the following assumptions are made: laminar flow; no inertial effects (zero Reynolds number); spherical particles; homogenous material; smooth surfaces and that particles do not interfere with each other.

These assumptions should be true in this system. As discussed above the maximum Reynolds number is low enough to assume there are no inertial effects. One point to note is that the smoothness of the microparticle may depend on the coating. However, this should still provide a very good estimate of the drag force. In the path planning the particles will also be made to take paths which do not come into very close proximity with each other to avoid interference.

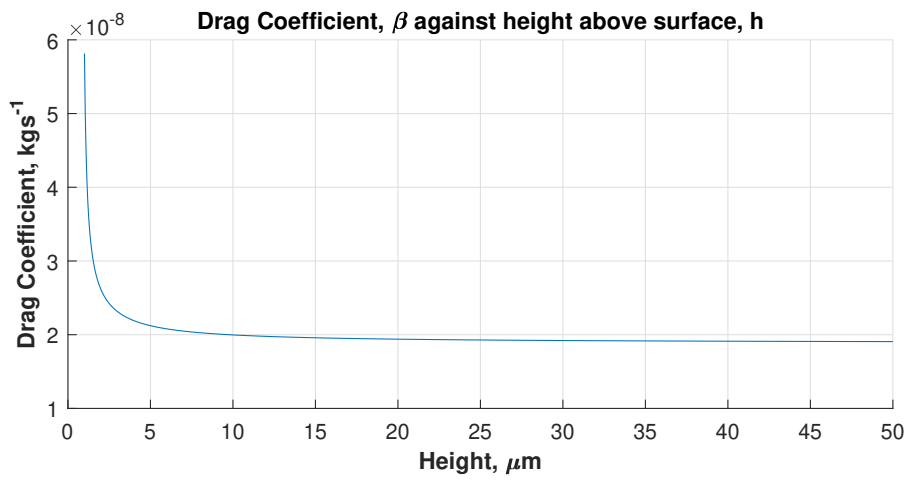


Figure 25: A graph of drag coefficient against height above the surface for a 1 micrometre radius particle

Figure 25 shows the variation of the drag coefficient with height above the container surface. Note that the plot starts at a height of 1 micrometre as h is measured from the centre of the particle. Very close to the wall the drag greatly increases, and it tends towards an asymptotic value of 0.0188kg s^{-1} as h tends to infinity. A distance of at least 2 micrometres should be maintained, otherwise the particle will slow down dramatically and will likely be lost from the trap.

As the particles are tweezed above the cells, the drag coefficient will vary as the distance to the cell/container surface varies. Since the maximum cell diameter is 30 micrometres, as stated in Section 1, it is suggested that particles are tweezed at a minimum height of 36 micrometres. When the microparticle is directly above the cell, h will be a minimum of 6 micrometres resulting in a drag coefficient of 2.08×10^{-8} and when the microparticle is not above any cells, h will be 36 micrometres resulting in a drag coefficient of 1.91×10^{-8} . This is a maximum 8.9% change.

3.2.3 Maximum particle speed

The maximum particle speed in an optical trap (which the particle instantaneously accelerates to when a trap is applied), is given as:

$$v_{max} = \frac{F_{trap,max}}{\beta} \approx \frac{\kappa r_0}{\beta} \quad (36)$$

Using the values calculated above the maximum velocity of tweezing would then be approximately $438\mu m/s$ using a peak force of $F_{trap,max} = 9.1pN$ from Seung-Bin Joo's simulation referred to in Section 3.2.1 and calculated in Section 2. However, this would require the traps to move continuously i.e. for the SLM to have an infinite refresh rate. The effect of a finite SLM refresh rate on trajectory planning is considered in Section 3.5.

3.3 Parameter uncertainty

When looking at maximum trapping speed in Equation 36 there are several factors that can impact v_{max} . First of all the parameter β may vary. Equation 35 indicates how drag coefficient β depends on separation depth and viscosity coefficient ν . It has been stated that the liquid medium may vaporise as the cell moves and the variations in the chamber may cause a change in h [30]. Additionally, ν may have different values in different places in the medium which may also cause variation in β as the cell moves.

Furthermore, the trapping force will also be affected by multiple factors. First of all the ray-optics approximation will not provide a perfect estimate, with some papers having errors of more than 30% [31], then there will also be variations in shape and intensity of laser beam because of an unstable laser source, and polarisation could have an impact as that would change the reflection coefficients for transmission and reflection. Wu et al. [31] mentions the variation of refractive index due to the coating of the particle as a particular reason that numerical calculations may be different from the experimental result. Other disturbances such as Langevin forces and stage mechanical vibrations will also be present.

Hence it is very important to calculate the trap stiffness experimentally to ensure than values for r_0 and κ are known, otherwise the system may not be able to function autonomously and the microparticle may escape the trap or will underperform in speed. This is important in planning an ideal trajectory.

3.4 Trapping stiffness calibration

There has been significant effort on experimentally measuring trap stiffness as accurately as possible, resulting in several different methods. In general, using multiple methods is recommended to ensure accuracy of the results. After research into the various techniques, two complimentary methods were

chosen to ensure calibration could be completed as quickly and accurately as possible. These are the Equipartition Theorem method and Drag Force method. The combinations of these methods allow for rapid measurement of trap stiffness independent of drag force using the Equipartition Theorem and also a characterisation of the tweezing force for the whole linear regime using the drag force method. In practice, during a first time calibration both methods should be used. After this, if the set up of the system does not change the trapping stiffness should not vary significantly so the faster Equipartition Theorem can be used subsequently to confirm the system is function correctly. Once implemented, both methods should agree to within 10% [32]. The first two methods require the addition of a position sensitive detector system, which will add a mirror, Quadrant Position Detector and a low power CW laser to the optical layout. This can be seen in the optical layout in Section 1. However, these are inexpensive components, costing less than £200 in total. A summary of the theory behind these methods is given below.

3.4.1 Drag Force Method

This is usually done by having a particle in a fixed trap and using a motorised stage to create a flow in the fluid which creates a viscous drag force on the particle (after a small time the fluid velocity is equal to the stage velocity). Then the trapping force can be calculated using Equations 32, 33 and 34 to give:

$$\kappa = \beta * v_{fluid} / \Delta x, \quad (37)$$

where v_{fluid} is the velocity of the fluid when the particle has reached equilibrium, and Δx is the displacement from the trap centre. The Langevin forces are not considered here.

Hence, the constant fluid velocity creates a constant displacement from the centre of the trap. This is measured at a series of different stage velocities, which allows the force to be calculated at several displacements until r_0 , which can be used to examine the linearity of the trapping. This cannot be done with any other method. The velocity of the fluid can either be referenced from the stage or by using a video. An accuracy of 10% can be achieved by obtaining particle speed from the video, with a larger accuracy from using a computer controlled stage [33]. Since β , the viscous drag on the particle must be known, this method is best suited to uniform spherical particles, where Stokes Law and Faxen's Law mentioned above can be used to explicitly calculate the drag. Otherwise, the drag is more difficult to calculate for irregularly shaped particles. This is ideal for this system, which uses spherical polystyrene beads. Triangle waves of the displacement of the stage can be used (leading to constant fluid velocities and hence drag forces from Equation 34). In addition, drag force measurements are slow compared to

the Brownian motion of the particle, so the bandwidth requirements of the detection system are relaxed and a video camera can be used. Having a higher frequency camera is beneficial for this process.

3.4.2 Equipartition Theorem Method

This method requires a calibrated position sensitive detector. It works by calculating the variance in the Brownian motion of a trapped particle. From the Equipartition theorem, the energy in the Brownian motion of the trapped bead is equal to $\frac{1}{2}k_B T$ [32], and the energy stored in the trapped spring (since we are operating in the linear trapping regime) is equal to half the spring constant, κ times the variance in the motion $\langle x^2 \rangle$. Setting these two energies equal and solving for the stiffness gives

$$\kappa = \frac{\langle x^2 \rangle}{k_B T}. \quad (38)$$

A high analog bandwidth/precision of position measurement is necessary, but since the position signal has random phase aliasing artifacts will not need to be considered, so the digital sample rate does not need to be correspondingly high [33]. This can measure trap stiffness very quickly, in less than a second.

3.5 Optical Tweezer Trajectory Planning

Due to the variation in the parameters involved in the dynamics of the optical tweezers, the trajectory of the particles and the sequence of optical traps must be carefully designed. This section focuses on the planning of this trajectory in the x-y plane. In this Section it is shown that the main limitation for the speed of the microparticle is the time constant τ and the frequency of Spatial Light Modulator (SLM) used. For this analysis two key assumptions are made: There is no delay in obtaining information from the real-time image position of particles and that in the holographical optical tweezer system in Section 2.3 and that the optical trap is placed without delay. These assumptions have been used in other research for the control of multiple cells manipulated by optical tweezers [34].

Specific design objectives are set for this system:

- Robustness to adjustment of the time constant $\beta/k \pm 10\%$.
- Movement of the particle as quickly as possible
- Robustness to Brownian motion

3.5.1 Particle motion for a single trap

First, it is useful to look at the dynamics of a particle for a step response of the trap. Note that for most of this analysis we consider that the Brownian motion is negligible to be able to find simple analytical

solutions for particle trajectory, and it will be added as noise in the optical tweezer simulation later. The general curve is an exponential decay convergence from the initial particle position to the trap position. The same model can be found in over-damped mass spring models or RC circuits. The time constant for the optical trapping would be $\tau = b/k$. With the values calculated in Sections 3.2.1 and 3.2.2, $\tau = 2.08 \times 10^{-8}/6.45 \times 10^{-6} = 310.1\text{Hz}$ and $r_0 = 0.96\mu\text{m}$.

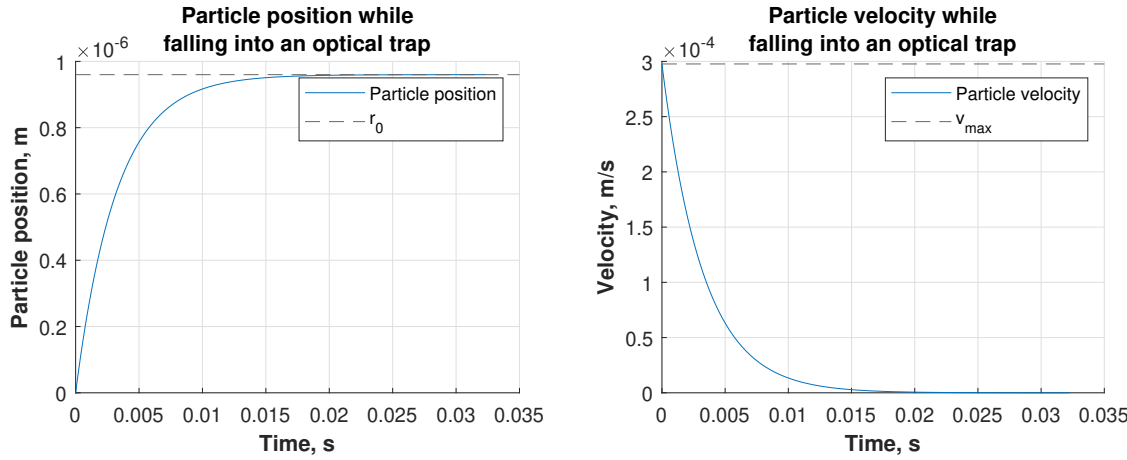


Figure 26: A plot of the position of a particle and its velocity as it falls into an optical trap placed at the limit of the linear regime. At $t = \tau$ particle position reaches 63% of its asymptotic value while particle velocity decreases to 37% of its original value. At $t = 3\tau$ particle position reaches 95% of its asymptotic value while particle velocity decreases to 5% of its original value.

For a single step, with a trap position of $u_1 = r_0$ and initial position of $x_0 = 0$ the particle trajectory is

$$x(t) = r_0 + (0 - r_0)e^{-k/\beta t}. \quad (39)$$

Taking the derivative of this to find the velocity of the particle we have

$$\frac{dx}{dt} = k/\beta(r_0)e^{-k/\beta t} = v_{max}e^{-k/\beta t}. \quad (40)$$

where v_{max} is the maximum velocity of the particle when it is at the very edge of the trap. The particle position and velocity falling into a single optical trap is plotted in Figure 26. From this it is clear that there is a trade off between prioritising speed or velocity. Having a low refresh rate and moving the trap at $t \lesssim \tau$ means that the average velocity is higher, as the trap is refreshed before the velocity reaches the flat region at larger t . However, this means that the trap will move before the particle position has settled, so if τ varies from the experimental evaluation, there will be a large error in the predicted position of the particle which can accumulate over time. Similar considerations can be applied for moving the trap at a

timing of $t \gtrsim \tau$, where the position of the particle before moving the trap will have a low margin of error, but the velocity of the particle for larger t will be very small—leading to an overall lower velocity.

3.5.2 Particle motion in a sequence of optical traps

The motion of the particle for a particle step can be generalised, and the displacement x_i at the end of a particle time window i is given as

$$x_i = u_i + (x_{i-1} - u_i)e^{-k/\beta t_{refresh}}, \quad (41)$$

where $u_i = \lambda i$ is the optical trap position for the time window i . The time window i increments each time the optical trap is moved after $t_{refresh}$. θ is the step size of the optical trap each iteration. This can be rewritten as a fixed proportion of the linear regime limit $\theta = qr_0$ (e.g. for $q = 0.9$, $\theta_1 = 0.9r_0$, $\theta_2 = 1.8r_0$, $\theta_3 = 2.7r_0$), where q is the trap spacing coefficient and is a real number between 0 and 1.

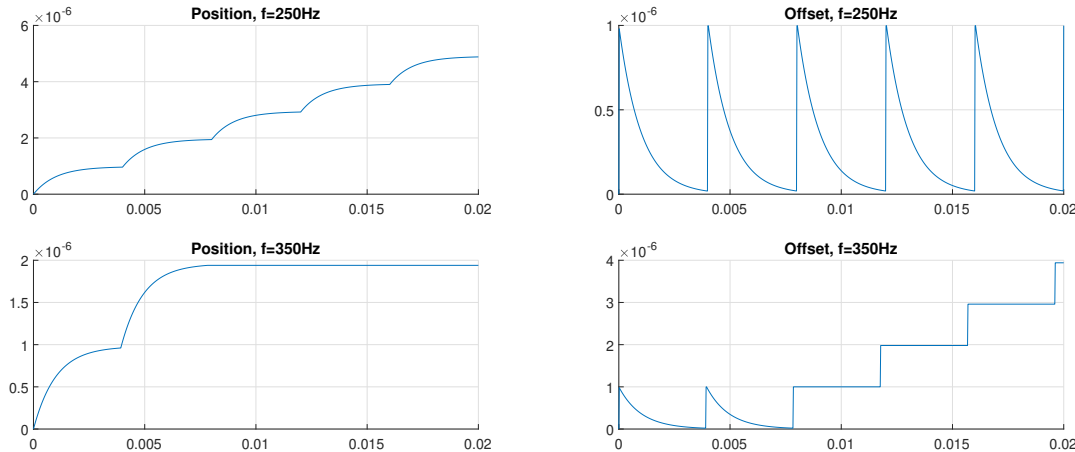


Figure 27: The particle motion for a series of optical traps. The graphs on the left show the particle's displacement over time, while the graphs on the right show the absolute offset from the *most recently placed* optical trap. τ and r_0 are the same as stated above. These plots show for $q = 0.9$ the particle eventually escapes at 350Hz but not 250Hz.

The optical trap cannot be moved by r_0 each iteration or the particle will fall out the trap, which is clear from Equation 39 which shows that for any step of the optical trap, the particle will never reach its exact position. Therefore, for a particular refresh time for the SLM $t_{refresh}$, the maximum value of θ needs to be found to ensure the particle moves as quickly as possible without escaping the trap. As example of this effect, Figure 27 shows a simulation of particle movement with $q = 0.9$, showing that at 350Hz the particle escapes in the third time window, while it is stable at 250Hz.

3.5.3 Calculating optimum trap spacing coefficient

We can solve the problem of finding the optimum value of q for a given refresh rate by creating an analytical equation for the offset of the trap at the end of time window i . By writing offset o_i as

$$o_i = x_i - u_i. \quad (42)$$

The maximum displacement of a trap is $d = o_i + \theta$ at the beginning of the time window when the trap has just moved. To maintain trapped, the inequality $d < r_0$ must hold. Equation 41 can be rewritten as

$$x_i = u_i + (u_{i-1} - u_i + o_{i-1})e^{-k/\beta t_{refresh}}. \quad (43)$$

Hence

$$o_i = (o_{i-1} - \theta)e^{-k/\beta t_{refresh}}. \quad (44)$$

If $x_0 = 0$ (meaning $o_0 = 0$), then offset can be rewritten as a geometric series:

$$o_i = \theta \left(\sum_{n=1}^i e^{-k/\beta t_{refresh}} \right). \quad (45)$$

By rewriting θ as qr_0 and by introducing the inequality $d < r_0$ the following equation can be written:

$$q \left(\sum_{n=0}^i e^{-k/\beta t_{refresh}} \right) < 1. \quad (46)$$

Provided that $|e^{-k/\beta t_{refresh}}| < 1$, which is true for all possible parameters, the value of the sum of this geometric series converges, which is not clear at first glance. The sum evaluated as i tends to infinity leads to the inequality

$$q \frac{1}{1 - e^{-k/\beta t_{refresh}}} < 1. \quad (47)$$

This gives a restriction on the maximum value of q for a certain choice of parameters k, β and $t_{refresh}$. This means that given a certain time constant τ and refresh rate t_r , a certain q can be chosen to ensure that the particle never escapes the trap. However, this means that the offset converges to $d = r_0$ as time window i increases, which is on the very limit of the linear regime, so instead q is set as

$$q \leq 0.95 \left(1 - e^{-k/\beta t_{refresh}} \right) - \frac{r_0}{\Delta x_{brownian}}. \quad (48)$$

A coefficient of 0.95 is used so that the offset instead converges to approximately $d = 0.95r_0$ as i tends to infinity, and $\Delta x_{brownian} = 0.039\mu m$ is the mean absolute deviation of the Brownian motion calculated in Section 2.2. The last term in Equation 48 effectively subtracts $\Delta x_{brownian}$ from θ to ensure that Langevin forces do not allow the trapped particle to escape. $\Delta x_{brownian}$ has a value approximately 4% of the value of r_0 , hence it only has an impact at very high refresh rates, where q becomes very small. The maximum q for different SLM frequencies from Equation 48 is plotted in Figure 28. As expected, the higher the SLM frequency the lower q must be to maintain the particle within the trapping regime.

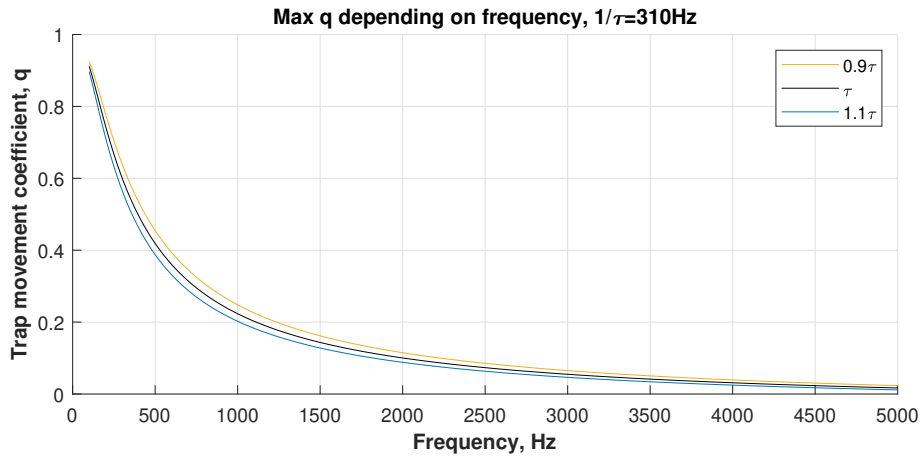


Figure 28: A plot of the maximum trap spacing coefficient q for stable trapping given SLM frequency

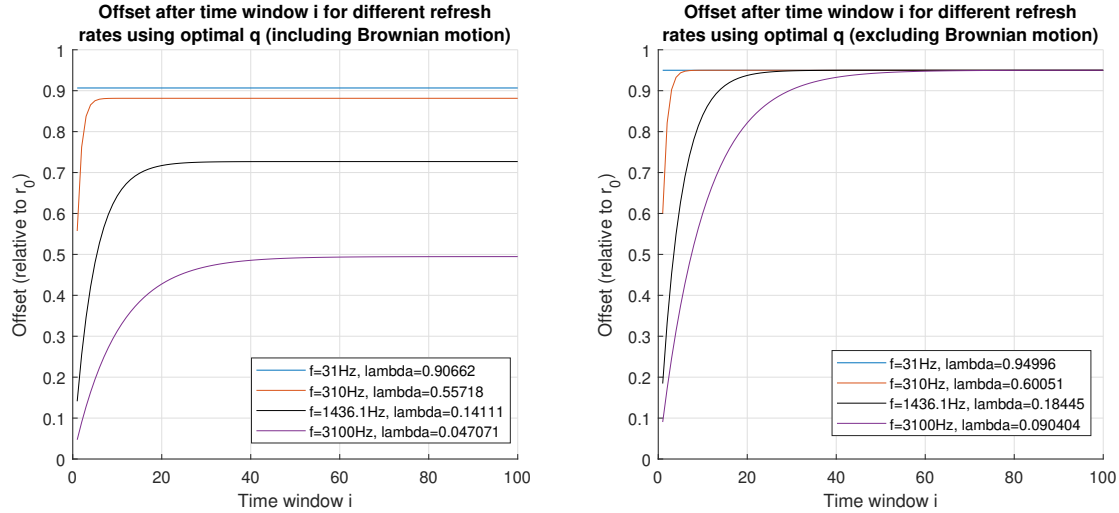


Figure 29: A plot of particle offset after time window i for different SLM frequencies of 31Hz, 310Hz, 1436.1Hz and 3100Hz. This corresponds to $t_{refresh}/\tau$ of 0.1, 1, 4.63 and 10.

Figure 29 shows how the offset from the optical trap position at the end of time window i from Equation 45 increases with iteration i . It can be seen that after a certain number of iterations an "equilibrium is reached", where the offset stays constant regardless of iteration. The number of iterations needed

to reach this asymptote is controlled by $t_{refresh}/\tau$, however note that while the number of iterations to converge is larger for smaller $t_{refresh}/\tau$, the physical time this takes actually decreases in Figure 29 because the duration of each time window also decreases. The plotted offset calculated with Equation 45 is done for the value of q calculated with Equation 48 with and without the Brownian term. Note that the offset relative to r_0 decreases greatly for high refresh rates when q is calculated with the Brownian term. This is because the Brownian motion has a greater effect at higher refresh rates because at these refresh rates the trap is moved by smaller increments each time window i , and hence the effect of Langevin forces becomes more prominent relative to the distance θ .

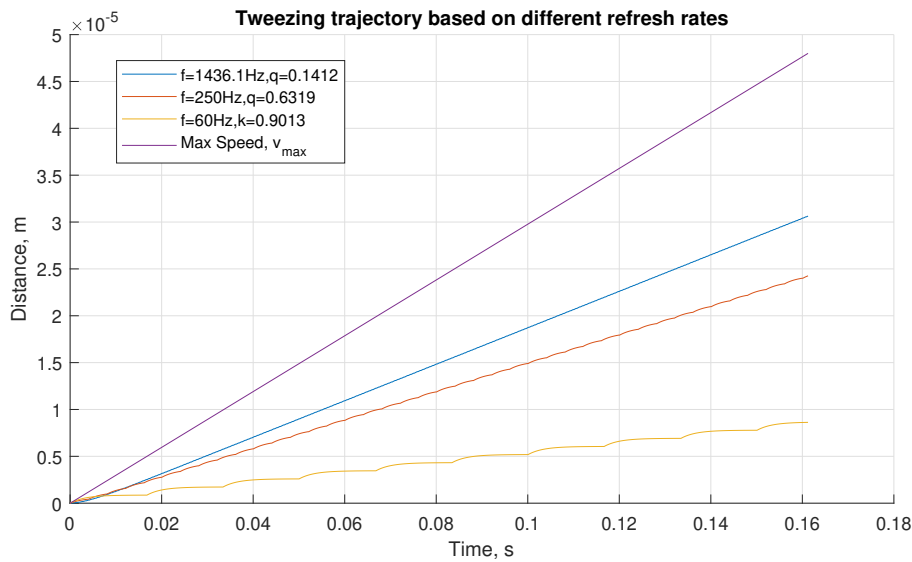


Figure 30: The stable trapping trajectories for $f=60Hz$, $250Hz$ and $1436.1Hz$, as well as a theoretically maximum speed based on $\kappa_t = 6.45pN\mu m$.

Finally, Figure 30 shows the different optimum optical trap trajectories for different refresh rates of the SLM. It is clear that increasing the refresh rate leads to a large increase in the speed as expected. The values of q selected were calculated with Equation 47, which lead to stable optical tweezer trajectories. The theoretical maximum speed $v_{max} = 297.7\mu m/s$ is calculated using Equation 36 from Section 3.2.1, with $\kappa_t = 6.45pN\mu m$ and $r_0 = 0.96\mu m$. Note that the true max speed if the SLM was continuously moved would be higher since κ_t underestimates the maximum trapping force. At an SLM frequency of $1436.1Hz$ the particle moved $30.6\mu m$ in 0.161 seconds, which corresponds to a speed of $190\mu m/s$. Calculating speed in the same way for $f = 250Hz$ and $f = 60Hz$ gives values of $150.1\mu m/s$ and $53.5\mu m/s$ respectively. This justifies the decision to use a higher frequency SLM, as it allows the ability to move the microparticles much more quickly (SLMs are more commonly manufactured at $60Hz$).

3.5.4 Total trajectory speed and path planning

Overall we have shown that each microparticle can be stably moved at a maximum speed of $190\mu\text{m}/\text{s}$. Given that the average distance they must cover is $23.5\mu\text{m}$ as mentioned in Section 1, the particle will take 124ms to move into position on average. Since the distribution of microparticles within the medium is essentially random, the distance they have to cover will vary as well. This is not explicitly modelled, but an adjustment is made of a factor of 2, so that all particles should be in position within 248ms .

Now that a method for planning a trajectory in the x-y direction has been completed, an overview of the overall path planning process can be made. For x-y motion, widefield imaging operates at 150Hz, while the SLM frequency is 1436.1Hz, with time periods t_w and $t_{refresh}$ respectively. Firstly, a trajectory will be planned between each microparticle and the specific cell entry cite in the x-y direction, considering the maximum stable speed calculated above. After the position of the particles have been located in the widefield imaging, a sequence of optical traps will be generated to move the particles in their chosen trajectories. After ten refresh cycles, $t_{refresh}$ have elapsed, t_w will have also passed and another image is taken to show that the particles have been following their planned trajectories and to calculate the next sequence of optical traps. To avoid collisions A* pathfinding can be used to navigate around obstacles and particle speed may also be adjusted. Once all the microparticles are above the specific site on the cells where they will be inserted, they are kept trapped in the same position in the x-y plane while the focus of the objective lens changes and moves the optical trap down in the z-direction. This can happen at approximately a velocity of $0.3p\text{N}/2.08 \times 10^{-8}\text{kgs}^{-1} = 14.4\mu\text{m}/\text{s}$, applying Equation 36 in the axial direction. Hence over a distance of $6\mu\text{m}$ as specified in Section 3.2.2 this will take approximately 420ms .

3.6 Summary

In conclusion, this section has covered the theory behind the implementation of an optical tweezer system. First, an overview of the forces on an optically trapped particle was completed alongside a simulation of the optical trapping force to be give values of trap stiffness $\kappa = 6.45p\text{N}/\text{m}$ and trap range $r_0 = 0.96\mu\text{m}$ for the rest of the trajectory analysis. Then a calibration procedure was chosen so that the trap stiffness of the optical trap could be experimentally measured given the gap between the ray-optics model and actual trapping force on the microparticle. Finally, the analysis of the optical tweezer dynamics alongside the work in Section 2.2 was used to be able to plan stable trajectories for the microparticles which move them as fast as possible at $190\mu\text{m}/\text{s}$. This primarily consisted of optimising the trap movement coefficient q with respect to the SLM refresh frequency given the time constant of the optical trap dynamics τ .

4 Laser ablation system - Sean Mata

4.1 Introduction

This laser ablation/optical injection system has the primary responsibility for creating a pore in the cell membrane once the particle have been moved by the optical tweezer system to a suitable position so that the $2\mu m$ particles can then be moved into the cell. Optical injection offers several advantages over microinjection, its main alternative. It is non-invasive which reduces contamination risk, and can be performed through a sterile coverslip[35]. Furthermore, it has high cell injection efficiencies, preserves cell viability, and integrates seamlessly with other microscopic techniques, a key feature of our platform.

To create the pore, an 80MHz femtosecond pulsed laser is used which is shared by the chemical imaging system in Section 6 and the ablation system in this section. $3\mu m$ temporary pores are created in the cell membrane by irradiating the cells for a $100ms$ duration with the femtosecond laser. The beam profile has an axial range of $30\mu m$ which is achieved by using an axicon-generated Bessel beam. Additionally, by using a shutter and power control system, the length of the irradiation window and energy per pulse can be adjusted. The power and precision of the laser also mean that this platform could easily adapted to perform intracellular dissection, chromosome ablation and extraction or laser transfection without optical tweezers (by immersing cells in a solution of membrane impermeable drugs). In the rest of this report, an overview of the optical layout is first provided in Section 4.3 followed by the technical analysis of different parameter and design choices. These include the choice of pulse width, repetition rate, irradiation time and average power of the laser in Section 4.4, the numerical aperture of the objective lens in Section 4.4.3 and the parameters of the axicon used to generate the Bessel beam profile in Section 4.5. Finally, an overview of the safety of the ablation system is included.

4.1.1 Background

This system employs a variation of photoporation-induced optical injection (or transfection). Optical transfection typically involves exposing a solution of a specific substance to be inserted into cells, followed by photoporation to create a transient pore in the membrane [35][36]. In our platform, a transient pore is created using laser light, but instead of passive diffusion, a drug-coated microparticle is actively moved into the cell using optical tweezers. This addresses a challenge with optical transfection, where high substance concentrations around cells make precise dosing difficult [37]. Throughout this report, we'll refer to this process as laser ablation or optical injection, while the passive substance entry into cells is termed optical transfection.

4.2 Design specification

There are several variables that will affect the design choices in this report. These are summarised here:

- **Speed:** The ablation process takes approximately $40 - 100\text{ms}$. This should be minimised to ensure the platform can process cells as quickly as possible.
- **Cell viability:** Photodamage and thermal damage must be minimised. This means that spot size should be as small as possible and particular wavelengths are better—if possible, near-infrared wavelengths are optimal. Additionally, the power of the laser dose should be able to be specified.
- **Insertion efficiency:** This is defined as the percentage of microparticles that are successfully inserted into the cell for each attempt. In general, the larger the pore size, the higher the insertion efficiency may be. This will require a specific intensity and power distribution.
- **Sub-cellular targeting precision:** The radial spot size of the output of the laser must be small enough to reach the necessary longitudinal and axial precision. This should be no larger than $1\mu\text{m}$.
- **No fluorescence used:** Certain types of lasers such as continuous wave lasers can use fluorescent particles to increase precision[38][39]. This should be avoided.
- **Axial range:** Using an objective with a high Numerical Aperture means that the beam divergence from the focal plane increases (e.g. $2 - 4\mu\text{m}$ confocal parameter for a Gaussian beam). Since this technique is very sensitive to axial misalignment of the objective, this should be taken into account.

Additionally, other important design criteria such as the cost of the system and the ability for it to be controlled autonomously as stated in the introduction factor into the analysis in this report.

4.3 System overview/Optical Layout

In this section, the optical layout designed for the laser ablation system is shown first in Figure 31 alongside a summary of each section and their key parameters. The analysis completed to create this optical layout, involving various parameter and design choices are included in Sections 4.4—4.5.

4.3.1 Laser

The laser used is a Chameleon Discovery NX Ti:Sapphire Laser system. It combines a femtosecond pulsed Ti:Sapphire laser with an Optical Parametric Oscillator. This is shared with the CARS imaging system described in Section 6 to reduce cost. The key parameters are relevant to this system are Wavelength $\lambda = 800\text{nm}$; Repetition rate = 80MHz ; Pulse width = 100fs ; Beam waist $\omega_0 = 1.2\text{mm}$; Beam type:

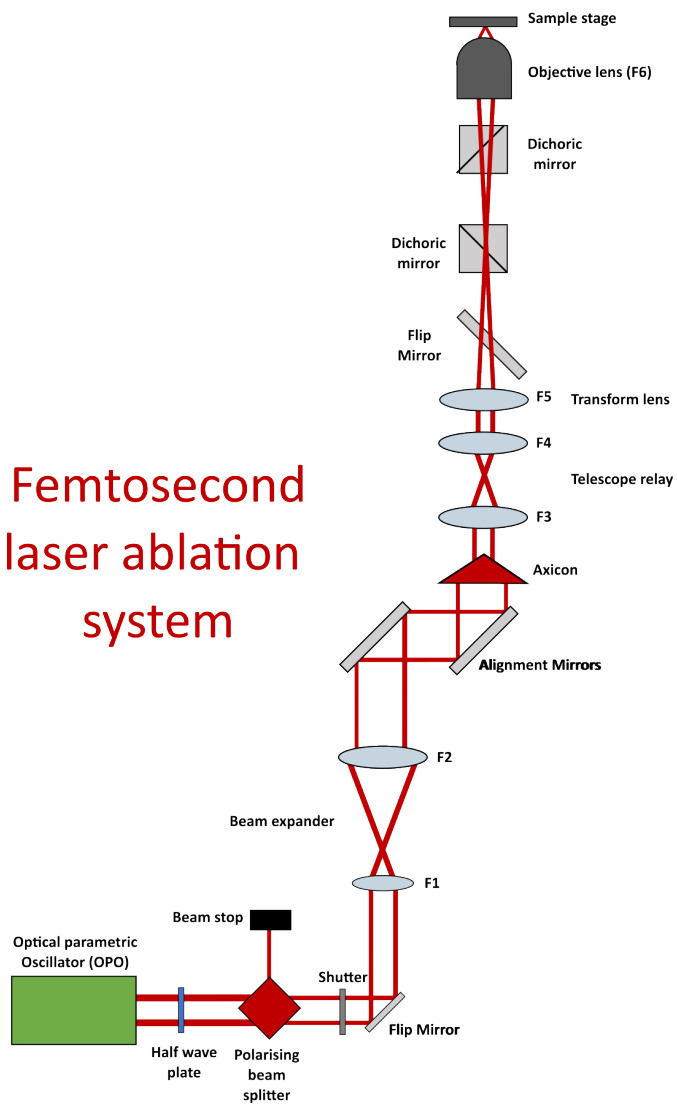


Figure 31: Ablation system optical layout

TEM00 (Gaussian); Output power = 3600mW. The decision to use this laser is covered in Section 4.4.

4.3.2 Power control - Half wave plate and Polarising Cube Beam Splitter

The power control for the ablation laser is completed by using a Polarising Beam Splitter (PBS) and a Half Wave Plate in series. At the Polarising Beam Splitter, the P polarisation of incident light passes through the cube with minimal loss, while the S polatisation is reflected out. It is important that the beam dump is present for safety, as laser light escaping the system could cause vision damage.

To be able to adjust the amount of light that passes through the PBS the half wave plate is used. A zero order $\frac{1}{2}$ wave plate is used which introduces a π phase difference between the two components of light perpendicular and parallel to its optical axis. For linearly polarised light input, this means that the plane of the light is rotated. Rotation of the half wave plate by ϕ degrees leads to 2ϕ degrees of polarisation

rotation. Then according to Malus' law [40] the intensity of light that passes through the beam splitter is

$$I = I_0 \cos^2(2\phi) \quad (49)$$

where I_0 is the input intensity and ϕ is the azimuthal angle of the half wave plate. Hence the intensity can be completely modulated from 0 to I_0 by rotating the half wave plate between 0 and 45 degrees using a rotation mount. This is suited for high power applications and offers the ability to continuously tune the output power of the laser, as opposed to using a series of Neutral Density filters which would only allow fixed amounts of attenuation. For the output power necessary of $2.11W$ needed to have a power of $0.75W$ at the sample, calculated in Section 4.3.8 using the transmission efficiency of this system, an angle of $\phi = 20.02^\circ$ is needed for the half wave plate. To ensure the power at the sample does not vary more than $0.01W$, the angle must not vary more than 0.206 degrees. This can be achieved with the Thorlabs ORIC® Rotation Stage. The output power will be calibrated manually during setup with a power meter.

4.3.3 Mechanical shutter

The cell is irradiated for a duration on the order of tens of milliseconds. The shutter needs to be suitable for high power pulsed near-infrared irradiation as well as a maximum rise time and fall time of 1ms and accuracy of at least 1ms. This is achieved with the Newport Electronic Shutter model 76992 with a 0.77ms rise time and a 0.88ms fall time and a damage threshold of more than 5W for a 1.2mm beam waist, which will safely absorb the incident beam. The shutter controller used is the 76995 Electronic Shutter Driver, however a custom transistor logic pulse generator could also be designed.

4.3.4 Beam expander

Since the output from the laser has a beam waist 1.25mm, it is decreased by factor 5 by the beam expander to achieve a value of $\omega_1 = 0.25mm$ in Section 4.5.3. Hence lenses F1 and F2 have focal distances of 10mm and 50mm.

4.3.5 Axicon

This is responsible for shaping the laser into a Bessel Beam. The key parameters are: Refractive index: $n = 1.5$; Beam waist input: $0.25mm$; Axicon angle: 8° . The selection of these parameters is discussed in detail in Section 4.5.

4.3.6 Transform lens + Telescope relay

In this section an overall beam expansion of factor 1/8 need to occur from the calculations in Section 4.5.3. The lens F3 transforms the Bessel beam into an annular intensity distribution, and then lenses F4

and F5 act as a telescope relay. The focal lengths of the lenses are specified as F3: 40mm, F4:10mm, F5:80mm, F6 (objective lens): 2.525mm. Hence $F3/F4=4$ and $F5/F6\approx1/32$.

4.3.7 Objective lens

The Objective chosen for our platform is MRL07920 manufactured by Nikon. It has a numerical aperture of 1.1 and a focal length of $F6=2.52\text{mm}$. This is shared between all systems, as shown in Section 1. The of numerical aperture on this system is examined in Section 4.4.3.

4.3.8 Transmission efficiency of system

The optical components that the ablation laser must pass through are as follows, with the relevant efficiencies per component bracketed: 1 cube beamsplitter (92%), 1 half wave plate (98%), 1 flip mirror (92%), 2 alignment mirrors (92%), 1 axicon (92%), transmission through 2 dichoric mirrors (92% each), 5 lenses (98%) and the objective lens (72%). This gives an overall optical efficiency of

$$0.92^7 \times 0.98^6 \times 0.72 = 35.6\%.$$

This means that the femtosecond laser must have an output power of at least $0.75W \times 1/38.7\% = 2.107W$, where $0.75W$ is the power at the sample necessary chosen in Section 4.5.

4.3.9 Costs

The estimated cost for all the components in the optical layout is shown in Table 3.

4.4 Laser parameter analysis

There are several parameters that need to be specified for the femtosecond laser to match the design requirements in Section 4.2 as best as possible. In this section the choice of pulse width, wavelength, numerical aperture, repetition rate and irradiation time are discussed. In Section 4.5 the design of the Bessel beam shaping is considered, which dictates the focal lengths of the different lenses and axicon parameters.

4.4.1 Pulse width selection

The pulse width has a large impact on the functioning of the system, leading to very different ablation mechanisms and significantly impacting cost and precision of the laser. Laser transfection methods have utilized a range of pulse widths, from continuous wave to femtosecond pulsed lasers. A multi-criteria analysis was completed in Table 4 based on data for continuous wave, nanosecond, picosecond and femtosecond lasers compiled from different reviews on optical transfection [36][39] as well as other research papers. Weighting were based on the design specification in Section 4.2. To reference "Cost"

Table 3: Itemised cost for the ablation system

Ablation components	Quantity	Price (£)	Total (£)
Shutter	1	2100	2100
Shutter controller	1	2100	2100
Lenses	5	80	400
Alignment mirrors	2	80	160
Axicon	1	5000	5000
			Total: £9760
Shared components(CARS Imaging System)			
Half wave plate	1	200	200
Polarising beam splitter	1	200	200
Rotation stage	1	2100	2100
Rotation stage controller	1	2100	2100
Chameleon Discovery NX	1	100,000	100,000
			Total: £104,600
Shared components (general)			
Objective lens	1	28000	28000
Dichoric mirror	2	1500	3000
Flip mirror	1	120	120
			Total: £31,120
Overall total cost of related components: £145,480			

column only the price of the laser was used, where approximate prices were obtained from Laser Diode Source [41]. Cell transfection efficiency references to cell transfection where substances passively enter the cell, but this still gives a good measure for the effectiveness of a particular method.

Femtosecond-pulsed lasers emerged as the preferred choice due to their high cell viability and transfection efficiency (cell viabilities greater than or equal to 90% are often reported [36]), despite being the most expensive. They also have the least collateral damage due to their multiphoton absorption mechanism, with the effect of this being examined in Section 4.4.4. Femtosecond lasers minimise heating effects as well as collateral damage, and eliminate the need for fluorescent staining [36][38]. In general, as the duration of the pulses becomes shorter, a lower irradiation threshold is required for membrane poration and hence the induced mechanical effects and collateral damage decreases. Sharing the laser with the CARS imaging system in Section 6 additionally reduces its effective cost. Continuous wave and nanosecond lasers, while less expensive, lack the precision of femtosecond pulses and often have much lower cell viabilities [36].

4.4.2 Repetition rate and ablation mechanism

For this platform a femtosecond laser with a repetition rate of 80MHz regime was used as this means that the laser could be shared with the chemical imaging system laser in Section 6 and because more data was

Table 4: Multi-criteria analysis of the different pulse widths. Each pulse width and category pair was given a score ranging from 1 to 10. Weightings of each category are shown in the column headers. Total scores out of 10 shown in red.

Pulsing	Cost (10%)	Precision (20%)	No fluorescence used (30%)	Cell viability/ collateral damage (20%)	Cell transfection efficiency (20%)	Total
CW	9	4	0	2	2	2.5
ns	6	4	10	4	4	6
ps	4	4	10	6	6	6.6
fs	2	8	10	9	9	8.4

available on the effects compared to the 1kHz repetition rate. Dissection at the 80 MHz repetition rate is performed in the low-density plasma regime at pulse energies well below the optical breakdown threshold and only slightly higher than used for nonlinear imaging [38]. The exact mechanisms of photoporation are not fully understood[42], however it is known that it is mediated by the breaking of chemical bonds in the cell membrane due to a low density plasma of free electrons created by the incident light. Heating or thermoelastic stresses do not have a major contribution to ablation in this regime. The shape of the free-electron distribution alongside parameters such as irradiation time control the size of the pore creation, where the non-linear absorption of photons leads to a higher precision compared to lower pulse rates.

4.4.3 Spot size-Numerical aperture and Wavelength

The focus of this analysis is to be able to examine the spot size of the free-electron distribution that controls the photoporation. Having a spot size that is as small as possible is ideal since it enables a greater level of precision, where the pore size can be increased relative to the initial spot size by increasing irradiation time. In general, using smaller wavelengths also decreases the spot size but increases the amount of photodamage on the cells. Additionally, a smaller focal volume means heating effects are localised and that heat can dissipate more quickly in all directions, leading to less overall temperature increase of the cell. Furthermore, it means less power is needed to create a pore because the free electron distribution amplitude needs to reach its given threshold over a smaller area. The following analysis on spot size and numerical aperture is first completed for Gaussian beams, which is related to the central maximum of a Bessel beam in Section 4.5 for a final determination of spot size.

To begin this analysis, the beam waist at the focus of a lens is given as

$$w_f = \frac{\lambda f}{\pi \omega_{lens}}, \quad (50)$$

where f is the focal length of the lens, λ is the wavelength of incident light and ω_{lens} is the beam waist at the input of the lens. ω_{lens} is set to $D/4$, where D is the aperture of the lens, which is small enough relative to the aperture to prevent truncation of the Gaussian beam or excessive spherical aberrations [43]. Since $D = 2 \times NA \times f$, Equation 50 can be rewritten as

$$w_f \approx \frac{2\lambda}{\pi NA}. \quad (51)$$

This equation shows how the spot size is approximately inversely proportional to numerical aperture and proportional to wavelength. Hence, a higher numerical aperture leads to a smaller focused spot size of the irradiance distribution and free-electron distribution. However, since the objective lens is shared between all the systems in this report, the maximum numerical aperture of this platform is limited by the chemical imaging system, which requires that a water-dipping objective lens is used because using a high-NA oil-immersion lens would interfere with the CARS imaging process as described in Section 6.4. Hence, a numerical aperture of 1.1 was chosen which is the highest NA available while using a water-dipping objective lens. In the following section, the relation between the irradiance spot size and free-electron distribution spot size is examined.

4.4.4 Spot size-Pulse width and Wavelength

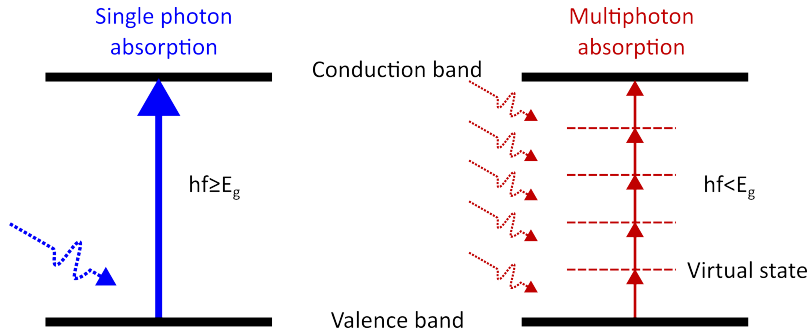


Figure 32: A diagram comparing multiphoton absorption to single-photon absorption. With a number of 5 photons being absorbed, a wavelength of 800nm can be used instead of 177.5nm, leading to less photodamage.

To describe the optical breakdown in cells to produce a free-electron distribution, the effect of irradiation in water is used because the analysis carries over very well to cells. To describe the optical breakdown in water, we use the method used by Vogel et al. [38] and proposed by Sacchi [44], where water is treated as an amorphous semiconductor and the excitation energy is regarded as the energy required for a transition from the molecular 1b1 orbital (the valence band) into an excitation band (the conduction band). This has a band gap energy of 6.5eV [38]. In multiphoton absorption, multiple photons of lower

energies can be used to overcome this band gap energy. This is only achieved using a femtosecond laser. The number of photons needed for excitation is given as m . The excitation of an electron for $m = 1$ for a continuous wave laser and $m = 5$ for a femtosecond laser is depicted in Figure 32.

Then, using the low -intensity approximation of the Keldysh theory (which neglects the effect of tunneling on photoionisation) the free-electron distribution at the end of a femtosecond laser pulse $\varrho_{max}(r, z)$, is given as

$$\varrho_{max}(r, z) = A \times I(r, z)^m, \quad (52)$$

where $I(r, z)$ is the laser intensity distribution and m is the number of photons required for multiphoton ionisation. A is a proportionality constant which will vary slightly depending on I_{max} [38], but can be taken as a constant for this analysis.

Now the size of the free-electron distribution for a specific numerical aperture and wavelength can be plotted, which is shown in Figure 33. This depicts the Gaussian spot created by three different lasers all with a Numerical Aperture of 1.1. The dashed-dotted blue line has a wavelength of 800nm and a value of $m = 1$, which corresponds to a pulse width of CW to nanosecond/picosecond. The red solid line has a wavelength of 355nm and a value of $m = 1$ with a linear absorption mechanism again. Finally, the black dotted line represents the parameters used for this system, with a wavelength of 800nm with a femtosecond pulse width of 100fs , where $m = 5$. Since the blue and black lines both have a wavelength of 800nm , they have identical laser intensity distributions. However, due to the linear absorption of the blue line with parameters $\lambda = 800\text{nm}, m = 1$ its free-electron distribution remains the same size as the irradiance distribution. However, the black line with $\lambda = 800\text{nm}, m = 5$ now overlaps with the red line with parameters $\lambda = 355\text{nm}, m = 1$, because its width has been shortened due to the non-linear absorption mechanism. It can be seen here that the multiphoton absorption mechanism approximately decreases the size of the free-electron distribution by a factor of 2. Hence, using a femtosecond laser enables the system to have a very small spot size while using near-infrared wavelengths which minimise photodamage to cells. This results in a final spot size $0.564\mu\text{m}$ defined in Section 4.5.3.

4.4.5 Optimisation of irradiation time and pulse energy for pore size, injection efficiency and cell viability

As previously mentioned, the optimum parameters to maximise cell viability, transfection efficiency and repeatability are not well known. The key parameters that can be varied are the laser spot size, repetition rate, pulse energy and exposure time. The spot size is typically 500-600nm in radius across most studies,

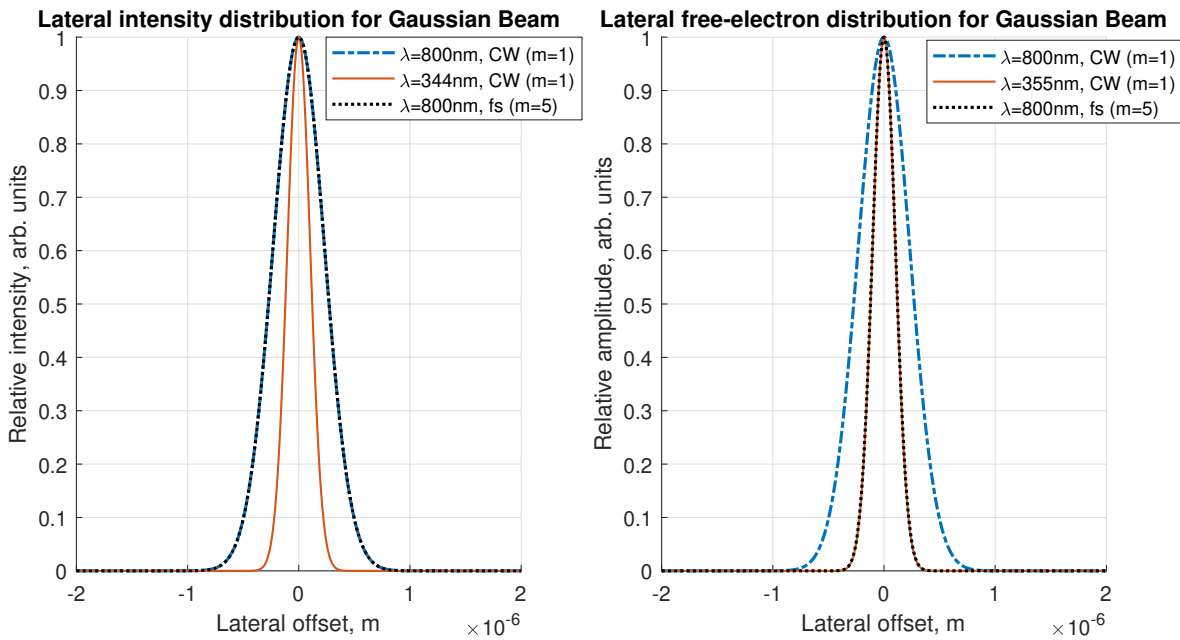


Figure 33

where in Section 4.5.3 the laser spot size is specified as $0.564\mu\text{m}$. The repetition rate has also previously been chosen to be 80MHz. Hence, the remaining parameters to vary are the exposure time and pulse energy (equivalent to manipulating average power with a fixed repetition rate).

Values of cell transfection efficiency are used for comparison of parameters because the processes are very similar to this method of optical injection while having more reference papers. In general cell transfection efficiency increases with irradiation time and pulse energy, while cell viability decreases [42], hence a balance in parameter choice is needed. Cell viability also tends to decrease above a certain pore size [45]. However, the minimum particle radius in this system is limited by the ability to complete ray-optics analysis in Section 2 and Section 3 to get an accurate measure of the forces in the optical trap. This dictates a minimum particles diameter of $2\mu\text{m}$.

With this particle size restriction, a pore size of $3\mu\text{m}$ which would correspond to an exposure power of 75mW and exposure time of 100ms is chosen. This should be sufficiently large to ensure successful injection of the drug particles, while maximising cell viability [45]. However, this is outside of the regime of other papers' studies, so a quantitative estimate for cell viability cannot be given. This appears to be on the limit of pore size while maintaining high viability rates [46]. In a future system, using smaller microparticles and pore sizes could lead to higher cell viabilities. For example, Stevenson et al. indicated cells were more likely to appear healthy with a pore size less than $d = 2.2\mu\text{m}$.

4.5 Bessel beam analysis

A Bessel beam was decided to fulfil the design specification in Section 4.2 best, with the main alternative choice being a Gaussian beam. A Bessel beam requires more incident power from the laser which increases its cost, however its main advantage is its "non-diffracting" property which means that a pore can successfully be created over a much longer axial range. The axial range of the Bessel Beam is specified as $30\mu\text{m}$ and designed for in Section 4.5.3. This means that the targeting of the cell membrane is much more robust to variations in optical misalignment and cell height, which is a common issue with Gaussian beams [36], where some procedures even recommend ablating the cell 3 times at different axial heights for maximum transfection efficiency [47], slowing down the speed of the overall system. Another issue with Gaussian beams is that out of focus light may be accidentally targeted within the cell, destroying its internal structure and decreasing the overall cell viability. This is not an issue for Bessel beams due to the extended axial range, leading to an increase in cell viability as well as insertion efficiency.

4.5.1 Bessel Beam Generation-The Ideal Bessel Beam

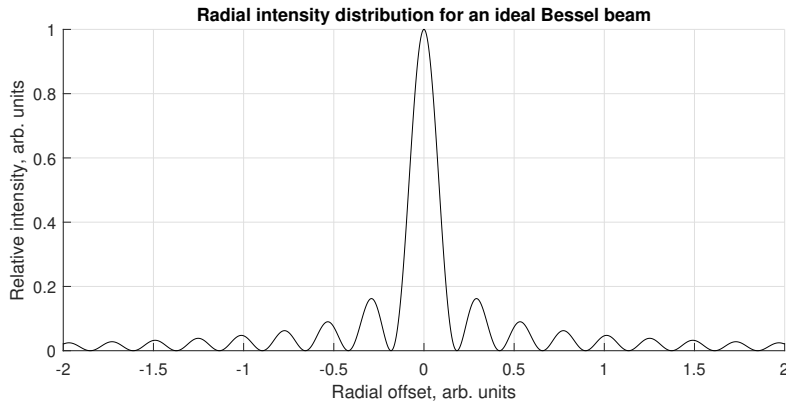


Figure 34: Bessel beam intensity over radial coordinate. The profile includes a large central maximum, followed by several concentric rings of decreasing amplitude. Each ring approximately carries the same amount of energy. For an ideal Bessel beam this profile is invariant for any z -coordinate.

To understand the generation of the beams, it is useful to consider ideal Bessel beams first, which are particular solutions to the time-independent Helmholtz wave equation $\vec{\nabla}^2 - \frac{1}{c^2} \frac{\partial^2}{\partial t^2} u(\vec{r}, t) = 0$ in cylindrical coordinates [39]. For this report, analysis will focus on Bessel functions of the first kind and zeroth order Bessel beams. Figure 35 shows the intensity distribution of a zeroth order Bessel Beam. The ideal zeroth order Bessel Beam has a small thin bright core in its centre that propagates without diffraction and is surrounded by an infinite number of rings which correspond to the oscillations in intensity either side of the peak. Note that since that the intensity approximately decays with $(k_r r)^{-1}$, each ring in the profile

carries approximately the same amount of energy. This electric field amplitude is given in Equation 53 as

$$E(r, \phi, z) = A_0 e^{i(k_z z)} J_0(k_r r). \quad (53)$$

with transverse intensity obtained from Equation 53 is

$$I(r, \phi, z) = |A_0|^2 J_0^2(k_r r), \quad (54)$$

where k_z and k_r correspond to the longitudinal and radial wave vector components respectively, which follow the rule $k = \frac{2\pi}{\lambda} = \sqrt{k_r^2 + k_z^2}$. λ is the wavelength of the light forming the bessel beam, r, ϕ, z are the radial, azimuthal and longitudinal components of the cylindrical coordinates and A_0 is a constant.

This class of equations propagate along z without any diffraction i.e. the intensity distribution is independent of axial coordinate z , however they do have a transverse spatial confinement, which increases as k_r increases. Furthermore, ideal Bessel beams have an infinite extent and since the electrical field amplitude in Equation 53 is not square integrable, creating one would require a beam with infinite energy as well as infinite aperture. This is clearly not possible.

4.5.2 Practical Bessel Beam Generation

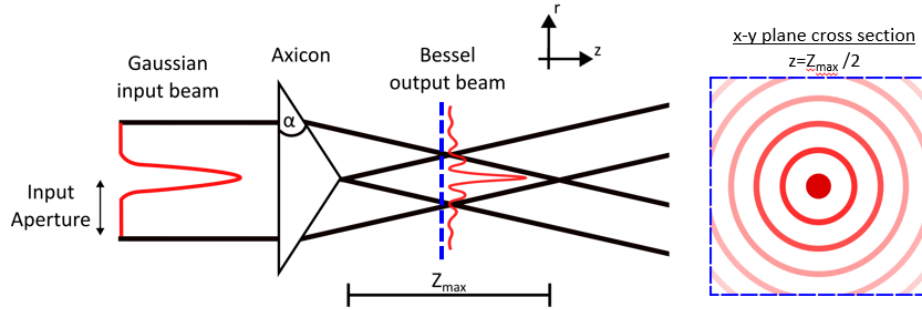


Figure 35: A diagram depicting Bessel beam generation with an axicon. The radial intensity profile is approximately constant over a certain range z_{max} .

To generate these beams practically, we can first look at the Fourier transform of a Bessel beam propagating along the z axis given in Equation 53. In k -space, it is an infinitely high ring in the spatial frequency domain peaked at $K = k_r$, where the phase varies from zero to $2\pi l$ around the peak [48]. This is often described as the Bessel Beam being considered as a superposition of a infinite number of plane waves whose wavevectors are distributed on a cone or a shifted ring centered on the z axis [49].

To recreate this characteristic of the Bessel Beam, any method must apply spatially a linear phase with

rotational symmetry. In this system, this is achieved with an axicon which is a conically shaped optical element which imparts phase shift $\psi(r, \theta) = k_{ax}r$ to an incident field where $k_{ax} = k(n - 1)\gamma$. Where n is the refractive index of the axicon material and γ is the internal angle of the axicon. By choosing $k_{ax} = k_r$ for a specific Bessel beam, the axicon imposes a ring of transverse wave vectors on the incident beam, and these plane waves come together past the axicon to produce a bessel beam [48].

The field past the axicon may be calculated using the Fresnel integral. This integral can be approximated using the method of a stationary phase, which gives an analytical expression for the field intensity $I_0(r, z)$ for a zeroth-order LG input mode with a beam waist of ω_1 [48]:

$$I(r, z) = 2\pi(k_r\omega_1)\left(\frac{P_0}{\pi\omega_0^2/2}\right)\left(\frac{z}{z_{max}}\right)\exp(-2z^2/z_{max}^2)J_0^2(k_r r). \quad (55)$$

This has a central beam width of

$$W_B \approx \frac{2.4048}{k_r} = \frac{2.4048\lambda}{2\pi} \frac{1}{(n - 1)\gamma}, \quad (56)$$

which corresponds to the radial distance to the first zero of the function. It also has a longitudinal extent of

$$z_{max} = \frac{k\omega_1}{k_r} = \omega_1 \frac{1}{(n - 1)\gamma}. \quad (57)$$

Taking the derivative of Equation 55 we find the peak intensity is at $z_{peak} = \frac{z_{max}}{2}$. For a Gaussian beam of equal size with beam waist w_0 , the transverse spreading is given by the Rayleigh range $z_R = k\omega_0^2/2$. Comparing this to z_{peak} it is evident that Bessel Beams have a more tightly focused field, with the longitudinal extent being a linear function of beam waist size instead of a squared function. The other point to mention comparing Bessel and Gaussian beams, is that for Bessel beams the radial width depends only on laser wavelength λ and axicon angle γ , while longitudinal extent depends on incident spot size ω_0 as well as λ and γ . Hence, the radial and longitudinal extents can be varied independently, while for a Gaussian beam the beam waist and longitudinal extent given by the Rayleigh length both depend on w_0 (adjusting wavelength to adjust Rayleigh length can only be done within a certain range, and wavelengths are restricted when working with biological material in this context[48]).

4.5.3 Analysis of axicon parameters

After the decision to implement a Bessel beam, the parameters for the axicon must be decided. For a Gaussian beam, we have already specified the laser spot size and power at the sample. To decide

parameters for the Bessel beam these two variables will be matched and then adjusted based on the propagation length desired.

To match the laser spot size, we use Equation 57 to give the width of the beam, which should contain all the power in the central maximum as it is the first zero of the function. For a focused Gaussian beam the width used is $W_G = w_f \sqrt{3/2}$, where the beam waist at the focus of the lens w_f is obtained from Equation 50. Hence, a value of $0.564\mu m$ is calculated with an NA of 1.1. This corresponds to the point where the intensity reaches $1/e^3$ of its original value, and contains 99.7% of the total energy in the pulse-this is analogous to 3 standard deviations in a normal distribution.

Additionally, the beam expansion of lenses 4 and 5 by a factor of Y has an effect on the central maximum width and propagation length as follows, where W'_B and z'_{max} are the respective distances after going through the beam expansion lenses:

$$W'_B = W_B/Y \quad (58)$$

$$z'_{max} = z_{max}/Y^2 \quad (59)$$

To achieve a beam width of $0.564\mu m$, the beam expansion Y is given a value of 8. This would result in an ideal axicon angle of 7.73 degrees using Equations 58 and 56, however to be able to use a premade axicon this is rounded to 8 degrees. The radial intensity distribution for these parameters and a power input of 1W is given for the Bessel and Gaussian beams. It can be seen that the intensity distribution for the Bessel beam is much lower, because the power is spread out between the different rings. Hence, the next step is to match the power distribution.

The power in each central maximum up to a width of W is calculated as

$$P_c = \int_0^W I(r, z_{max}/2) 2\pi r dr. \quad (60)$$

For an laser of power 1W, the power in the central maximum for the Gaussian and Bessel beams are 0.997W and 0.147W respectively. Hence, the power in the Bessel Beam must be increased by a factor of $1/0.147$ to match the powers. This can be seen in the second plot of Figure 36, with the corresponding free-electron distribution in the third plot. Note that the distribution value for outer rings in the Bessel beam is very low due to the multiphoton absorption mechanism, meaning only the central maximum has a high enough intensity to damage the cell membrane.

Finally, the propagation length z_{max} will be selected. With an beam waist of $\omega_1 = 0.25\text{mm}$ at the axicon the propagation length is $56\mu\text{m}$ using Equations 57 and 59, which gives a large range over which a pore may successfully be created. However, only approximately $30\mu\text{m}$ of this length the Bessel Beam has a free-electron distribution amplitude sufficient for photoporation. The axial intensity distributions between the Gaussian and Bessel Beam are compared in Figure 37, and it is evident that the Bessel Beam has a much larger axial extent.

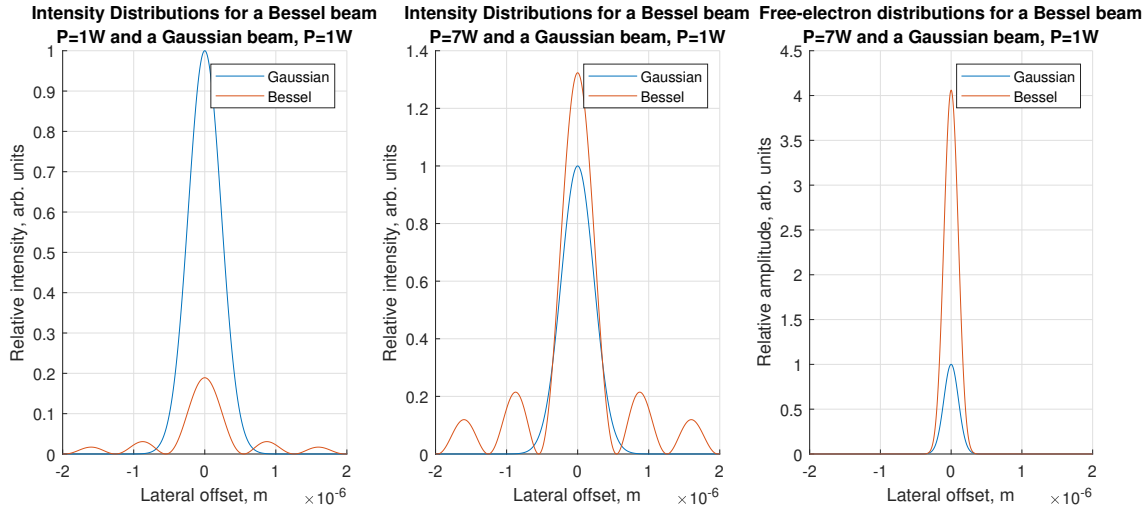


Figure 36: Radial light Intensity and free-electron distributions for different Bessel and Gaussian beams

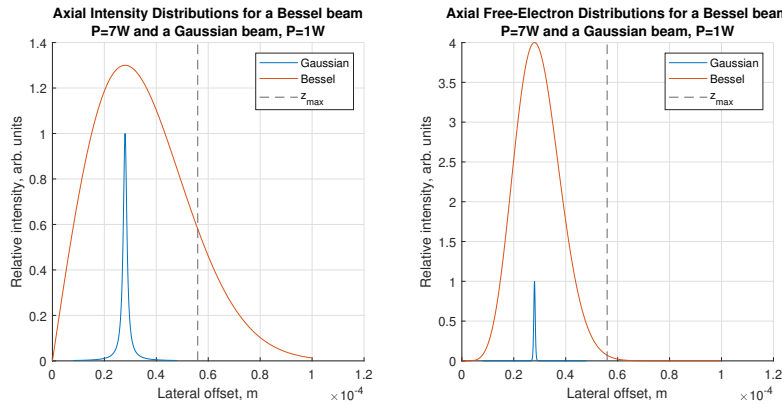


Figure 37: Axial intensity distribution and free-electron distribution for a Gaussian Beam and the Bessel beam used in this system

4.6 Safety Considerations

For the system to be successfully implemented, it must be safe for use. Hence, a number of safety measures are put in place. The largest risk when using lasers is eye damage. In particular, the near infrared light is invisible to the human eye and damage can occur very suddenly without visible risk to an untrained person. Common errors include accidents during alignment of beams and misuse of protective

eye wear [50]. Excessive exposure to near infrared light can also lead to retinal damage, and in severe cases blindness, as well as skin burns at high laser powers [50][51].

The British Standards (BS EN 60825-1) includes 8 classes of laser[51][52]. The laser in this platform would be classed as Class 4 (this applied to any laser above a power limit of 500mW [51]). This applies whenever the system is being set up by a technician, e.g. to calibrate power and optical alignment. However, the platform is enclosed so that during normal operation by a researcher, it is not possible to access the higher exposures directly, hence in this case the laser can be classed as Class 1.

The University of Cambridge's safety precautions for lasers [50] may be taken as a guideline for this system. It is recommended that the laser is only used within a laser-controlled area with appropriate warning signs and that interlocks are used so that the laser automatically shuts off whenever any access panel is opened. Furthermore, during setup and calibration the laser should only be used by trained operators who are aware of the risks of laser operation. Whenever this system is implemented, a risk assessment should carried out for the environment it is used in. Other laser-related hazards to include in this risk assessment are electrical hazards, chemical hazards and potential fume and fire hazards.

4.7 Summary

Overall a capable photoporation system has been design that contains several key features. First of all it has the ability to create $3\mu m$ pores in the cell membrane which was shown to be large enough to insert the $2\mu m$ microparticles in Section 2.2. It does this with an irradiation spot size of diameter $< 1\mu m$, which can be used to target arbitrary cell features. Furthermore, the ability to vary the irradiation time and power at the sample with a mechanical shutter and half wave plate/polarising beam splitter for power control was included, to be able to adjust parameters based on the cell used and to adjust the pore size. Due to the bessel beam configuration created by an axicon photoporation is also possible over an axial range of approximately $30\mu m$. While this system has been designed for photoporation to insert microparticles optically trapped by the optical tweezer system specified in Sections 2 and 3, it can also be applied to standard cell transfection by ablating cells in a concentrated solution of substance such as plasmids.

5 Widefield Imaging System - Alexander Peake

This particular system will be used to produce widefield images of our entire sample, capturing multiple cells, and the particles the Optical Tweezers will manipulate into them, in a single image. Widefield imaging more generally refers to a set of microscopy techniques which have a wide enough FOV (field of view) to view an entire sample, all of which is under illumination, as described in [53]. From these images we will computationally extract important data which both the Holographic Optical Tweezers and Laser Ablation systems rely on: we need to be able to perform image segmentation, accurately telling us the locations of the $2\mu\text{m}$ polystyrene particles at a rate which will allow good performance of the optical tweezers controller, and for the ablation system: we will need to detect the regions in the sample stage which are occupied by the $20\mu\text{m}$ to $30\mu\text{m}$ cells, the tops of which will be ablated.

5.0.1 Design objectives of the system

Our system's objective is to provide an automated method for conducting single cell surgery. All systems including widefield imaging will need to be able to operate with minimal user input. We will therefore need to be able to detect cell and particle locations, as well as a detailed picture of the regions which are occupied by cells in a completely software-implemented way. This will mean utilising relevant image processing algorithms which must be provided with detailed, high quality images from the microscopy system. As previously mentioned in Section 1: a high degree of parallelism is another important general objective, meaning the widefield system will need to be able to image and perform the various segmentation algorithms on multiple cells and particles concurrently.

Design Specifications:

1. **Parallelisation:** We require a wide enough FOV at the camera sensor to view a useful number of cells so that a high degree of parallelisation is realisable. Since our cells will be arranged such that each is separately confined to a region in a petri dish $50\mu\text{m} \times 50\mu\text{m}$ across (see Section 1) and we aim to be able to view a region containing 9 cells for tweezing at any one point, we will need an FOV which will accommodate this at the plane of the camera. A FOV of **at least $170\mu\text{m} \times 170\mu\text{m}$ available at the camera (the total FOV of the lens will be much greater but we will only view a portion of this on the camera)** is therefore the specification targeted as this will generously allow more than nine entire wells, packed into a 3×3 grid to be viewed without any clipping.
2. **Resolution:** We need to produce images of our sample which have high enough resolution to

view the polystyrene particles, which at $2\mu m$ in diameter are the smallest objects we will need to resolve, and to accurately segment the cells from the image. The resolution of this system is diffraction limited and is determined by the wavelength of light used, and the Numerical Apertures of our system's main objective and condenser lenses (as previously mentioned we are using an NA = 1.1 water dipping objective).

3. **Magnification:** the total system magnification should map the entire FOV to the dimensions of the image sensor. The image sensor chosen has sensor dimensions of $6.77 \times 5.66mm$. This area will need to be mapped to the region we aim to view on the sample stage. The magnification thus required for the widefield system **is approximately $33\times$.**
4. **Maximised Cell Viability:** Most importantly for the microscope, we will need to use a technique which minimises harm to the cells which our system is designed to analyse. This makes techniques which do not use harmful staining or fluorescense preferable. This presents a challenge, as without staining, live cells are highly transparent under visible light illumination.
5. **System Imaging Rate:** The system serves as an input for the optical tweezer controller therefore needs to be able to output data at a high enough rate as to not limit the control performance. A rate of **150Hz** is targeted, meaning all image processing must be capable of running faster than this rate.
6. **Cost:** We will need to accomplish the objectives specified above using techniques and components which cost as little as possible, such that the cost of the entire system will be minimised.

There are a number of widely used Widefield microscopy techniques which were considered in light of these requirements. A summary of the findings is shown in Table 5. From this selection **Phase Contrast Microscopy (PCM) was the technique chosen.** Neither PCM nor Differential Interference Contrast (DIC) require staining and although DIC's ability to produce artefact-free images was attractive; it is an inherently expensive technique, and it will be possible to greatly mitigate the artefacts produced in PCM whilst still achieving high quality images.

5.1 Phase-Contrast Microscopy

The imaging technique chosen is phase contrast microscopy (PCM). Transmission microscopes have difficulty in providing sufficient contrast when viewing live cells, which are transparent to visible light. PCM is a technique which will provide the additional contrast required to images of cells in our stage, as

Table 5: Summary of some of the most commonly used widefield microscopy techniques. This comparison was useful in assessing which approach was best suited for our system. PCM emerged as the most appropriate solution due to its ability to produce high contrast images without the need for harmful marking of our cell specimens. The fluorescence and brightfield techniques were immediately considered not possible, due to their violation of the design criteria.

Technique	Advantages	Disadvantages
Brightfield Microscopy: One of the simplest microscopy techniques. Resolvable details appear dark against a bright background.	Relatively few components are required. It is a very simple, cheap and well established technique	Relies on the absorption of light by the sample, meaning low contrast for transparent specimens, staining is usually required when imaging cells.
PCM (Phase Contrast Microscopy): one of the most popular widefield imaging techniques, phase shifts created in the light diffracted by phase objects are translated into intensity differences. This results in greater contrast when imaging specimens which absorb very little light.	Provides high contrast images of biological specimens without the need for staining, relatively few components are needed to achieve phase contrast imaging.	Images may contain undesirable artifacts such as halos and shade-off, which as discussed later can negatively affect the performance of image segmentation algorithms.
DIC (Differential Interference Contrast): Polarised light is used as the illumination source. The principle is very similar to that of phase contrast microscopy. Additional prisms and polarizers are used to achieve this in such a way that does not produce the same artefacts as PCM.	High contrast images are produced, without the need for staining. The images are free from the artefacts often found in phase contrast microscopy.	This method incurs a high cost due to the extra components required.
Widefield Fluorescence: Specimens are stained with photo-fluorescent chemicals known as fluorophores. The fluorophores are then excited by a laser to emit light.	High contrast and high resolution. Not diffraction limited.	The fluorescent compounds are highly toxic to cells.

demonstrated in Figure 38, without needing harmful staining or fluorescence. A technique developed in the 1930s by physicist Frits Zernike, PCM exploits the creation of an interference pattern between direct and scattered light using specialised optics, as described in [54].

Using this technique, phase differences in light passing through the specimen $\Delta\phi$ can be converted into intensity differences. The derivation below is roughly inspired by Hecht, [56], demonstrating the

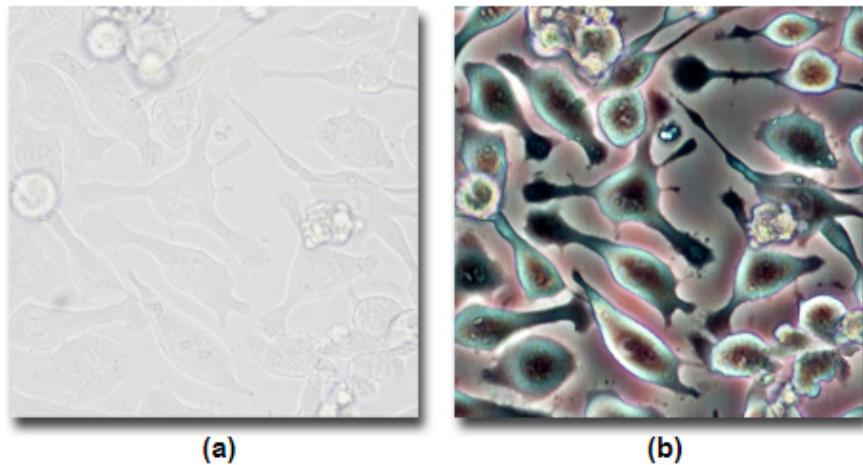


Figure 38: Figure taken from [55]. A bright field image of some living cells are shown in a) The corresponding phase contrast image is shown in b). The phase contrast image is in much greater contrast, thanks to its intensity relationship given by Equation 69.

mathematical principle behind this technique. To start with the light is expressed as a simple planar wave, where (E) represents the electric field component of the light, (ω_0) represents the angular frequency, (t) time, (z) is the position of the wave and (k) the wave number:

$$E(z, t) = A e^{j(\omega_0 t - kz)}. \quad (61)$$

As light passes through different objects within the stage, it will experience differences in optical path length according to the thickness of the disturbance (t). Path difference (OPD) is also a function of the difference in refractive index between the medium (water in our case, $n_{medium} = 1.33$) and the specimen. Cells, due to being largely composed of cytosol, typically have refractive indices of between 1.36 and 1.39 [57]. Path difference can easily be computed as:

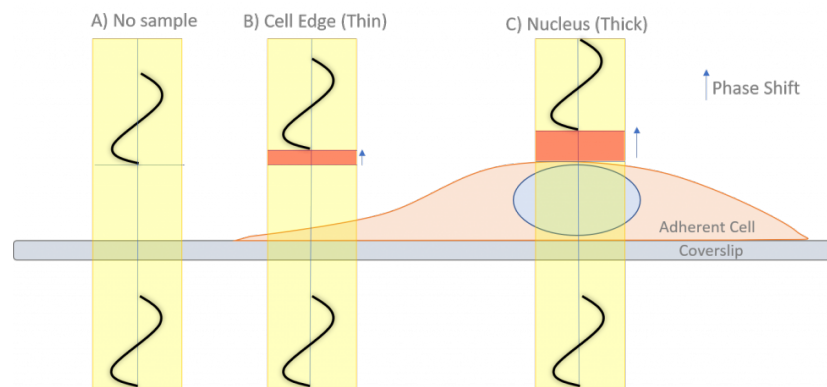


Figure 39: Diagram showing how difference in path taken affects the phase of light exiting the sample stage. From [58].

$$OPD = t(n_{specimen} - n_{medium}). \quad (62)$$

These differences in path length will result in exiting light having differing relative phases, ($\Delta\phi$) depending on the path taken (as shown in Figure 39):

$$\Delta\phi = OPD \times \frac{2\pi}{\lambda}. \quad (63)$$

The deviated light wave will be phase shifted relative to the incident wave:

$$E(z, t) = Ae^{j(\omega_0 t - kz - \Delta\phi)}. \quad (64)$$

Assuming that $\Delta\phi$ is small [56], and applying a Taylor expansion to Equation 64, allows the perturbed light wave to be re-expressed as:

$$E(z, t) = Ae^{j(\omega_0 t - kz)}(1 - j\Delta\phi). \quad (65)$$

Since we are purely concerned with intensity, the modulus will remove any complex components, and we can solely consider the real component of the phase-shifted wave:

$$\mathcal{R}[E(z, t)] = A [\cos(\omega_0 t - kz) + \Delta\phi \sin(\omega_0 t - kz)]. \quad (66)$$

We can see that the wave consists of two components [56], the cosine term which is unaffected by the phase shift and represents the **Direct and Un-deviated** component. There is also the sine component, pre-multiplied by $\Delta\phi$ representing the **Diffracted and Deviated** component of light exiting the specimen. Phase contrast microscopy techniques then introduce a $\frac{\pi}{2}$ phase shift to the un-deviated light, using the light paths shown in Figure 40 (there are two main types of phase contrast microscopy, positive and negative. Positive PCM induces a $(+\frac{\pi}{2})$ phase shift, negative PCM a $(-\frac{\pi}{2})$ difference):

$$\mathcal{R}[E(z, t)] = A \left[\cos(\omega_0 t - kz - \frac{\pi}{2}) + \Delta\phi \sin(\omega_0 t - kz) \right], \quad (67)$$

$$\mathcal{R}[E(z, t)] = A [1 + \Delta\phi] \sin(\omega_0 t - kz). \quad (68)$$

This is done with the use of a phase plate the structure of which is shown in Figure 41. It consists of a transparent disk in which there is a ring of phase-shifting material. The different light paths are shown in

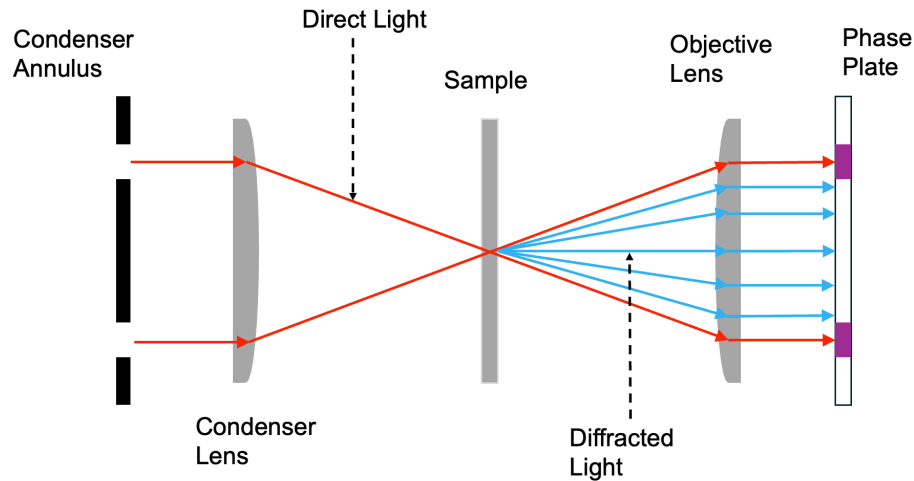


Figure 40: Light paths in a phase contrast microscope. Light from the condenser annulus forms a cone which is focused onto the sample using a condensing lens. When the light reaches the sample, a component is diffracted and phase shifted by $\Delta\phi$ (represented in blue) and passes through the regions of the plate adjacent to the phase ring. the direct light will be passed through the phase ring and path-shifted by $\frac{\lambda}{4}$, providing correct alignment of the condenser annulus and phase plate.

Figure 40. The intensity of the resulting wave becomes dependent on the phase shift created within the specimens as shown in Equation 69, rather than just the intensity of transmitted light ($I \propto A^2$). This is the result which achieves the drastic increase in contrast:

$$I \propto A^2 |1 + \Delta\phi|^2 . \quad (69)$$

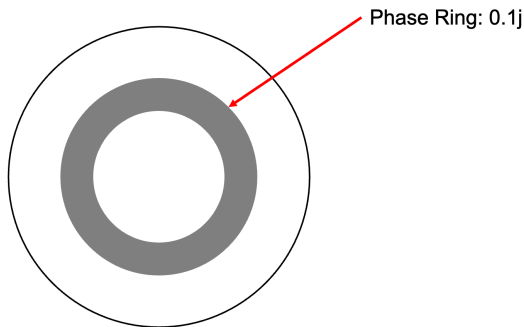


Figure 41: Physical construction of a phase plate. The plate consists mostly of a transparent disk. The phase ring (shown in grey) is a layer of phase-retarding material, which introduces the $\frac{\pi}{2}$ shift to the un-deviated component of the light. In most PCM systems, the phase plate is housed within the objective lens assembly itself, for our system this would be impractical as discussed later.

An unfortunate artefact encountered in PCM images are regions of high intensity around the edges of

specimens, known as Halos. This artefact is caused by the small leakage of diffracted light which is able to travel through the phase ring material. If allowed, this can cause significant reduction in image quality and contrast, and is known to cause issues for automated image segmentation, as was discussed in [59]. The techniques which will be used to mitigate this effect will be discussed further on in the report in Section 5.1.5.

5.1.1 Optical Layout and Price Breakdown

The optical layout devised for the Widefield imaging system is shown below in Figure 42. To summarise the operation of this setup: the sample is illuminated with green 550nm LED illumination. The light is passed through a circular annulus and condenser to produce a cone of light at the sample stage. The objective lens is then used to resolve the information from the light passing through the sample. The phase plate comes next, which produces the required phase shifting to the direct light component as described in Equation 67. The resulting intermediate interference pattern is then focused onto the plane of the CMOS imaging sensor by a transform lens. The cost breakdown of all components in this microscope is shown in Table 6.

Table 6: Estimated cost breakdown for the phase contrast microscope, using pricing from distributor websites. Where exact prices could not be found for specific components, the price of similar components was used. Not included are components shared with other subsystems.*Included together as part of a kit manufactured by Nikon

Component	Quantity	Price per item (£)	Total price (£)
Apodized Phase Plate	1	426	426
Condenser Annulus	1	426	426
CMOS (IDS Imaging GV-79F0WP-M-GL)	1	2010.25	2010.25
FBH550-40 550nm optical band-pass filter	1	131.74	131.74
LED Illuminator	1	500	500
Tube Lens	1	450	450
Widefield Imaging System Price: £3943.99			

5.1.2 Illumination

The illumination wavelength chosen for the microscope is 550nm, provided by an optical band-pass filter combined with broadband LED illumination. This green light exists at the middle of the visible spectrum, and is the wavelength around which most commercial phase plates are designed to work. At this wavelength, animal cells are typically transparent and will behave as phase objects. It is possible to user a broader band of illumination e.g. from white LEDs, but using monochromatic illumination will ensure that there are minimal chromatic aberrations introduced to the images. Chromatic aberrations are distortions caused by the differing ability of a given lens to focus different wavelengths to a point. Contrast is also

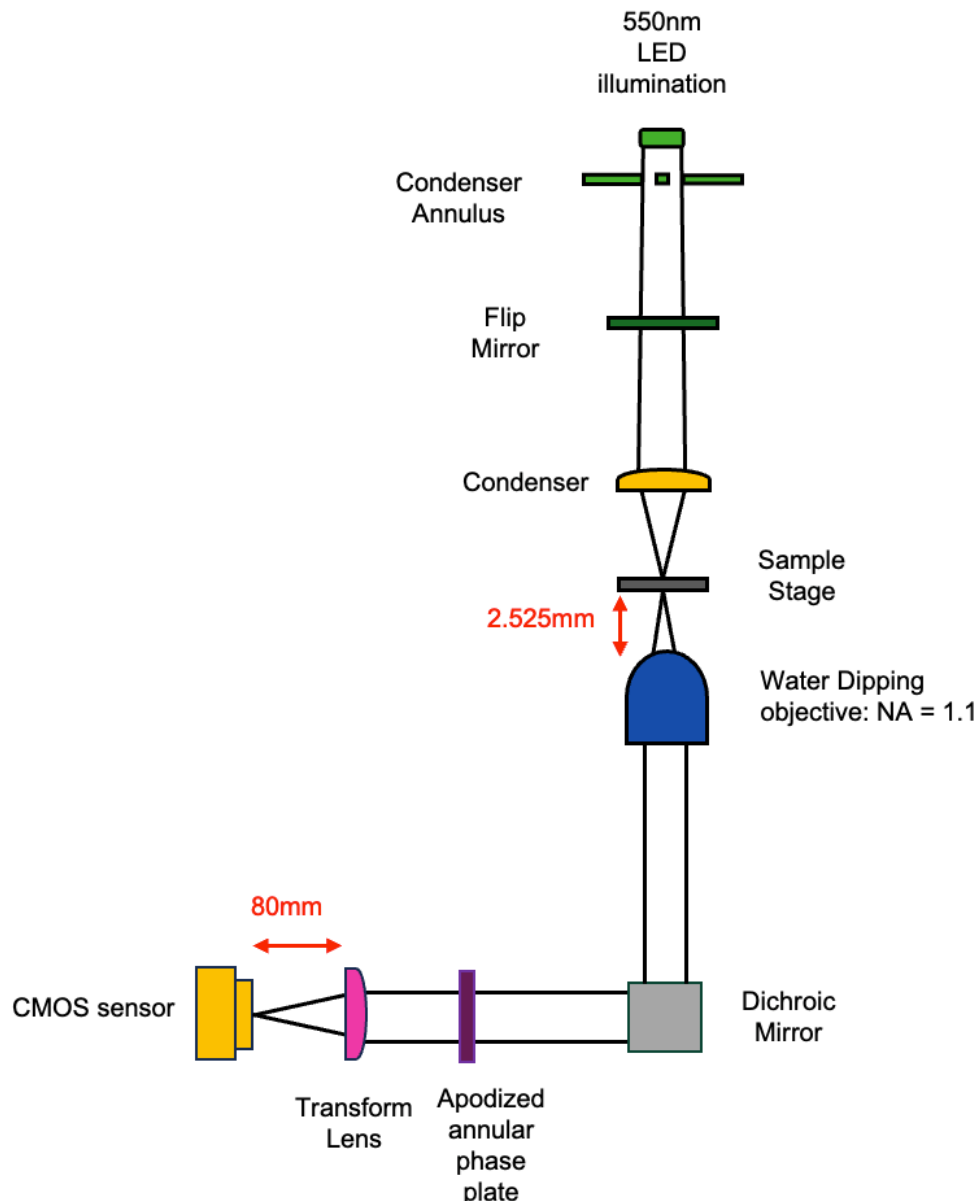


Figure 42: Exploded optical layout for the Widefield imaging system. The system shares the objective lens with all the other optical systems. The microscope produces high-contrast phase-contrast images which are captured by the CMOS sensor at the bottom. The phase plate is designed to produce the $\pi/2$ phase shifts at the 550nm wavelength used in the LED illumination. There is a dichroic mirror which will allow use of the phase plate without negatively impacting the optics of the other systems.

maximised when using solely 550nm illumination as other wavelengths will not completely destructively interfere at the phase plate. This light is shone through a condenser annulus which is an opaque disk with a transparent ring optically conjugated with the phase ring of the phase plate. This creates a cone of illuminating light of which the direct component will travel through the phase ring, as shown in Figure

40, provided correct alignment.

The flip mirror is necessary due to the overlap between the 550nm illumination and the range of wavelengths swept over by the CARS system. The two subsystems will never be used at the same time, thus the flip mirror will be able to change its state depending on the current stage of the process.

5.1.3 Phase Plate

As described earlier, the phase-plate's role is to shift the phase of the un-deviated light from the sample by one-quarter wavelength. Normally this component is packaged directly within the objective lens housing. This is impractical for our design, as all systems within this architecture share the same objective lens, and aberrations introduced by the presence of the phase plate would decrease performance of all other optics. This effect is analysed in detail in Section 5.1.4.

5.1.4 Fourier Optics Simulation

The effect of the phase plate was simulated in MATLAB using some principles of Fourier Optics, which describes the behaviour of light within optical systems using Fourier transformations. As described previously in Section 2.3.1: the interaction of incident light on a convergent lens produces a 2D spatial Fourier transform [60]. The result, represents the resultant intensity distribution.

A circular aperture, represented in MATLAB as a square matrix of zeros, with a filled circle of transmittance 1 at the centre: represents the back focal plane of the objective lens, over which the Fourier Transform can be taken, without the presence of the phase plate. This represents light travelling through the objective from the sample.

Computing a Fast-Fourier-Transform over this matrix, the resulting intensity distribution follows the distribution of an Airy Disk as shown in Figure 43. This is the best possible focusing distribution a perfect lens can theoretically create of a circular aperture and represents the diffraction limit of an optical system [61]. The deviation of energy from the central maximum is the minimum physically possible. The phase plate is represented with a similar circle of transmittance 1, but with a ring of phase shifting material, represented by a ring of values $e^{j\pi/2}$. Conducting the same test reveals a significantly altered intensity distribution, shown in Figure 44.

Figure 45 shows both point-spread-functions overlayed to illustrate the artefacts introduced by the phase plate. Both curves are normalised to the same energy content, but we can see that the height of the

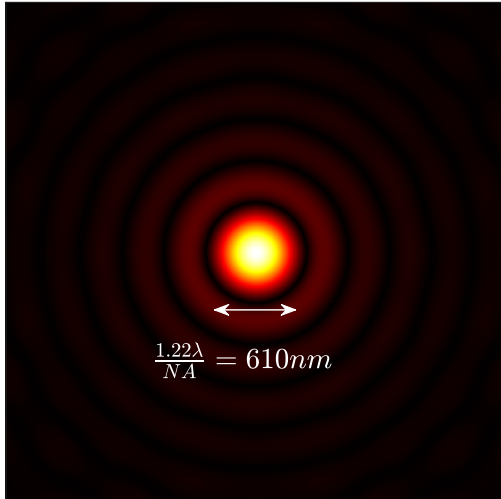


Figure 43: The airy disk produced by an ideal lens. Computed using a MATLAB simulation, computing an FFT over a circular aperture. The central peak is equal in diameter to twice the resolution distance of the lens.

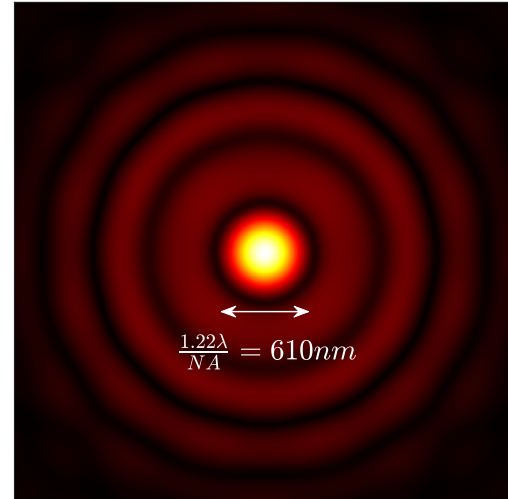


Figure 44: Intensity distribution for the objective lens with the phase plate. Side lobes have much more energy, as more light is diffracted. The power of the light after the lens is more spread out and the mean intensity becomes lower at the point of focus. The width of the central peak remains the same in both cases. This case represents a diminishment of focusing ability.

central peak is lower for the phase plate curve. The side-lobes have more energy content in as well, showing that the phase plate has caused power to be more 'spread out' in space which would physically manifest as a slight decrease in the effective focusing power of the objective. This is an example of an optical aberration that would be introduced from the inclusion of phase contrast optics.

This effect would likely not be hugely detrimental to the performance of the widefield system due to the relative large size of the polystyrene beads however could be disastrous for the optical tweezing system, which relies on having a very high Numerical Aperture focusing lens for stable trapping as mentioned previously in Section 2.2, and may not be able to tolerate this effect. To avoid this problem, **the decision was made to place the phase plate out of the path of all other systems using a dichroic mirror.**

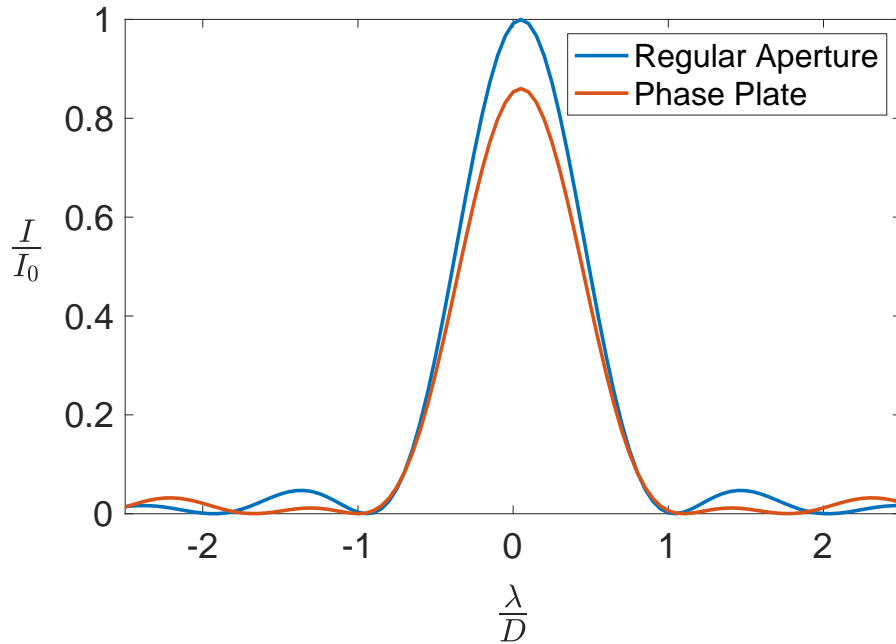


Figure 45: MATLAB simulation of the PSF of a phase plate compared with the PSF of a lens. Plotted is the normalised intensity against distance from the centre of the aperture, in terms of wavelength over aperture diameter (D). The Fourier transforming property of lenses was used to compute this, taking a circular aperture in either case and using a 2D Fast Fourier Transform. Energy from the lens is more concentrated at the peak of the distribution, with the side-lobes containing a small proportion of the total intensity field. The difference in central peak energy is more apparent here than in Figures 43 and 44.

5.1.5 Effect of Apodization For Removing Artefacts

As mentioned previously PCM suffers from artefacts created by a portion of light diffracted by specimens [62]. These artefacts are mostly caused by light diffracted by only shallow angles causing a portion to pass through the phase ring, along with the direct light. These Halo effects create regions of spurious higher intensity around the edges of specimens which can distort their edges as well as create a loss of contrast throughout the images [63]. These effects have widely proved detrimental to image segmentation algorithms, such as the ones mentioned later in Section 5.3 and it was concluded that as a result mitigation of this effect was necessary.

Halo effects can be addressed through the use of specialised optics [62]. Apodized phase contrast optics are designed to overcome this issue by suppressing diffracted light near to the phase ring. It achieves this through use of two concentric rings of neutral density film coating the plate adjacent to the phase ring, as

can be seen in Figure 46. This selective attenuation is evident in the graph in Figure 47 which shows the results of simulation, taking a Fourier transform of the apodized phase plate 46 compared with a regular plate 41. The intensity of the first side lobe is shown to be particularly diminished by adding this ring. This will particularly affect the Halo objects observed around larger objects, which will generally diffract light to a smaller angle.

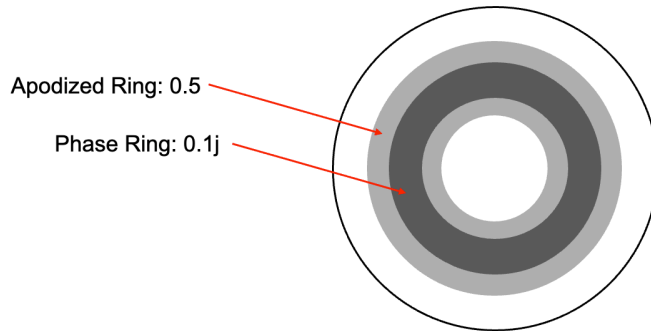


Figure 46: The construction of the apodized variant of the phase plate. The phase ring itself is identical to the non-apodized case, but instead there is the ring of neutral density material of transmittance = 0.5. This input field was fed into the MATLAB simulation for Figure 47.

Through this effect, apodized optics are able to achieve much higher-quality images, closer to the results theorised in the ideal case (described in Section 5.1). These images will allow for much more accurate image segmentation. For this reason **we will use an apodized Phase Plate in the microscope**.

5.1.6 Objective, Condenser, and Transform Lenses

As previously mentioned, the widefield imaging system shares the objective lens with all other optical subsystems. This informs the resolution we should be able to theoretically achieve given the wavelength of illumination chosen. The resolution of a diffraction-limited microscope (d) such as this one can be found through Abbe's Relationship 70 with $\lambda = 550\text{nm}$ being the illumination wavelength and $NA_{objective}$ and $NA_{condenser}$ are the numerical apertures of the objective and condenser lenses respectively:

$$d = \frac{1.22\lambda}{NA_{objective} + NA_{condenser}}. \quad (70)$$

The condenser lens is required to focus the illuminating light onto the sample in a cone shape, and to ensure that the entire sample is correctly illuminated. Its numerical aperture must be the same or greater than that of the objective to ensure that illumination will fill the entire NA range of the objective, otherwise the effective resolution of the widefield system will be limited. **The condenser we will be using will**

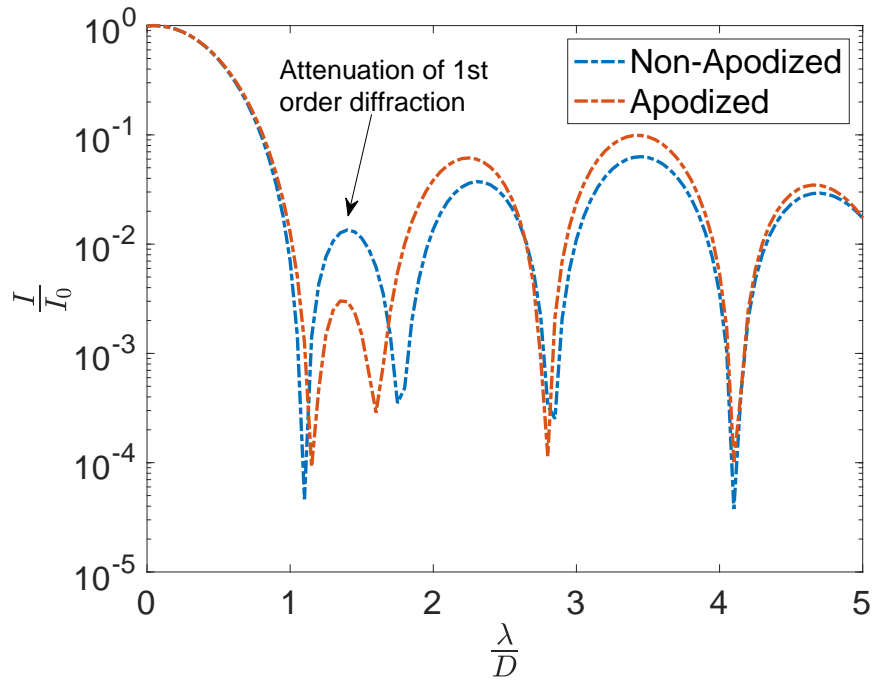


Figure 47: MATLAB plot of normalized intensity distribution against radial displacement from the centre of the phase plate on semi-log axes. This is expressed in terms of the aperture radius (D). The first side lobe represents the first order diffracted light which is more severely attenuated in the case of the apodized plate. This selective attenuation is a result of neutral density film which is placed either side of the phase ring, and results in greatly diminished halo artefacts. The other, higher order lobes representing light diffracted across a much higher angular range are minimally affected.

therefore be a NA = 1.1 water dipping lens. This gives us an upper limit on the available **resolution of 305 nm**, not taking into account the reduction in effective numerical aperture from the existence of the phase plate. Assuming that the reduction in effective NA is minimal however (reasonable given the similarity in intensity distributions and similar peak size this) would be an adequate level of resolution given the smallest objects we need to resolve in our sample are the microparticles sizing about **ten times as large in diameter**.

The objective is an infinity corrected lens, meaning to actually form an image from the intermediate interference pattern created by the phase contrast microscope, a transform lens is also required. This will also determine the total magnification of the system. As previously discussed a magnification close to **33 \times** is targeted. This can be used to find the desired focal lengths from the expression given in Equation 71, where $f_{transform}$ and $f_{objective}$ are the focal lengths of the transform lens and objective respectively

[64],

$$M_{total} = \frac{f_{transform}}{f_{objective}}. \quad (71)$$

The MRL07920 objective lens has a focal length of 2.525mm. This means a transform lens with focal length of **84.1mm** would theoretically be required. This is not a standard focal length however, which would necessitate an expensive custom optic. To keep costs down, instead using a standard **80mm** optic as shown in Figure 48, would provide a magnification of **32 ×**. This would instead provide a FOV of **180 μ m × 180 μ m** which would still be adequate for viewing the desired **nine cells**.

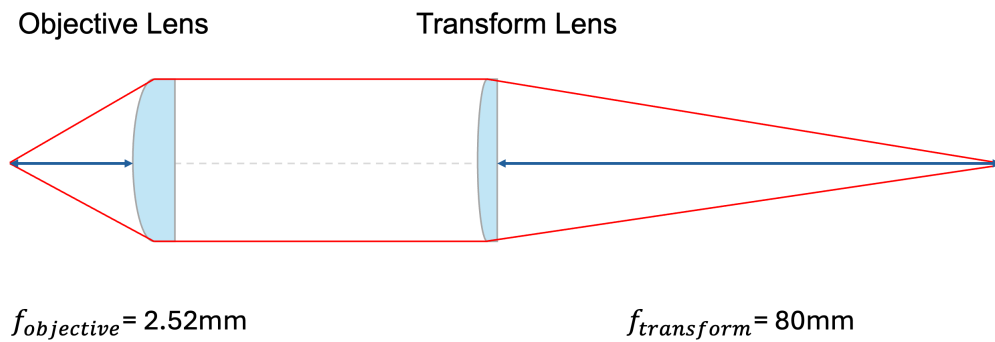


Figure 48: Focal lengths of the objective, and the corresponding focal length of the transform lens in order to achieve the desired magnification at the image plane. Phase plate will go in the middle, in the infinity corrected region

5.2 Camera sensor

A camera is needed for capturing the state of our sample stage. This sensor will collect monochrome images (we are imaging solely with 550nm illumination) over which image segmentation will be performed. There are two main imaging sensor technologies to choose from. Complementary-Metal-Oxide-Semiconductor (CMOS) devices and Charge-Coupled-Devices (CCD). CCD sensors are a legacy technology where each pixel consists of a photodiode, which will produce electrical signals dependent on the intensity of incident light. The intensity reading on each chip is stored capacitively and then during the readout stage each pixel is read sequentially and fed through a shared amplifier. As a result of this process, CCDs deliver images with high Signal to Noise Ratios (SNR) and high dynamic ranges (greater contrasts).

CMOS sensors are derived from technology used to make memory cells, meaning they can be manufactured in standard silicon fabrication plants. They are digital sensors, in which each pixel contains its

own individual amplifier, amplifying photodiode voltages. These readings are then read digitally [65].

There were technical specifications which had to be fulfilled regardless of the technology used to ensure accurate image formulation:

1. **Pixel Pitch (μm):** The size of the pixels in the sensor is an important factor ensuring that the imaging system will be able to resolve enough detail. The smallest detail we aim to resolve, multiplied by the system magnification of $32\times$ will be the dimension that detail is projected to at the plane of the camera. The pixels will need to be smaller than half of this dimension in order to avoid aliasing our signal, in accordance with the Nyquist sampling theorem. The smallest feature size resolvable is 305nm. To avoid aliasing the maximum pixel pitch must be $4.88\mu\text{m}$. This is a very reasonable target value, with many imaging sensors on the market having pixel pitches in the range $3\mu\text{m}$ to $5\mu\text{m}$.
2. **Sensor Size:** The sensor size, measured as the diagonal dimension of the rectangular array should map to the FOV with the level of magnification our system achieves. This dimension affects the total magnification required and thus the dimensions of pixel we would require.

Both CMOS sensors and CCD sensors tend to have their own benefits and disadvantages relevant to the application. To help decide what sensor technology would be best for this system, the following factors were included in a multicriteria analysis table. Relevant weightings, summing to 100 % were assigned.

1. **Cost:** CCD sensors typically are more expensive than CMOS sensors, owing to their slower and more complicated manufacturing process. A decision was taken as a group for cost minimisation to be a key focus, as this system contains many components which together would have the possibility of making this system prohibitively expensive. A high weighting was therefore necessary.
Weighting = 30 %.
2. **Quantum Efficiency at 550nm:** Quantum efficiency (QE) describes how effective a sensor is at converting the energy of incident photons to electrical energy. The higher this quantity is, the greater sensitivity achieved resulting in higher-contrast images.

CCD sensors tend to have higher quantum efficiencies than CMOS sensors as is shown in Tables 7 and 8. A high Quantum efficiency is very important for producing high quality images, as this determines how sensitive the sensor will be. A relatively high weight is used. **Weighting = 20 %**

Table 7: Quantum Efficiency of typical commercial CMOS sensors at 550nm.

CMOS sensor Model	QE at 550nm (%)
CS505MU1	72
Sony Pregius Gen4	71
Retiga E9	90
Teledyne Moment	73

Table 8: Quantum Efficiency of typical commercial CMOS sensors at 550nm. The Quantum efficiency values are higher than for their CMOS counterparts.

CCD sensor Model	QE at 550nm (%)
iKon-L 936	90
iXon 888	95
Teledyne PIXIS: 1024	95

3. **Noise Immunity:** All image sensors will suffer from random noise. There are a number of physical processes which cause random noise in images. Read Noise exists across the entirety of the image area and is an artefact of the electronic processes needed to convert incident photons to electrical signals. It can be modelled as a Gaussian process [66]. Thermal noise also manifests as Gaussian noise, which is the model applied to images for testing of image processing algorithms in Section 5.3. CMOS sensors in particular can suffer from 'Salt and Pepper' noise, due to the slight differences between the amplifiers on each pixel.

Typically CCD sensors are more robust to noise than CMOS sensors, which amass more total noise due to the large number of separate amplifier circuits. For this reason CMOS has been assigned a score of **5**, and CCDs a high score of: **9**. It is important that we have high enough signal to noise ratios for accurate image processing, however the effects of thermal noise can be greatly mitigated through effective cooling. A median weighting was used **Weighting = 10 %**

4. **Readout Rate:** The readout rate is incredibly important for our application. The particle detection algorithm serves as a direct input to the control of the optical tweezers, which will need to be provided with the centre coordinates of all particles being tweezed at a rate of **150Hz**. Slow input rate will cause poor controller performance. The speed of the widefield imaging process is also determined by the speed of the algorithms running each cycle (shown in Table 10) but the image sensor should not be the limiting factor.

The camera system serves as a direct input to the tweezers control system and thus needs to be sufficiently fast, **150fps is the target readout rate**. CMOS sensors tend to have higher readout

Image Sensor	Signal to Noise Ratio (10%)	Quantum Efficiency at 550nm (%) (20%)	Imaging Rate (40%)	Cost (30%)	Total
CCD	9	10	2	2	4.3
CMOS	5	7	9	9	8.2

Table 9: Multi-criteria Analysis to determine which camera sensor technology, out of CCD and CMOS would be the most appropriate. This takes into account attributes deemed most applicable to the system design. The final column shows the output sums in red. CMOS sensors emerged as the best choice.

rates than CCD devices meaning a greater choice will exist towards this specification value. For this reason, CMOS sensors are awarded a score of **9** and CCDs **2**. The importance of readout rate justified a high weighting. **Weighting = 40 %**.

From conducting the multicriteria analysis, **CMOS sensor technology emerged as the best choice**. A sensor which conformed to the minimum specifications was chosen below.

Exact Sensor Choice: IDS Imaging GV-79F0WP-M-GL 1/1.8" Monochrome PoE Camera

- Sensor Size: $6.77mm \times 5.66mm$
- Read Rate: 220fps (max)
- Pixel Pitch: $2.74 \mu m$
- Price: £2,010.25

5.2.1 Alignment and Correct Positioning

Correct alignment of the optical components is essential for the effective operation of subsystems within our design. In particular for the Widefield imaging: correct alignment of the condenser annulus diameter with the phase ring diameter is essential for achieving maximum contrast. In addition, vertical positioning of the stage relative to the aperture of the objective is vital for correct focusing of widefield system. At incorrect distances the stage and all specimens within will appear blurry and obscured. For most optical setups alignment is conducted manually by the user which is time consuming especially for apparatus with a large number of optical components such as this one. It however would be possible to automate this procedure, by measuring the degree of 'focus' the sample stage is in from the images measured by the CMOS camera.

The Laplacian based focus measurement, is a mathematical technique often used to compute the blurriness of an input image. It consists of finding the 2^{nd} order derivative of an intensity image, and computing the variance of this resulting matrix. The higher this variance, the more in-focus this image is as described

in [67]. This measurement, could be maximised using a gradient descent approach coupled with actuation of the stage, to create an auto-focus system which could be run at startup of the system. In addition this approach would also ensure the femtosecond laser ablation system is also in focus. The distance in focal point between the wavelengths used in the laser ablation system and the widefield imaging system (550nm) can be empirically found to be small and precisely quantifiable [45]. This would mean achieving the correct height for laser ablation would be trivial once the stage is in focus.

5.3 Image Processing

The other major component of the Widefield imaging system are the image processing algorithms which will extract the particle locations within the sample for tweezing and the exact locations of the cells. To properly analyse techniques to these ends, a MATLAB script was created to form images which would be accurate simulations of the real images we would obtain with a real PCM microscope. This simulation models the relative contrasts of the phase objects as shown in Figure 50, the diffraction limit of this system, and the effects of additive noise. Particles and cells are added onto an image matrix and thickness and refractive indexes are taken as inputs to calculate their relative intensities within the image. The exact implementations of the image processing algorithms used were provided by MATLAB.

The resolution of our system is calculated, and the image is convolved with a Gaussian Kernel of relevant size to form an approximation of the PSF. The choice of a gaussian kernel is not directly related to any physical optical process, instead the central peak of the PSF as seen in Figure 45 can be approximated by a gaussian with standard deviation equal to the 'true' PSF's full width at half maximum (FWHM). The similarity can be seen in Figure 49. This approximation was taken from a study in which various approximations to the airy disk were assessed [68].

5.3.1 Cell Segmentation

The cells are immobile throughout the process of transfection, adhered to the bottom of our sample stage. The laser ablation step is carried out on the top of the membrane, to allow the optical tweezers to move the particles into the cell as previously mentioned in Section 4. To know precisely where to ablate, it is the responsibility of the widefield imaging system to find and output these regions. This step will need to be computed once for every 3×3 grid of cells.

The cells, thanks to our phase contrast microscope should be represented in our images as a region containing a substantial intensity increase. Canny edge detection, an algorithm discussed more in detail later in Section 5.3.5, is a popular method for extracting edge information from images and could be

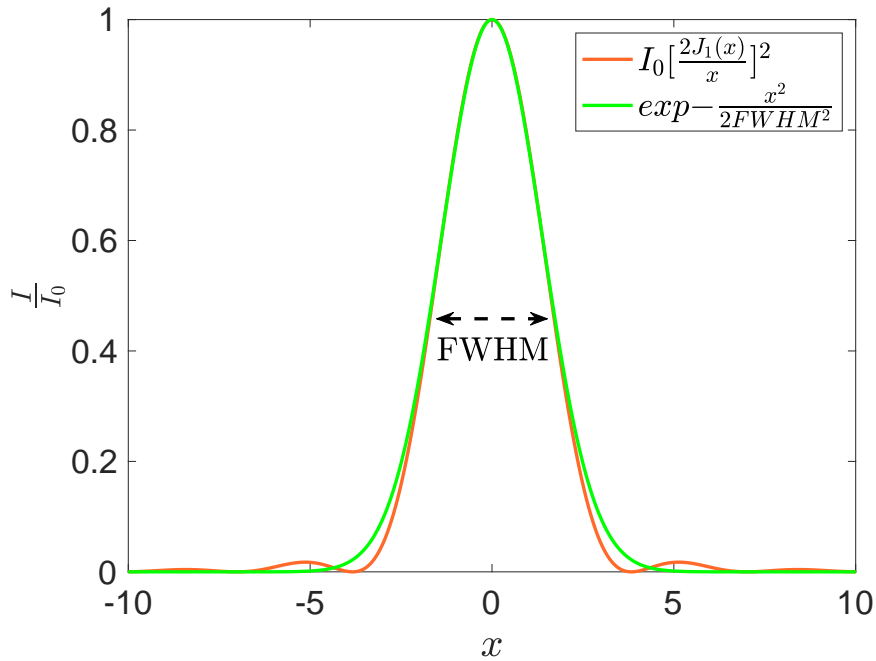


Figure 49: MATLAB illustration of the approximation made of the likely ideal widefield PSF. Gaussian approximation of the PSF of the widefield imaging system. The value of σ in the Gaussian filter approximation can be approximated using the FWHM of the PSF. Approximation [68] makes computational simulation of the diffraction limit simpler. This fact is exploited later in this report to model the effects of astigmatism.

used for segmentation [70]. This was tested as a means for extracting edge information from the sample images. It firstly computes the gradient over the intensity data of the image, and then applies thresholding to output only the strongest edges. Unfortunately it suffers greatly from the presence of noise, in many cases detecting a significant number of false positives.

The Active Contour algorithm is a popular computer vision method for performing image segmentation in medical and biological applications which is far more robust to noise. Active Contours was tested on simulated phase-contrast images, in the presence of a small amount of white Gaussian noise to allow its expected performance to be found.

5.3.2 Active Contours

Active Contours, commonly referred to as "Snakes" is a technique which iteratively fits an initial piecewise contour or "spline" to a particular region in an image [71]. [72]. It has a number of advantages over purely gradient-based methods such as Canny edge detection, which is discussed in Section 5.3.5.

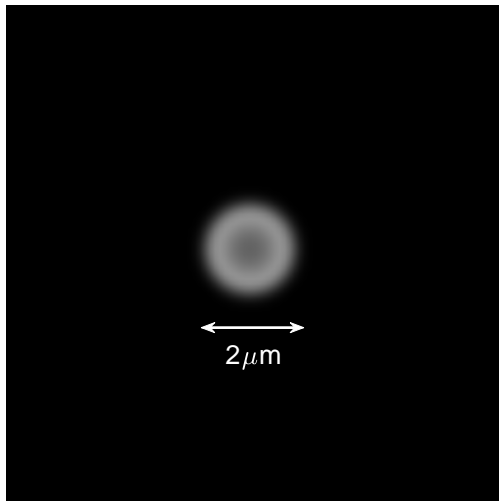


Figure 50: MATLAB simulation of the expected **contrast** we can expect to observe between the polystyrene microparticles and their background using this positive phase contrast imaging system. Regions treated with zero phase shift, such as the background have relative intensity of zero. Note the decrease in intensity towards the centre of the particle: this effect is due to the very large path difference experienced at the thickest point of the object. When the phase shift is large and just exceeds 2π , the effective path difference is very small hence there is a region of lower contrast. This artefact did not prove detrimental to the performance of the image processing algorithms discussed later, as the edge intensity does not suffer this effect. This was constructed using the intensity relationship given in [69], applicable for large phase changes.

Advantages Over Edge detection Algorithms:

- **Closed Outlines:** obtaining a closed region is important for our system as this will properly isolate the top of a cell, defining a region on the stage on which laser ablation can be conducted. Active contours as an algorithm produces such contours, unlike edge detecting algorithms such as Canny, which do not necessarily produce closed outlines. This will allow a binary mask to be fed to the laser ablation system, with regions where ablation can occur are highlighted.
- **Robustness to Noise:** Active-Contour algorithms are much less susceptible to noise, which we can expect to be introduced from the processes described previously. They are less likely to suffer false positive detections.

The algorithm is often referred to as an energy minimisation algorithm and in a classical form [72] is described by a cost function given in Equation 72. The first two terms in the integral represent an **Internal Energy** where α weights the amount the curve is able to stretch tangentially and β affects the tendency of the spline to bend. Tuning these parameters affects how well the contour will match the shape of the cells.

The last term is referred to as **external energy** and describes the gradient of the intensity distribution of the image after it has been smoothed out using a Gaussian kernel to attenuate noise.

$$E(s) = \int_0^1 \alpha \left| \frac{\partial v(s)}{\partial s} \right|^2 + \beta \left| \frac{\partial v(s)}{\partial s} \right| + |\nabla G_\sigma(v) I(v)| ds \quad (72)$$

An initial contour is initialised and an approach such as gradient descent is used to optimise the problem, changing the shape and size of the contour until the cost function in Equation 72 is minimised at which point the algorithm terminates having fitted a spline to the outer shape of the cell. Figures 51 to 55 illustrate the convergence process, with a circular initialised contour in pink converging to the boundaries of the 'cell' as iterations progress. This particular initialisation of the contour is an inefficient approach used purely for the purpose of illustration. Fewer iterations are necessary if the contours are initialised as close as possible to the boundary, as discussed in Section 5.3.3. From the accuracy obtained in testing (shown in Figure 55) it is clear that using active contours would be a reliable way of providing estimates of the cell boundaries even in the presence of noise.

5.3.3 Initialisation of Contours

Theoretically, the quality of the output contours will be unaffected by the way in which the contour is initialised [73], however convergence can be slow if the initial spline is 'drawn' far away from the cell targeted. In many medical applications, the initial contour is often 'drawn' on manually, with the researcher assigning a region of interest (ROI) around the cell they wish to converge a boundary to. This obviously would not be an ideal approach for this system, aiming to provide automation. A different, more automated approach is to initialise the contours around regions of high intensity as is described in: [74], [71]. This was the approach used to initialise the contours in the analysis conducted and produced successful results.

5.3.4 Contrast Sensitivity

The sensitivity of the algorithm was tested, taking sensitivity as the minimum contrast we could expect active contours to work reliably at. The active contours algorithm proved to work reliably for cells exhibiting path differences of at least 1.2 radians. Below this value, the 'cells' would appear with too little relative intensity to the background that the segmentation did not produce accurate edges or otherwise failed to segment the cell to any degree. This minimum phase change will correspond to a specimen thickness of **1.75 μm** . The thickness of cells in a single layered configuration such as ours has experimentally found to be typically around 5 μm [75], meaning we can be confident that using an active contours approach

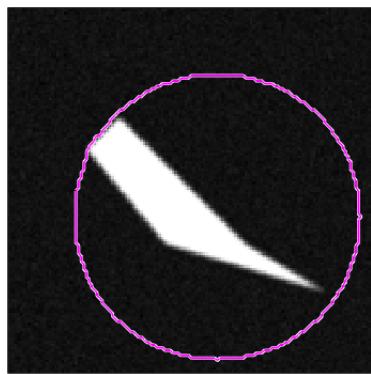


Figure 51: MATLAB simulation of the active contour algorithm after only 1 iteration. This shows the initialised contour, which in this case is a simple circle merely to demonstrate the algorithm. The actual approach to initialisation is discussed in Section 5.3.3.

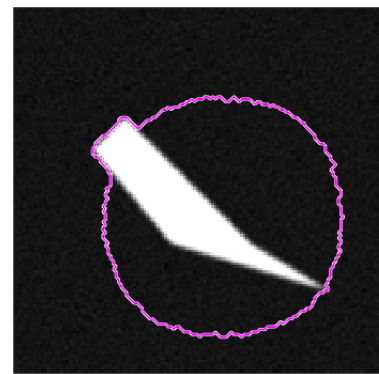


Figure 52: 20 iterations

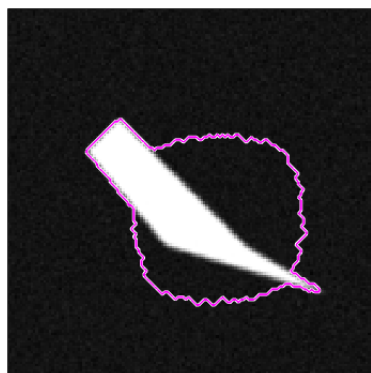


Figure 53: 40 iterations

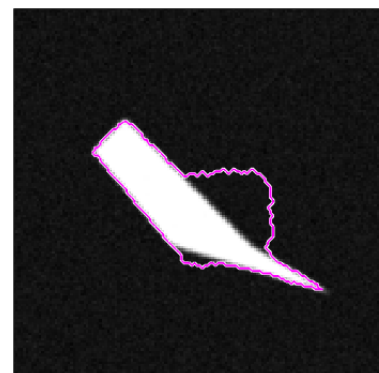


Figure 54: 60 iterations

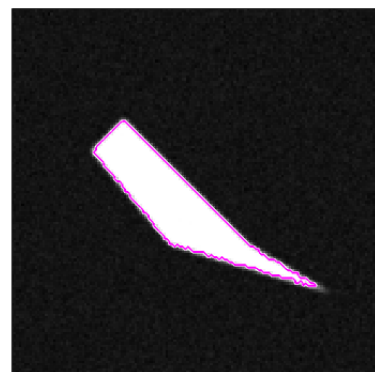


Figure 55: 80 iterations. The contour fits well to the edges of the cell, segmentation is complete.

such as ours would be a reliable approach for locating cells.

5.3.5 Particle Detection

For accurate manipulation, the optical tweezing system constantly requires the current locations of the drug-coated particles within the water immersion of our sample stage. We need to be able to differentiate between what is a particle and what is a cell. Luckily the particles have very distinct characteristics allowing them to be distinguished; they are uniform in diameter and spherical. They will therefore appear as circles within each image. A circle-detection algorithm is therefore used to locate them.

The Circular Hough Transform (CHT) is an algorithm for finding the locations of circular objects within 2D image data, and is an extension of the Hough Transform which is a technique in computer vision used for finding straight lines in images as described in [76], [77]. This step will output the centre coordinates of all circles it finds. All implementations of the CHT involve the following steps:

- 1. Canny Edge Detection:** Firstly, the edges in the image are found. Typical edge detection algorithms, such as Canny edge detection exploit the fact that edges in images are represented by a region of high spatial derivative. Assuming that the input images are grayscaled (as they are in this system): a convenient method of computing an image's 1^{st} order spatial derivative is through convolution with the horizontal (73) and vertical (74) kernels associated with the Sobel Filter:

$$G_x = \begin{bmatrix} -1 & 0 & 1 \\ -2 & 0 & 2 \\ -1 & 0 & 1 \end{bmatrix} * I(x, y) \quad (73)$$

$$G_y = \begin{bmatrix} 1 & 2 & 1 \\ 0 & 0 & 0 \\ -1 & -2 & -1 \end{bmatrix} * I(x, y) \quad (74)$$

The resulting image gradient magnitude is found by fusing the resulting matrices, by finding the element wise root-square-sum: $G(i, j) = \sqrt{G_x(i, j)^2 + G_y(i, j)^2}$. Once the gradient image is found, the Canny edge detection then applies a maximum threshold to only include the sharpest edges.

- 2. Accumulator Matrix Voting:** Every circle, parameterised by each center point within the image is checked to see how many edge points would intersect with it. The more edge points which intersect - the more 'votes' accumulated for that circle. As shown in Figure 56, the circle intersecting the edge

points on the original will collect the most votes. This voting occurs in a data structure known as the *Accumulator Matrix*, $A(x_{\text{centre}}, y_{\text{centre}})$ which parameterises each circle with its centre coordinates. This step can also feed with the false edges which are detected due to the presence of noise, which

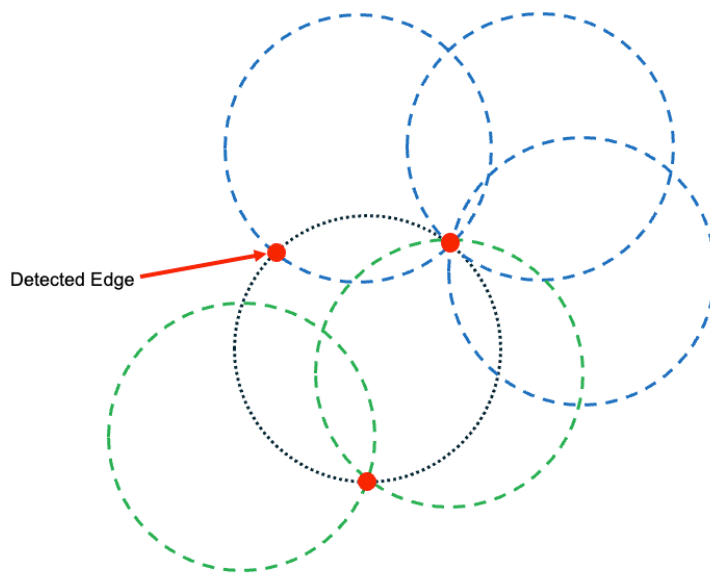


Figure 56: A greatly simplified diagram to show how the CHT works. Each of the red points is an edge point detected by the Canny edge detector. The dashed circles represent a few of the possible circles which could intersect the edges. Each intersection a circle has with an edge point counts as a 'vote'. The circle satisfying the most of the original edge points, with the most votes, will constitute a positive detection.

were problematic in the cell edge detection. This however has not proved as detrimental to the performance of the particle detection algorithm as noisy edges in this step will be negated by the voting process to some extent. The Canny detector also applies a Gaussian filter before performing edge detection in order to attenuate noisy pixels: improving final results.

3. **Circles Found:** Lastly, the possible circles with the most votes - the local maxima within the Accumulator matrix are selected, and their centre coordinates are outputted from the system as detected microparticles.

It was important to test that this algorithm would work sufficiently well given the imperfections found in real microscopy images, namely: the imaging resolution limit and additive noise. This is simulated using MATLAB, with the image generation discussed previously. The results are shown in Figure 57, demonstrating high accuracy in the presence of additive noise.

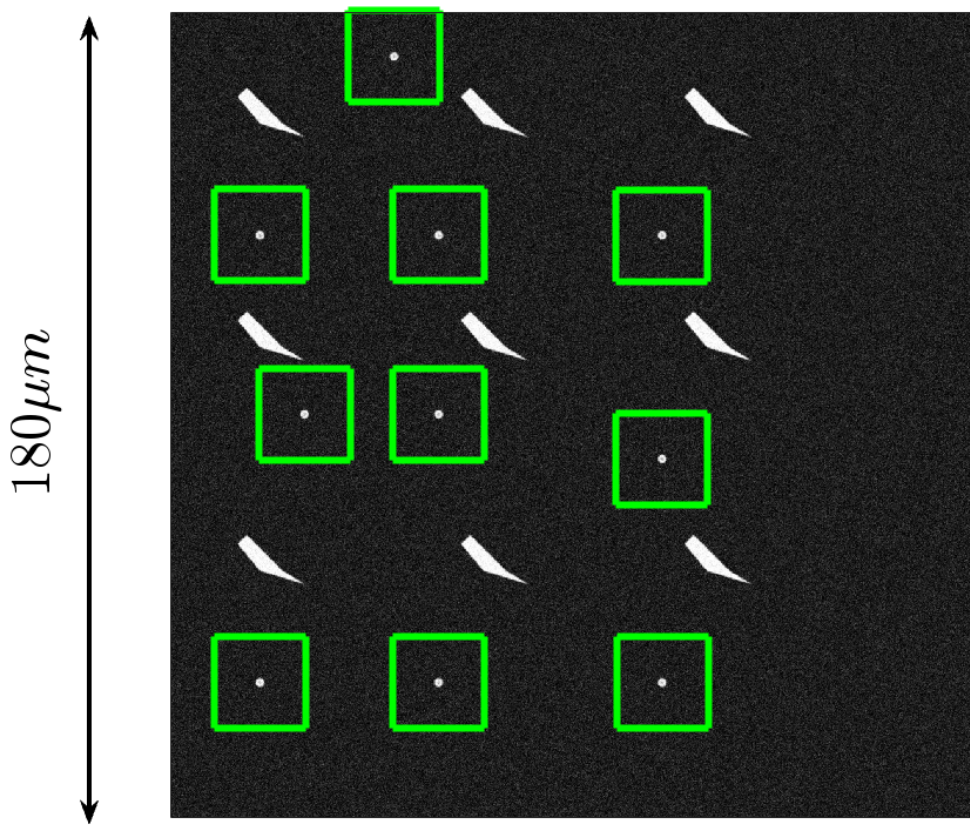


Figure 57: MATLAB simulation to show how the CHT would perform on images we would produce. A FOV of $180\mu m \times 180\mu m$ is used, and the diffraction limit of our system is simulated through convolution with a Gaussian Kernel, where σ is chosen to correspond to the diffraction limit. The green boxes show where the CHT run over the image detects circular objects. In this simulation the CHT is perfectly able to detect all particles within the microscope system's FOV, without falsely detecting the cells. The irregular shapes represent the cells. The green boxes show the centre coordinates of all detected particles, which would be outputted to feed into control of the optical tweezers

5.3.6 Precision

The precision of the particle detection algorithm needs to be precise, to ensure optimal performance of the optical tweezing control. Testing the simulation indicated that error in the measurement of the particle centre was on the order of **10nm**. This is possible despite the much larger resolution limit, as the particle centre itself will not suffer as greatly from the resolution limit as the edges. This shows the accuracy of this technique, being able to locate the centre of each particle to within 0.5% of the actual particle diameter.

5.3.7 Time Taken

Unlike the cell segmentation, the particle detection algorithms will need to run continuously throughout the optical tweezing process and thus the time performance is important. The time taken for the algorithm to run over the generated stage images were tabulated below. These values can be treated as upper limits

on the time that this could take in the final system as the performance of this code could be improved greatly through use of better hardware (this was run on a personal laptop when in reality our system would be controlled by a more powerful machine potentially) or using dedicated GPUs and also through code compilation or re-implementation in a compiled language such as C/C++.

Table 10: MATLAB measured CPU time taken for the CHT to be computed, and for all successful detections on the numbers of particles we would expect to be needed to locate. This also shows the algorithm runtime is broadly invariant for differing numbers of particles. Measured were rates of approximately 15Hz. MATLAB R2023b.

Number of Particles	Time taken (s)
10	0.0753325
15	0.075779
20	0.074274
25	0.076664

The MATLAB provided implementation of CHT algorithm was found to run at a maximum of **15 times per second** across the simulated images. A readout rate of **150fps** is targeted, as this rate offers sufficient performance to the control of the optical tweezers as discussed in Section 3.5.4. This would entail a ten times increase in the speed of this computation which is not unreasonable given the limitations of the computing power used to run the above test as well as the vast scope for optimisation; parallelising the algorithm is a possibility, the images could be subdivided into nine smaller images (one for each cell area in view) and then the CHT could be run on each individual cell concurrently.

5.3.8 Effect of Astigmatism Aberrations On Particle Detection

Real-World objective lenses and indeed all optical components can suffer from manufacturing defects. It is naive to assume that the spherical polystyrene microparticles will suffer completely symmetrical aberrations from the objective lens. Astigmatism causes non-symmetrical distortions of the specimen. Point Spread Functions from real objective lenses can cause a higher degree of 'blurring' in one axis which could cause circular objects to appear elliptical (this can also be caused by incorrect alignment of the components):

$$PSF(x, y) = \frac{1}{\sqrt{2\pi}\sigma_x\sigma_y} e^{\frac{1}{2}\frac{x^2}{\sigma_x^2}} \times e^{\frac{1}{2}\frac{y^2}{\sigma_y^2}}. \quad (75)$$

This had the potential to cause difficulty for the CHT algorithm which searches for circular objects within the image. Analysis was conducted to assess the impact of these aberrations, as whilst alignment problems are fixable, the software will need to be able to be robust to astigmatism introduced purely by the

objective. A high-quality objective will produce negligible astigmatism, more extreme cases were tested for the sake of robustness. The CHT is successful up to extreme astigmatisms which could only corre-

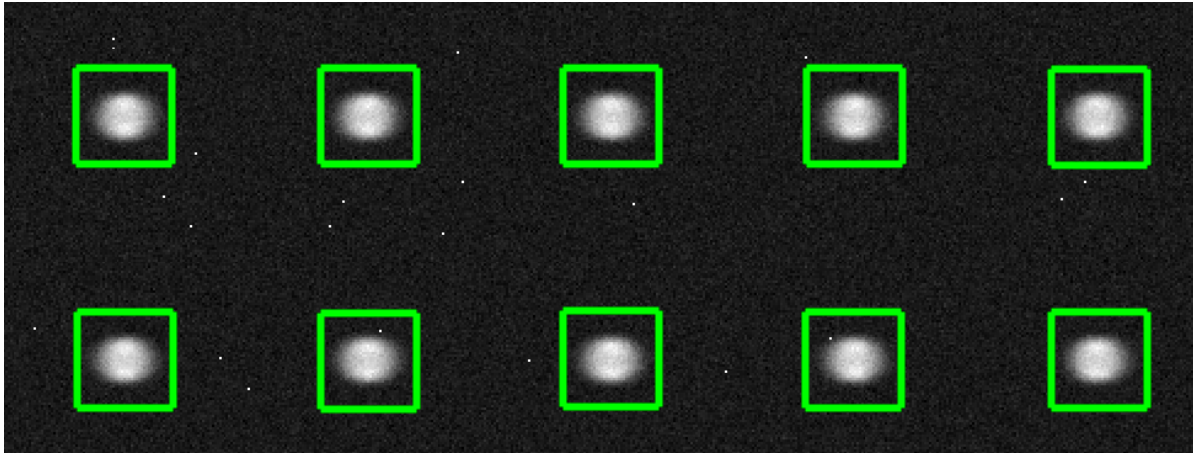


Figure 58: MATLAB simulation on the effects of a very extreme astigmatism, on the performance of the CHT algorithm. This was modelled using a Gaussian kernel of the form in Equation 75. This is a very extreme case, where σ_x is three times the value of σ_y . This corresponds to an effective horizontal resolution of 690nm and vertical resolution of 229nm. The CHT has enough inherent robustness to still able to detect all particles.

spond to an extremely poor objective lens. Figure 58 shows an image capturing a MATLAB simulation where the CHT is successfully able to recognize particles convolved with kernels with a ' σ ' value three times greater than the other axis. The likely small astigmatism we would likely experience would not pose a problem therefore to the performance of the particle detection aspect. This demonstrates the robustness of the CHT for finding circular objects within images.

5.4 Input To the CARS System

The final way the widefield imaging system feeds information to the other systems is to the CARS system. This process as discussed later involves relatively slow scanning of the sample stage which would be inefficient if the entire FOV had to be scanned. Instead, regions of interest (the locations of the cells) are conveniently outputted from the widefield system and can instead be scanned. This optimisation drastically decreases the area that has to be swept assuming only one cell per $50\mu\text{m} \times 50\mu\text{m}$ area is being scanned. This is a major optimisation which will decrease the overall time the entire system process takes.

5.5 Summary

- To summarise, the widefield system consists of a Zernike Phase Contrast Microscope and CMOS imaging sensor. Widefield images of the sample stage are taken, across a $180\mu\text{m} \times 180\mu\text{m}$ field

of view which allows nine entire $50\mu m \times 50\mu m$ sample stage area to be viewed in each of which a single cell will be contained - a key requirement to allow parallelism of the entire process. Imaging will be done at resolution of about 300nm, which is ample for viewing the details of the smallest relevant specimens in the stage - the polystyrene microparticles.

- The widefield system will then run an active contour detection algorithm to find the area occupied by the cell within the phase contrast image. This serves as an initial input to the control of the stage which will move the cell for laser ablation and define a region in which the laser will burn a hole. As an input to the optical tweezers, the Widefield system will output real-time particle locations to high precision of 10nm, which will be found using the circular Hough transform running at a rate of at least 150Hz. Testing of these algorithms showed that both performed accurately on simulations representative of the images which we would expect to produce. Both additionally proved to be robust in the presence of noise.
- The segmented cell regions will be fed as coordinate data into the CARS system, allowing a field of view drastically smaller than the field-of-view to be scanned before and after the transfection has occurred.
- A focus was made on building this system as economically as possible, taken as part of a group decision to mitigate the cost of what is a technologically advanced and inherently expensive system.

6 Chemical imaging system - Xianming Liu

In this platform, chemical imaging system refers to the Coherent Anti-stokes Raman Scattering (CARS) Microscopy system. Unlike conventional wide-field imaging systems, which offer a broad field of view, the CARS system makes a trade-off, opting for obtaining more information of the sample at the cost of a imaging speed. This deliberate choice is made to equip the platform with the capability for chemical discriminant imaging. This approach enables the detailed visualization of chemical composition without the need for traditional labeling techniques, offering a significant advantage in long term observability.

6.1 Introduction to Design Specifications

The primary goal of the chemical imaging system is to confirm the accurate delivery of drug particles into cells. This requires an imaging platform capable of sub-cellular resolution and differentiation among various particles.

6.1.1 Process Overview

1. The initial step involves using wide-field imaging system to identify the general area of interest and detect the presence of drug particles.
2. The chemical imaging system is then deployed to scan the area to identify the cell and drug particle using its chemical discriminate ability.
3. Post drug delivery, the system reassesses the cells to ensure successful drug delivery.
4. Long term follow up observation for the study of drug uptake mechanism.

6.1.2 Design Specifications:

- **Chemical discriminant Imaging:** The system must, at a minimum, be able to differentiate and identify the drug particle from the solution. Ideally, it would also provide chemical imaging of the scan area, detailing both chemical composition and spatial information.
- **Maximize Long-term Observability:** Continuous observation of the cell's response to the drug is crucial. The platform must allows for long-term studies.
- **Maximize Cell Viability:** Ensuring minimal impact on cell health. The imaging system, particularly the excitation laser, should operate in the NIR region to prevent photodamage.
- **Scan Area Compatibility:** The scanning area of the super-resolution system should exceed that of wide-field systems to ensure coverage without mechanical adjustments of the stage.

- **Spatial Resolution:** With drug particles sized at $2\mu\text{m}$, the system's resolution should surpass this. Target resolution of 300 nm to enable detailed sub cellular analysis.
- **Depth of View:** The system should possess adequate depth of View to image cellular interiors, not just surface levels.

6.2 Overview of Microscopy Techniques and Limitations:

Several imaging systems are available that meet the specified design requirements to varying extents. Below is a concise summary of several techniques.

- **Fluorescence Microscopy:** A widely used imaging method in life sciences, fluorescence microscopy utilizes the properties of certain molecules (fluorophores) that emit light upon being excited by a specific wavelength. This technique allows for visualization of specific components within cells through labelling the sample with fluorophores that bind to target molecules.

Limitations:

- **Photobleaching:** Over time, fluorophores lose their ability to fluoresce when exposed repeatedly to the excitation light. This reduces the observation duration.
- **Chemical Selectivity:** The choice of fluorophore is crucial. It must selectively attach to target molecules while not effect the drug uptake mechanism.
- **STED Microscopy:** Stimulated Emission Depletion Microscopy is a super-resolution technique that allows for imaging beyond the diffraction limit by selectively deactivating fluorophores, leaving a pinpoint area of fluorescence. This method significantly narrows the point of emission, allowing for much higher resolution imaging. This technique is able to archive spatial resolutions of 50-60nm.

Limitations:

- **Photobleaching and Phototoxicity:** Similar to fluorescence microscopy, STED faces challenges with photobleaching and phototoxicity. Repeated exposure to intense light can damage the fluorescent dyes and potentially harm the cell.
- **Cost and Complexity:** The system requires the use of an additional laser to selectively deactivate the fluorophores. Thus making the system more complex and costly to build.
- **Spontaneous Raman Scattering Microscopy (SRS):** Utilizes the Raman scattering phenomenon, where light interaction with molecules results in energy shift, thus changing the scattered light's

wavelength. This shift is unique to the molecular composition of the sample, allowing SRS microscopy to create a hyperspectral image that maps the chemical composition.

Limitations:

- **Weak Signal and Long Imaging Time:** The signal produced by Raman scattering is inherently weak, making it challenging to detect low concentration chemicals without resorting to higher excitation powers. This results in an increased imaging time.
- **Coherent Anti-Stokes Raman Scattering Microscopy (CARS):** Developed to overcome the weak signal issue of SRS, CARS uses two lasers at different wavelengths to excite molecules at specific resonances frequency. This non-linear process amplifies the Raman signal, enabling the detection of molecules at lower concentrations and faster imaging.

Limitations:

- **Complexity and Signal-Noise-Ratio:** The system is more complex than SRS, and while it offers enhanced sensitivity, it tends to have lower resolution. Non-resonant background signals can also reduce the signal-to-noise ratio, complicating data analysis.

6.2.1 Multi-Criteria Analysis

Multi criteria analysis is used to determine the Microscopy technique that is most suited to meet our design specification. Four weighted criteria: Cell Viability, Imaging Speed, Spatial Resolution, Complexity to score each technique. The final score is then normalized to out of 100%.

Table 11: Multi-Criteria Analysis of Microscopy Techniques, Total score normalized to 100%

Imaging Technique	Long Term Cell Viability (35%)	Imaging speed (20%)	Spatial Resolution (25%)	Complexity (20%)	Total
Fluorescence	4	8	3	8	53.5
STED	4	5	8	4	52
SRS	10	6	4	7	71
CARS	9	8	6	6	74.5

CARS Microscopy performs best in the multi-criteria analysis, as it provides great Long term cell viability combined with fast imaging speed. As a result, CARS Microscopy is chosen as the method for chemical

imaging task on our platform.

6.3 Working Principle of CARS Microscopy System

Before diving into CARS microscopy, this Section began with a brief overview of Raman Scattering, the Phenomenon underlying CARS microscopy.

6.3.1 Raman Scattering

When an incident light hits the sample the vast majority of the scattered light will be of same energy as the indecent light, however a small proportion will be emitted at a different energy, Figure59 [78]. This scattering happens because the incident photons collide with the molecules, transferring energy in the process. Some of this energy goes into changing the vibrational, rotational, or electronic states of the molecules. This causes the scattered light to have different energy as the incident light, Figure 59. Since Photon Energy is inversely proportional to its wavelength, the wavelength of the scattered light is also shifted. The wavelength difference is known as Raman Shift measured as a wavenumber. Different Raman-Shift provides specific information about the molecule's vibration frequencies, rotation transitions. Which are linked to specific physical properties such as bonds structure, and the dipole moments.

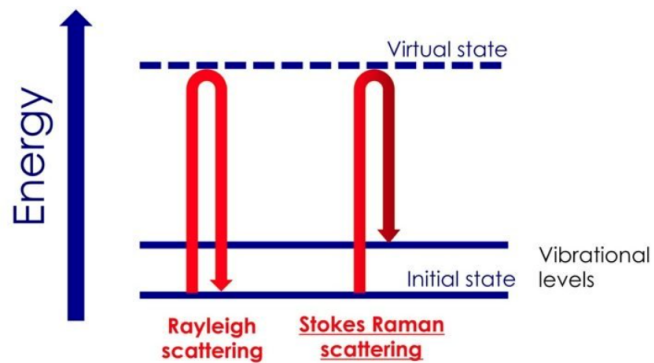


Figure 59: Energy Level Diagram of Raman and Rayleigh Scattering: Raman Scattering has different energy as the incident light. [78]

6.3.2 Traditional Coherent Anti-Stokes Raman Scattering

Coherent Anti-Stokes Raman Scattering (CARS) is a nonlinear optical process that is based on Raman Scattering. It is primarily used for imaging and analyzing molecular structures. Unlike conventional Raman scattering, CARS utilises two different laser beams: the Pump beam and the Stokes beam. These beams are simultaneously incident on the sample, where their frequencies are specifically chosen so the difference matches a vibrational frequency of the molecule being studied. When these beams interact with the molecules, a third photon is generated. This photon has a higher energy (or lower wavelength)

than the pump beam, which is the characteristic signature of CARS, see Figure 60 [[79]]. The process amplifies the Raman signal by producing a coherent emission from the sample, making CARS particularly useful for observing low-concentration samples or fast dynamic processes within living cells [80].

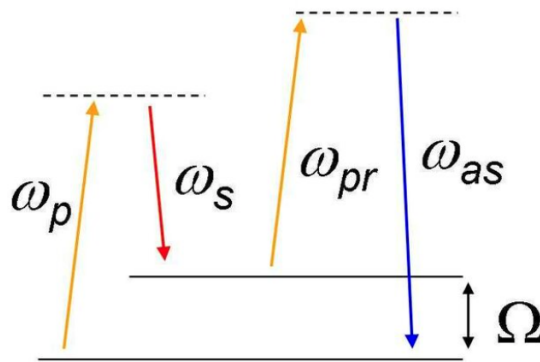


Figure 60: CARS Energy level, the Output ω_{as} has the highest energy compared the incident photons [79]

The advantage of Coherent Anti-Stokes Raman Scattering lies in its ability to provide high-resolution, chemically specific images, and spectra of samples with minimal background noise. The coherence of the signal leads to a strong directional emission, which significantly enhances the signal-to-noise ratio compared to spontaneous Raman scattering. Furthermore, the use of near-infrared wavelengths for the pump and Stokes beams allows for deeper penetration into biological tissues with reduced photodamage, making CARS an invaluable tool for biomedical imaging and research.

6.3.3 Higher Order CARS

Traditional CARS microscopy typically involves four-wave mixing processes, see Figure 60. Higher-order processes like six-wave mixing and eight-wave mixing can also be employed to enhance resolution and sensitivity, this is typically achieved by using femtosecond pulsed lasers, [81][82].

When extending the concept to higher-order CARS, such as six-wave and eight-wave mixing, the process involves interaction of more excitation photons. The general principle remains the same: nonlinear interactions of multiple photons to excite a specific molecular vibration. However, these higher-order processes involve more complex interactions among more photons [81], resulting in smaller excitation area and higher resolution.

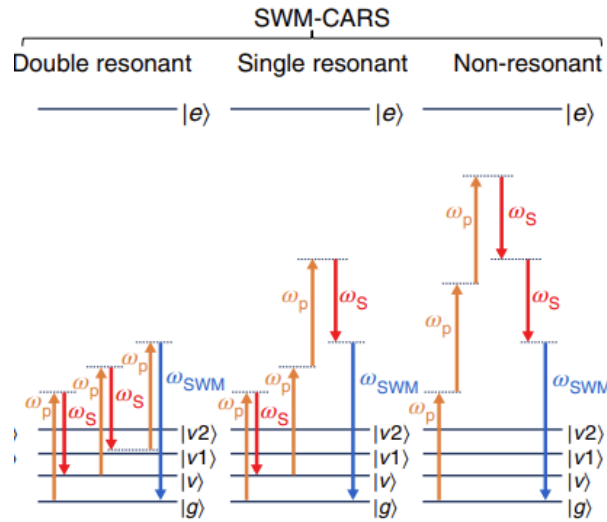


Figure 61: Energy Level diagram of Six Wave Mixing CARS signal

For six-wave mixing, the signal intensity might be represented as [81]:

$$I_{6WM} \propto |\chi^{(5)}|^2 I_p^3 I_s^2 \quad (76)$$

Here χ refers to the non-linear Raman susceptibility and N refers to the number of molecule. I_p and I_s are the peak intensity of Pump laser and Stokes laser respectively. The perturbation solution of $\chi^{(5)}$ and $\chi^{(3)}$ could be formulated through summing over the entire Feynman Diagrams [83]. The mathematical solution to χ is non-trivial, thus this report will not expand further on its derivation, Clark et al. [84]

For Raman Shift of around 3000cm^{-1} , Gong et al. [81] calculate the corresponding $\chi^{(3)} = 2.59 \times 10^{-4} \text{nm}^2 \text{V}^{-2} \text{M}^{-1}$ and $\chi^{(5)} = 2.45 \times 10^{-6} \text{nm}^4 \text{V}^{-4} \text{M}^{-1}$. Using the results from above, the normalized CARS signal intensity is calculated for 6WM and 4WM. The result is plotted using Matlab. Using the χ value stated above, the intensity distribution of the CARS signal is plotted for 4WM and 6WM. Figure 62 very clearly illustrates 6WM CARS results in higher resolution compared to 4WM CARS.

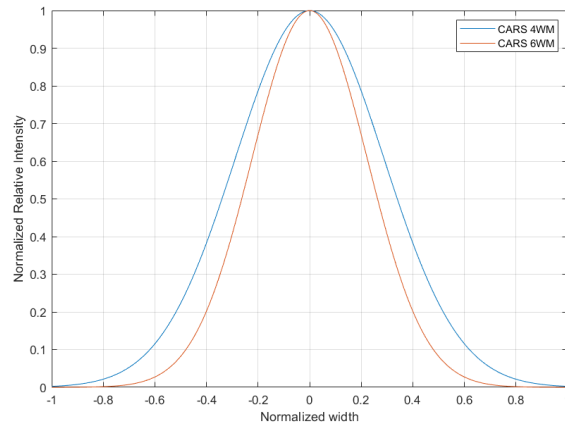


Figure 62: CARS intensity distribution under Gaussian beam excitation, the signal width is reduced compared to traditional 4WM CARS.

6.3.4 CARS Signal Intensity and wavelength calculation

To calculate the wavelength of the Coherent Anti-Stokes Raman Scattering (CARS) signal, the wavelengths of both the pump and the Stokes lasers are required. The energy (or frequency) of the CARS signal is essentially the sum of the pump photon's energy and the difference in energies (frequencies) between the pump and Stokes photons. This difference corresponds to the Raman shift, which is typically expressed in terms of frequency or wavenumbers but can also be converted back to wavelength:

For 4 wave mixing: Referencing to Figure 60, typically the probe beam is the same as the pump beam. Therefore the energy of the CARS signal could be written as

$$E_{CARS} = E_P - E_S + E_{Pr} \quad (77)$$

$$\omega_{CARS} = 2 * \omega_P - \omega_S$$

$$\omega_{4WM} = \frac{c}{\lambda_{4WM}} = 2 \frac{c}{\lambda_p} - \frac{c}{\lambda_s} \quad (78)$$

This equation is derived from the fact that the CARS process involves two pump photons and loss of a stokes photon.

For 6 wave mixing: Similar method as for 4WM, except for 6WM the process involves three pump photons, and loss of two stokes photons:

$$\omega_{6WM} = 3\omega_p - 2\omega_s \quad (79)$$

It is clear that the HO-CARS signal will have even higher energy than traditional CARS signals. Therefore lower wavelength than the two excitation laser beam.

Raman vibrational energy is often stated as Raman shifts. They are provided as wavenumber cm^{-1} , it is possible to derive an equation relating the Raman Shift to the two excitation wavelengths:

$$\text{Raman shift} = 10^7 \left(-\frac{1}{\lambda_p} + \frac{1}{\lambda_S} \right) \quad (80)$$

6.4 Example Spectra

CARS technique allows for excitation of specific Raman shifts, this significantly enhancing the imaging speed by avoiding the need to scan through a broad range of Raman shifts. By referencing to the Raman Spectrum of the molecule of interest it is possible to identify fingerprint Raman shifts. In practice, calculating the Raman shift and its associated intensity for each molecule presents a substantial computational challenge. Fortunately, several open-source databases exist, containing valuable data for biological and hydrocarbon samples. This report will rely heavily on such databases for referencing Raman spectra of interest.

The Raman spectra referred to in this project are outlined as follows:

polystyrene: Our optical tweezing system is designed to be compatible with polystyrene beads. Polystyrene bead is a very common drug carrier particle used in the industry. It is also a very simple molecular structure, resulting in a very simple Raman spectrum, see Figure63.

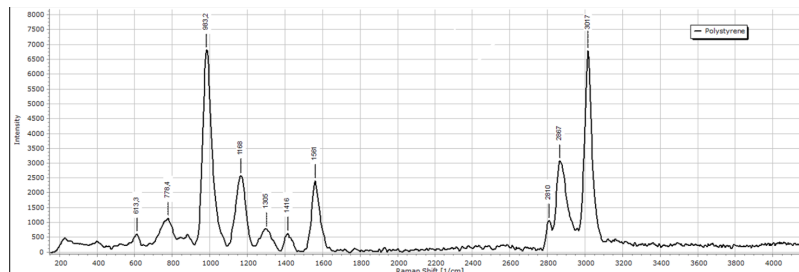


Figure 63: Polystyrene Raman Spectrum [85]

Polystyrene can be characterized by the peak at 3017cm^{-1} from the vibration of (C-H) bond. While the Aromatic ring results in the 1000cm^{-1} peak.[85]. The ability of the platform to distinguish between the polystyrene particle and cell is critical to our platform, Polystyrene has very distinct narrow peaks, making

it very easily identifiable.

Selection of Spectra for Cancer Cells: Figure?? is Raman spectra for skin cancer cells. The spectra for cancer cell are usually between 800cm^{-1} to 1800cm^{-1} [86]. The HO-CARS system must be able to image the entire active Raman spectra region of cancer cells and polystyrene beads, therefore the system must be able to excite Ramanshift from 800 cm^{-1} to 3100cm^{-1} .

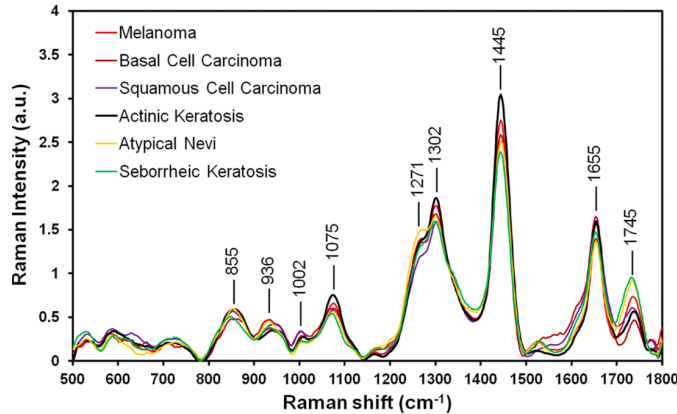


Figure 64: Cancer Cells Raman Spectra [86]

Raman Spectra for Solution:

Most of the key functionalities in our platform, such as laser ablation and optical tweezing, require the use of a high numerical aperture objective lens, with NA value greater than 1. This requirement dictates that the objective lens must be of the immersion/dipping type. A critical consideration in this setup is the Raman Spectra of the immersion fluid. It is essential to select a fluid whose spectral characteristics do not interfere with those of the cell and drug particles, ensuring clarity and precision in our observations and manipulations.

Figure65 and Figure66 are the Raman Spectra of some common immersion Solution:

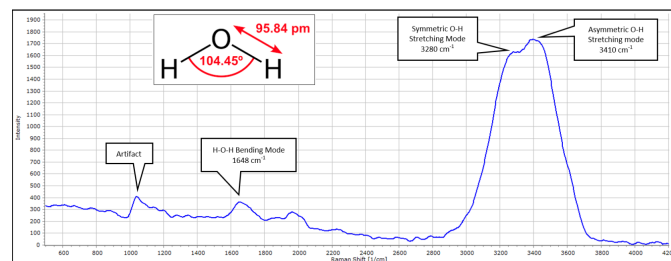


Figure 65: Water Raman Spectrum [87]

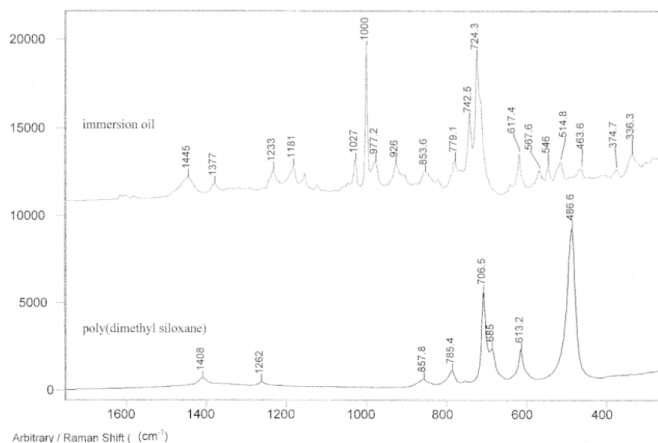


Figure 66: Standard Immersion Oil Raman Spectrum [88]

The prominent vibrational bands of the water molecule are between 3400 cm^{-1} and 3250 cm^{-1} . Given the simplicity of the water molecule, it is mostly characterized by the dipole moment. This results in fewer vibrational bands, leading to a much simpler spectrum. And more importantly, water lacks any organic bonds, commonly found in sub-cellular structures, this is evident through the relatively uniform presence between $800\text{-}1800\text{ cm}^{-1}$. This simplicity renders water an ideal medium for our platform.

In conclusion, We have chosen Polystyrene beads and water for their compatibility with the biological sample. Given the uncertainty regarding the specific organelles involved in the drug uptake process, the HO-CARS system needs to be able to image any Raman shift of interest that is within the cell's active Raman region. As a result, the HO-CARS system needs to be able to scan from 800cm^{-1} to 3100cm^{-1} .

6.5 Optical layout of our CARS system

The HO-CARS system is designed to collect three dimensional chemical image. The excitation wavelength will be chosen to excite specific finger-print Raman shifts of interests and steered to image the entire 3D space. Below is a diagram of the optical layout of the HO-CARS system.

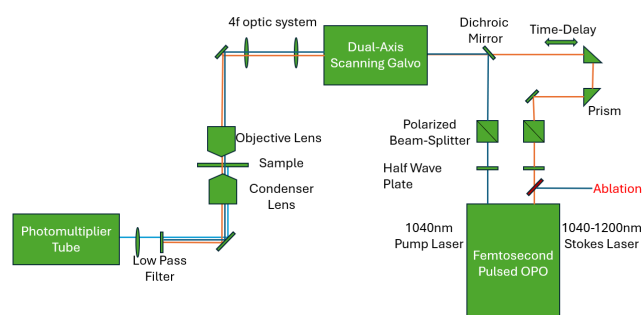


Figure 67: Optical Layout of the HO-CARS System

An Optical Parametric Oscillator outputs the Pump and Stokes beams at desired wavelength and pulse width. The output excitation beams are then directed through a series of half-wave plates and a polarizing beamsplitter for precise beam intensity control.

Following this, the merged beams are routed through a dual-axis galvanometer scanner and a pair of 4F lens sets for in plane beam scanning. The focal depth adjustment would be accomplished through varying the relative distance of the 4F lenses.

The Stokes and Pump beams then interact with the sample and cause the emission of the CARS signal. This combined beam is then collected through a condenser and passes through a short-pass filter. This filter removes the excitation beams, isolating the CARS signal for detection by the photomultiplier tube.

6.5.1 Laser & Optical Parametric Oscillator

Our platform already incorporates a femtosecond pulse laser for laser ablation, see Section 4.4.3. Therefore we can use the same laser source for both functions, enhancing performance significantly with minimal increase to costs.

For the HO-CARS setup, we require a Pump beam that is continuously tunable and a fixed Stokes beam. This requirement leads us to choose an Optical Parametric Oscillator (OPO) as our laser source. An OPO in itself is not a laser, rather it takes laser beam generated from a standard laser and convert it into two outputs: signal and idler.

We've opted for the Chameleon Discovery NX Ti:Sapphire Laser system by Coherent, a commercially available product that combines a femtosecond pulsed Ti:Sapphire laser with an OPO. It is specifically designed for CARS application, while still have sufficient power for laser ablation [89]. This system offers dual outputs: a constant beam at 1040nm and a tunable output ranging from 660nm to 1320nm.

Calculating the system's Ramanshift Range and Signal Wavelength:

The Ramanshift range of interest is between -400cm^{-1} and -3200cm^{-1} . This covers the Raman Spectra of cancer cells and polystyrene. Referencing to subsection 6.3.4, it is possible to calculate the excitation wavelength given the desired Ramanshift. Output B, 1040nm, will be used as the stoke beam. Output A, the tunable output, will be used as pump beam.

$$\text{Raman shift} = 10^7 \left(-\frac{1}{\lambda_p} + \frac{1}{\lambda_s} \right) \quad (81)$$

Setting the pump laser to the shortest wavelength will result in the largest excitable Raman shift. The

result is -5536.1cm^{-1} , larger than the specified -3200cm^{-1} .

$$\text{Raman shift} = 10^7 \left(-\frac{1}{660} + \frac{1}{1040} \right) \quad (82)$$

$$\text{Raman shift} = -5536.1\text{cm}^{-1} \quad (83)$$

For cell viability, it's best to use the longest possible wavelength for the energizing beam, ideally within the NIR range ($> 780\text{nm}$). The maximum Raman shift of interest, corresponding to Polystyrene beads, is around 3017 cm^{-1} . This is achieved by setting the tunable output (Stokes Beam) to 791nm . On the lower end, our platform can excite Raman shifts as minimal as 400 cm^{-1} by setting the tunable output to 1000nm .

The use of femtosecond pulse laser excitation enables six-wave mixing, in contrast to the conventional four-wave mixing, resulting in a CARS signal of higher energy. Consequently, the signal are emitted at a lower wavelength:

$$\lambda_{6WM} = \left(3\frac{1}{\lambda_p} - 2\frac{1}{\lambda_s} \right)^{-1} \quad (84)$$

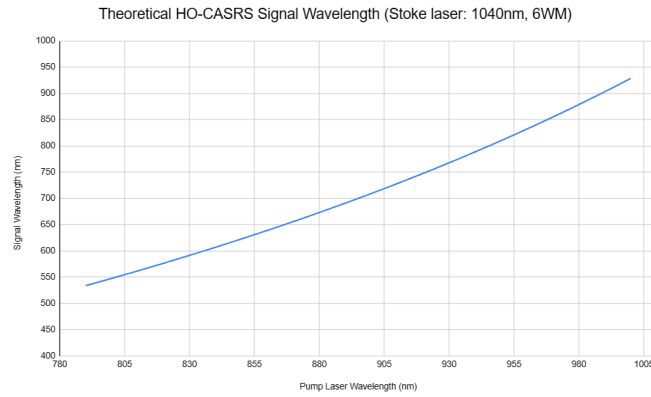


Figure 68: Theoretical HO-CARS Signal Wavelength vs. Pump Laser wavelength, note the overlap in the signal wavelength and pump laser wavelength.

Using the above equation, we anticipate the CARS signal wavelength to range between 534.8nm and 928.5nm . It is clear from the plot above that the range of the HO-CARS Signal overlap with the Pump Laser range. This adds some complication to the process of filtering out excitation beams prior to detection, and the filter system design will be discussed in detail in section 6.5.6.

6.5.2 Optical Component Choice and Efficiency

Optical Path:

The laser beam traverses the following components before reaching the sample: **1.** Half-wave plate; **2.**Polarized beamsplitter; **3.**Mirror; **4.**Two prisms; **5.**Dichroic mirror; **6.**Two Axis galvanometer; **7.**Two aspherical lenses; **8.**Two additional dichroic mirrors; **9.**Objective lens

Optical Transmission Efficiency:

While ideal optical components would transmit 100% of the light, real-world components invariably introduce losses. These losses occur at each stage as the beams traverse various elements. Additionally, the power output of the Optical Parametric Oscillator (OPO) varies with the wavelength, adding another layer of complexity to maintaining consistent output.

A half-wave plate and polarized beamsplitter are used as a tunable intensity attenuation system . They will be adjusted to ensure constant peak intensity at the sample across all wavelengths.

Mirrors and aspherical lenses, which are very standard in design for NIR wavelengths, will also be utilized. We will be using Anti-Reflective coated lens and High-Reflector mirror with a typical efficiency of 99%. The HO-CARS system utilizes three mirrors and two lenses (optic 3,6,7), resulting in a combined efficiency of these components of approximately 95%.

The primary concern regarding component selection involves the choice of dichroic mirrors and filters. Since the HO-CARS system uses a broad range of wavelengths and sometimes overlap with the wavelengths used by other systems. It is crucial to ensure that the dichroic filters are compatible with these wavelengths and do not eliminate any wavelengths of interest.

The first dichroic mirror in the system is used to combine the two laser beams from the Coherent laser. (optic 5). The tunable beam has wavelengths ranging from about 750 nm to 1000 nm, and the constant beam has a wavelength of 1040 nm. As shown in Figure 67, the mirror must reflect the 1040 nm wavelength while allowing shorter wavelengths to pass through. Thus, the Thorlabs Shortpass Dichroic Mirror/Beamsplitter with a 1020 nm cutoff wavelength is the ideal choice for this application.

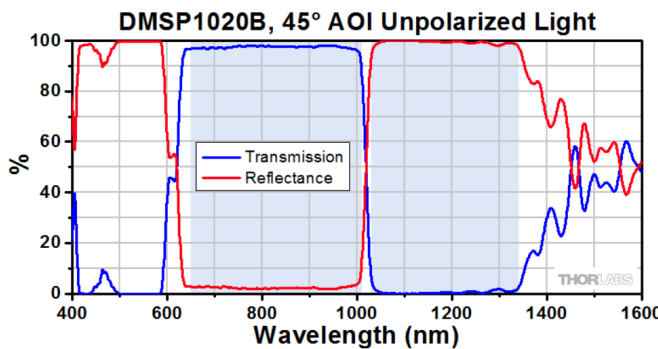


Figure 69: Thorlabs, DMSP1020B Dichroic Mirror[90]

According to Figure 69, the transmission band is between 650nm - 1010nm, and the reflection band is from 1030nm to 1340nm. Therefore fully satisfy the requirement. Thorlabs guarantees minimum 95% efficiency for the transmission and reflection bands.

The second and the third dichroic mirror on the beampath are used to merge the optical path of the HO-CARS imaging system with optical tweezing and wide-field imaging system. All the optical path for each system must all merge prior of the objective lens.

First, we will define the requirements for the dichroic mirror between the Optical Tweezer and the HO-CARS system. As detailed in Section 2.1.6, the optical tweezer uses a laser with a wavelength of 975 nm. This presents a unique challenge for the dichroic mirror since the tweezer's laser wavelength is within the bandwidth of the HO-CARS system. The HO-CARS beams need to transmit through the filter, while the optical tweezing beam (illustrated in blue in Figure ??) must be reflected by the beamsplitter, necessitating a notch beamsplitter. To minimize the loss in the Raman spectra that the HO-CARS system can image, the notch filter should be as narrow-banded as possible, centered at approximately 975 nm.

Typically, biological samples exhibit active Raman spectra from 800 to 1800 cm^{-1} , corresponding to wavelengths from 960 nm to 876 nm. Therefore, the bandwidth of the notch dichroic mirror, centered around 975 nm, must be 30 nm or less. While such a beamsplitter is not commercially available, there are no production filters that meet these requirements either.

It is possible to custom order beamsplitters that meet the above requirements from companies such as Semrock, Alluxa, and Thorlabs. Semrock manufactures a filter, NDF01-1040, with specifications close to our needs, with the reflection band centered around 996 nm instead of 975 nm [91]. Its transmission spectra, when placed at an Angle of Incidence (AOI) of 55 degrees, typically achieves a transmission

efficiency of 90%, which will be used in calculating the overall system efficiency.

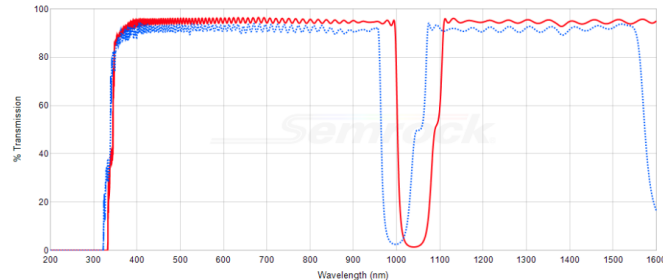


Figure 70: Transmission spectra of the the NFD1040 at AOI: 0° and 55°

The other beamsplitter reflects the wide-field image to its detection system while allowing other wavelengths to transmit through. This design is simpler as the wide-field system employs 550 nm light, whereas the other systems use much longer wavelengths ranging from 750 nm to 1040 nm. Therefore, a simple longpass dichroic mirror will be sufficient. The Thorlabs BMLP650 is chosen to ensure that the transmission band covers the entire bandwidth of the other systems. [92].

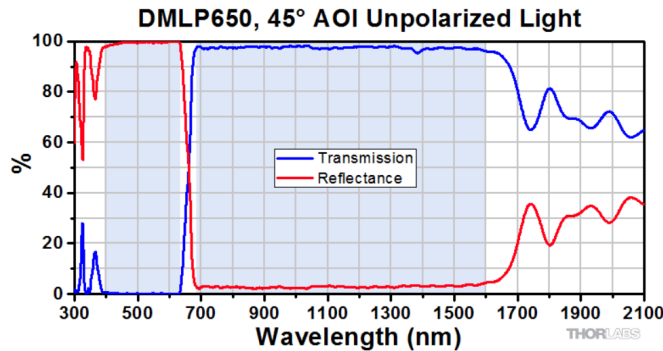


Figure 71: Longpass Dichroic Mirrors/Beamsplitters: 650 nm Cut-On Wavelength

The BMLP650 is unique in that its guaranteed transmission band extends well into the IR region, thus ensuring that the transmission efficiency is greater than 90% across the entire range of 750 nm to 1040 nm.

Lastly, as referenced in Section 4.3.7, all the systems in our platform share the same objective lens. Therefore, the choice represents a compromise among the requirements of each system. The objective lens chosen for our platform is the MRL07920, manufactured by Nikon.

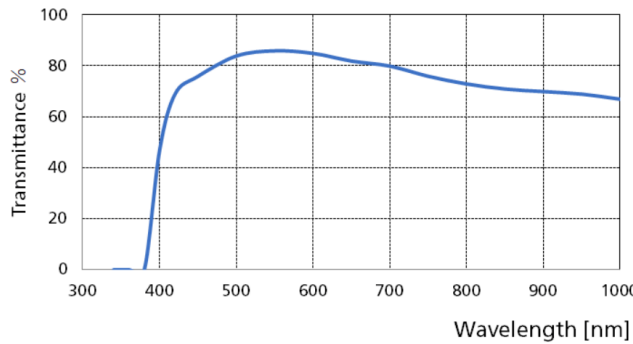


Figure 72: Transmittance graph for MRL07920, [93]

As the HO-CARS system utilises laser with between 750nm and 1040nm. the Transmittance is between 70% and 80%. Now combining all efficiency of each component, the total system efficiency is 31.8%. Therefore only 31.8% of the output power will reach the sample.

$$\text{System Efficiency} = \prod \text{Component Efficiency} \quad (85)$$

$$\text{System Efficiency} = 0.99^5 * 0.95 * 0.9^2 * 0.7 = 31.8\% \quad (86)$$

6.5.3 Intensity Control, Power Delivered to the Sample

Photodamage Threshold:

Research indicates that the threshold for cell photodamage can be expressed as a function of excitation intensity and exposure time: $I^2\tau < \text{Constant}$, with the commonly accepted lower threshold ranging between 20 to 100 $\text{TW}^2\text{cm}^{-4}\mu\text{s}$ [94]. Typically, strategies involve reducing exposure time while increasing intensity, with the shortest exposure being in the tens of microseconds. For our platform, we have set the threshold at $40 \text{ TW}^2\text{cm}^{-4}\mu\text{s}$ and an exposure time of $10 \mu\text{s}$, yielding a maximum peak intensity of 2 TW cm^{-2} .

Power Output and Wavelength Considerations:

The average output power of our laser fluctuates between 2000 and 3700 mW [?], depending on the output wavelength. The system operates with a pulse width of 100 fs and a repetition rate of 80 MHz. Calculations for consistent intensity delivery at the sample are based on the lowest average power output scenario.

The lowest wavelength utilized by the HO-CARS system is approximately 780 nm. By interpolating the energy output between 700 nm and 800 nm, we estimate the output at 780 nm to be around 3280 mW.

Peak Power Calculation :

To determine the peak intensity at the sample plane, it is necessary to calculate both the peak power and the spot size at that location.

$$P_{peak} = \frac{P_{avg}}{\text{Pulse Width} * \text{Repetition Rate}} \quad (87)$$

Using values of $P_{avg} = 3280W$, Pulse Width=100 μs and Repetition Rate=80MHz, the calculated peak output power is 407500W. As the overall efficiency of the optical system is 31.8%. Without any attenuation from the polarizing beamsplitter, the power delivered to the Sample is 129585W.

Final Power Delivery :

We will be using MRL07920 Objective lens to focus the laser beam onto the sample. It has a numerical aperture of 1.1. By applying the following formula, it is possible to calculate the theoretical beam waist size.

$$S = \frac{4M^2\lambda f}{D\pi} \approx \frac{2M^2\lambda}{NA\pi} \quad (88)$$

Where S is the Spot radius, M^2 is beam quality factor , λ is wavelength of the beam, NA is the numerical aperture.

The Coherent Laser's beam quality is roughly 1.2. For the scenario with the longest wavelength used (1040 nm), the resulting spot size is 722 nm. By combining the spot size and peak power, we can calculate the peak intensity at the sample.

$$I_{peak} = \frac{P_{peak}}{\pi * (\text{beam radius})^2} \quad (89)$$

This yields a peak intensity on the order of $1 * 10^{13} W cm^{-2}$, which is substantially higher—by a factor of 100—than the threshold for photodamage. This is expected as the laser is chosen to have sufficient power for laser ablation. Therefore, the laser intensity must be attenuated by approximately 100 times using the half-wave plate and polarized beamsplitter configuration.

Intensity Adjustment Mechanism:

The HO-CARS system employs a half-wave plates and polarized beamsplitter to adjust beam intensity—this configuration mirrors that used in laser ablation systems. By altering the relative angle between the wave plate and the polarized beamsplitter, beam intensity can be finely tuned and attenuated, the working

principle of this system is explained in Section4.3.2:

$$I = I_0 \cos^2(2\phi) \quad (90)$$

$$\frac{I}{I_0} = \cos^2(2\phi) \quad (91)$$

The average output power spectrum is constructed from linearly interpolating values provided in the laser specification sheet. The following linear piece-wise function represents the Output Power spectrum.

$$P_{avg} = \begin{cases} 2000 + 16(\lambda - 700) & \{800 > \lambda \geq 700\} \\ 3600 - 4(\lambda - 800) & \{900 > \lambda \geq 800\} \\ 3200 - 5(\lambda - 900) & \{1000 \geq \lambda \geq 900\} \end{cases} \quad (92)$$

Therefore the associated Peak excitation intensity spectrum can also be modeled by first solving for the peak power, and then the peak intensity, using methods explained in Section6.5.3. Using the Peak Intensity spectrum, we can calculate the theoretical angle between the polarized beamsplitter and the half-wave plate required to ensure that the peak intensity measured at the sample remains constant at $2TW cm^{-2}$. The result is shown in Figure73.

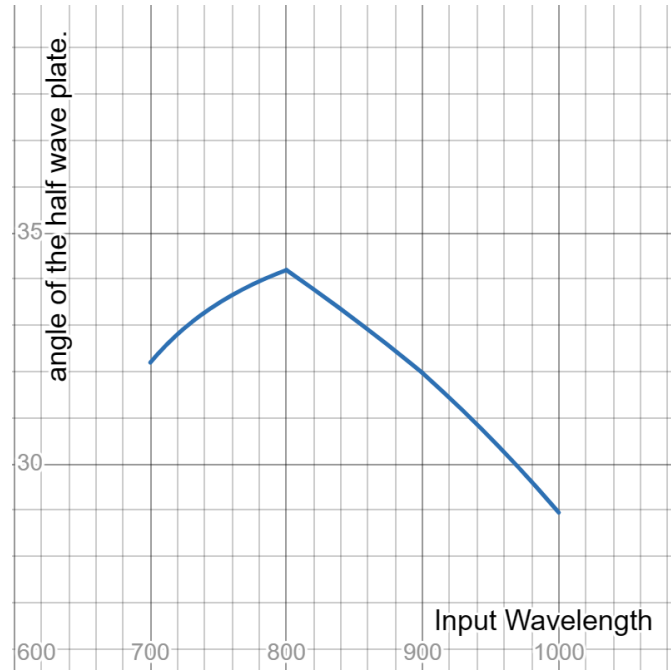


Figure 73: Azimuthal angle of polarized beamsplitter at different laser wavelength

The exact azimuthal angle needed is calculated and depicted in Figure 73. This results in an approximate 0.011-degree rotation per 1 nm change in wavelength. Consequently, a relatively inexpensive Thorlabs ORIC® Rotation Stage could be utilized to precisely control the angle of the half waveplate. It is chosen to rotate the half waveplate instead of polarizing beamsplitter to ensure the final polarization of the laser beam is constant for the dichroic mirrors. [95].

Depending on the biological sample used and empirical data collected by the system, the operator would be able to fine tune the peak excitation power when operating the system by simply commanding the rotation stage to a different azimuthal angle.

6.5.4 Optical Scanning System

The HO-CARS laser beams excite only one spot on the sample at any given moment; therefore, the beams need to be mechanically steered to scan the entire sample. To achieve this, a 4F optics scanning system is used, consisting of two galvanometer mirrors and two aspherical lenses.

A 2-axis galvanometer is used to steer the laser beam on the focal plane, and the relative distance between the 4F lenses is used to adjust the axial focal distance. The analysis primarily focuses on setting up the system to image the focal plane.

A galvanometer (galvo) mirror is essentially a mirror attached to a servo motor, which allows it to rotate and reflect the laser beam at various angles. Each axis of rotation provides the system with one-dimensional scanning capability. Two galvo mirrors with independent axes of rotation are required to steer the beam in 2 dimensions, see Figure74.



Figure 74: ThorLabs 2D Galvo Mirror Beam Path[96]

Thorlabs manufactures commercially available galvanometer mirrors. By having two axes of rotation, these mirrors can direct the beam to any point on a 2-dimensional plane. However, using only the galvo

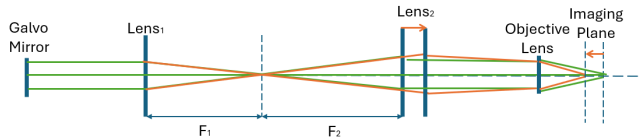


Figure 75: Two aspherical lenses (Lens 1 and Lens 2) are placed so that their back focal points coincide. Collimated ray is imaged onto the objective lens (green rays). When Lens 2 is moved away from Lens 1, the rays entering the objective are no longer collimated, resulting in the imaging plane moving closer to the objective (orange rays)

mirror would result in the reflected beam completely missing the objective, as it would be deflected off the optical axis. The solution to this problem is to implement a 4F imaging system.

This system relies on two lenses to image the deflected beam at the back focal plane of the objective. The working principle can be explained through Fourier optics; each lens can effectively be seen as performing a Fourier transform, imaging the beam onto a Fourier plane. By combining two lenses, the beam is first transformed into the Fourier plane and then reformed back to its original image at the back focal plane.

This setup is particularly powerful for optically processing the signal and applying various filters. In this application, it is used primarily to ensure that the spatial location of the laser beam remains unchanged, while only the incidence angle of the beam at the objective is altered. An added benefit is that by fine tuning the distance between the 2 lenses, it is possible to adjust the focal length of the system. Hence the system is able to control the axial location of the focal point on the sample, allowing us to image at different depth, see Figure 75.

By applying Snell's Law and assuming a thin lens, we can derive the equation that defines the relationship between the angle of rotation of the mirror and the angle at the objective's back focal plane. The focal distance and the angle of refraction depend on the refractive index of the lens material, the incident beam angle, and the surface curvature. The thin lens assumption posits that the radius of curvature of the lens is significantly smaller than its diameter, allowing us to neglect the thickness of the lens.

Quoted from Physics LibreText: "In the case of a converging lens, these rays do not converge at the focal point. Instead, they meet at another point on a plane called the focal plane, which contains the focal point and is perpendicular to the optical axis. As illustrated, parallel rays focus at the intersection where the ray through the center of the lens meets the focal plane." [97]

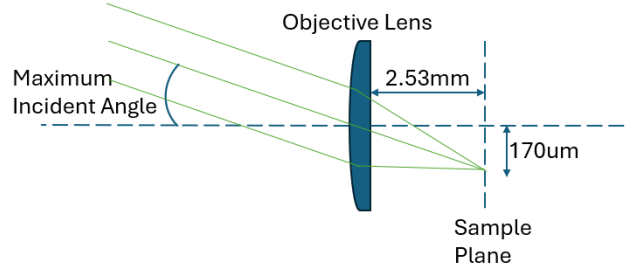


Figure 76: Maximum Incident Angle for the required scanning area

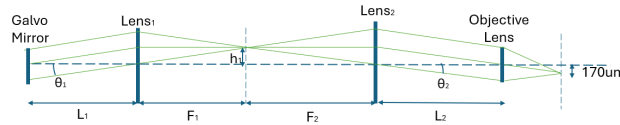


Figure 77: Diagram of the 4f scanning system

Given that the laser beam is collimated, after being reflected off the galvo mirror, it will be incident on the first lens at an angle and be focused onto a point in the focal plane. By considering the ray that passes through the optical axis, we can directly calculate the focal point on the focal plane.

The second lens is positioned one focal length away from the focal plane. Effectively, the rays can be seen as emanating from a point source at the focal plane of the second lens. This lens then converts them back into collimated rays, but at an oblique angle.

Now, by working backward from the required scanning area and the focal length of the objective lens, it is possible to calculate the necessary maximum angle of incidence on the back focal plane of the objective lens.

Given the desired max linear displacement is $170\mu m$ and the focal length is 2.53mm, the required max θ_2 is 3.86° . The value will be used for the calculation of the size of $Lens_2$ and distance from $Lens_2$ to the objective lens.

$$\text{Incident Angle}_{max} = \tan^{-1}\left(\frac{170\mu m}{2.53mm}\right) \quad (93)$$

$$\text{Incident Angle}_{max} = 3.86^\circ \quad (94)$$

Using Figure 77 We can easily derive the equation which related the galvo mirror output beam angle and

its associated linear displacement at the sample plane.

$$\theta_1 = \tan^{-1}\left(\frac{r_1 - \frac{D}{2}}{L_1}\right) \quad (95)$$

$$h_1 = F_1 * \tan(\theta_1) \quad (96)$$

$$\theta_2 = \tan^{-1}\left(\frac{h_1}{F_2}\right) = \tan^{-1}\left(\frac{r_2 - \frac{D}{2}}{L_2}\right) \quad (97)$$

Where r_1 and r_2 is the respective radius of the aspherical lens. F_1 and F_2 is the respective focal length. D is the beam diameter, and h_2 is the linear displacement of the spot at sample plane.

$$h_2 = 2.53mm * \tan(\theta_2) \quad (98)$$

By rearranging the equations above, the theoretical relation between θ_1 and h_2 is:

$$h_2 = 2.53mm * \frac{F_1}{F_2} * \tan(\theta_1) \quad (99)$$

Between the second aspherical lens $Lens_2$ and the objective lens, the beam will have to pass through several dichroic mirror. Therefore a large 75mm diameter, 60mm focal length aspherical mirror manufactured by Edmund optics is used as $Lens_2$. Applying the equations above, the large diameter will allow for a maximum of 550mm between the $Lens_2$ and the Objective lens, thus giving sufficient space for the placement of dichroic mirrors.

A smaller 30mm diameter and 26mm focal length aspherical mirror is as the first aspherical lens $Lens_1$. This is because a smaller focal length F_1 will require lower angular resolution for the same level of linear resolution. And as there is no additional optics between the $Lens_1$ and the galvo mirror, the distance between the could be much closer. Using the equations listed above the maximum allowable distance between the two component is 30mm.

This set up is also verified using Matlab ray tracing package OptoMetrika. A similar 4F scanning system in 1 dimension is modeled.

OptoMetrika is a iterative ray tracing package that solves for the optical image using snell's and Fresnel's Law. The galvo mirror is fully defined by a 3D location vector and a 3D attitude vector. The lens is similarly defined, however with additional characteristics such as the curvature and refractive index. THE

curvature of the lens is carefully chosen such that the focal length ratio is still maintained.

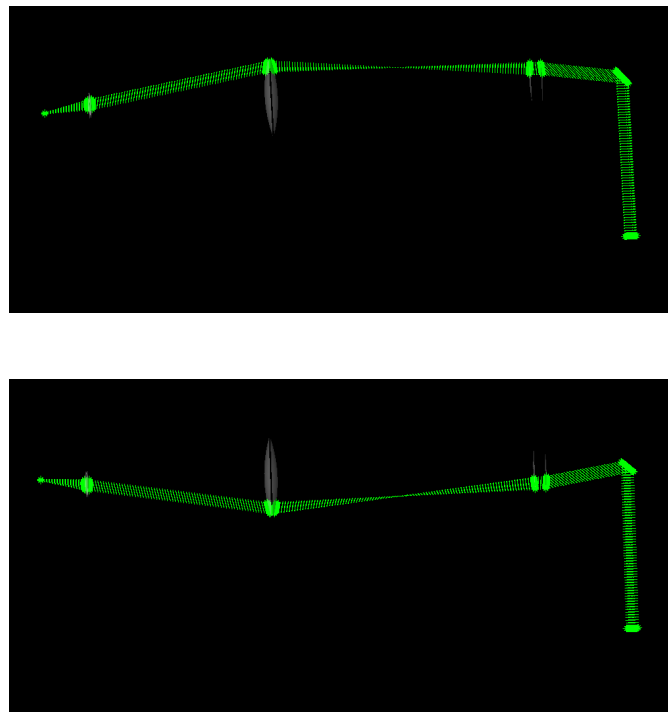


Figure 78: Ray tracing Model of the 4F system

Ray tracing confirms that the calculations for the focal length ratio and the diameter ratio are correct. The system also serves to amplify the angular rotation, such that the rotation at the galvo mirror is 2.3 times larger than the angle of incidence at the objective. This amplification is intentionally designed to reduce the precision requirements for the galvo mirror.

The ray tracing verifies the theoretical calculations. The scanning system is designed to cover a scanning area of $340\mu m$ by $340\mu m$, requiring each mirror to rotate from -8.3965° to $+8.3965^\circ$. To minimize the effects of aberration, only the central half of the lens diameter will be used, resulting in a scanning area of $200\mu m$ by $200\mu m$, which is slightly greater than the field of view of the widefield imaging system.

6.5.5 Imaging Time

The entire imaging area ($200\mu m \times 200\mu m$) comprises 666×666 individual scanning spots. The dwell time is set at $10\ \mu s$ per spot. Therefore, obtaining an image of the entire area for one Raman shift would take approximately 4.4 seconds.

As the sample measures only $50\mu m \times 50\mu m$, it would take about 0.27 seconds to scan the entire sample for each Raman shift. By using data collected from the widefield imaging system, the scan area can be further reduced, thus decreasing the imaging time even more.

6.5.6 Signal Detection System

A Photomultiplier Tube (PMT) will be used to detect the HO-CARS signal emitted from the sample. This signal will be focused using a condenser. A high numerical aperture condenser lens is employed to collect as much of the emitted signal as possible.

The highest Raman shift of interest is 3017 cm^{-1} , achieved using a 791 nm pump beam excitation. This results in a focal spot size of $\omega_p = 549\text{ nm}$. The Stokes laser has a focal spot size of $\omega_s = 722\text{ nm}$. The expected signal output, due to six-wave mixing mechanisms, leads to a resolution of the HO-CARS signal of $\omega_{6WM} = \frac{1}{\sqrt{\frac{3}{\omega_p^2} + \frac{2}{\omega_s^2}}} = 316\text{ nm}$ [81].

A photomultiplier tube is chosen over CMOS or CCD sensors primarily for its sensitivity and unparalleled rise time. As the HO-CARS system is designed to scan mechanically through the sample area, activating only one spot at any moment, the sensor needs to measure only intensity data, not location data. The HO-CARS signal is relatively weak and the exposure, or dwell time, is only $10\mu\text{s}$; therefore, the primary concern is the sensitivity and rise time of the sensor. The optimal solution for measuring intensity is to count the number of incident photons during the dwell time, which is precisely what a photomultiplier tube is designed to do. In our system, we will be using the Hamamatsu R2066 photomultiplier tube [98].

The photomultiplier tube does not differentiate between different wavelengths of light, as long as they are within its spectral response range. This poses a challenge, as the signal is mixed with the excitation beams, and all three wavelengths pass through the condenser. As shown earlier in Figure 68, the signal's wavelength range actually overlaps with that of the excitation beam; thus, it is not possible to use a single filter to isolate the signal. Instead, different filters must be used for different excitation wavelengths. These filters will be installed on a Thorlabs Motorized Fast-Change Filter Wheel.

Filter 1: Edmund Optics 700nm Cut off lowpass filter: Transmission band:400nm - 685nm. Rejection Band: 715 - 1050nm. The upper bound of the rejection band is exactly 10nm higher than the highest excitation wavelength which is 1040nm. This filter is used for excitation beam of wavelength up to 880nm.

Filter 2: Edmund Optics 800nm cut off lowpass filter: Transmission band:400nm - 790nm. Rejection Band: 825 - 1190nm. This filter is used for excitation beam of wavelength longer than 880nm, but shorter than 930nm.

Filter3: Edmund Optics 900nm cut off lowpass filter: Transmission band:425nm - 890nm. Rejection Band: 930 - 1250nm. This filter is used for excitation beam of wavelength longer than 930nm, but shorter

than 960nm.

Filter4: Edmund Optics 950nm cut off lowpass filter: Transmission band:450nm - 939nm. Rejection Band: 930 - 1250nm. This filter is used for excitation beam of wavelength longer than 960nm.

6.6 Cost Estimation

Shared Item:

Component	Quantity	Price per item (£)	Total price (£)
Chameleon Discovery NX	1	100,000	100,000
Dichroic Mirror	2	750	1500
Objective Lens	1	28,000	28,000
Condenser	1	2000	2,000
Shared system cost: £131,500			

HO-CARS specific Items

Component	Quantity	Price per item (£)	Total price (£)
Half wave plate	2	360	720
Polarizing beamsplitter	2	200	400
Rotation Stage	2	4100	8200
HR Mirror	2	150	300
Prism	2	75	150
2-axis Galvanometer	1	12000	12000
Aspherical Lens	2	500	1000
Detection Filter	4	410	1640
Filter Wheel	1	1,700	1700
PMT	1	1900	1900
HO-CARS system total cost : £28,010			

6.7 Safety Consideration

Referencing Section 4.6, the Coherent Chameleon Discovery NX laser system is classified as a Class 4 laser: may cause severe, permanent damage to the eye or skin without being focused by the optics of the eye or instrumentation. Even diffuse reflections of the laser beam can be hazardous.

The entire HO-CARS system will be enclosed, with all access panels interlocked so that the laser automatically turns off if any panel is removed. There will be no intra-beam viewing; all images and data will be collected through sensors. All unused beams will be terminated using pulsed laser beam blocks.

However during the Initial alignment and any non-routine operations, the system would be considered a class 4 system, and therefore the system must be used inside laser control area. According to the EN 207 standards, requiring the operator to use laser goggle with minimum M-LB9 rating.

With these safety measures in place, under normal operating conditions, there is minimal or no risk of user exposure to laser beams. The system would be considered Class 1, operable by users with minimal additional risk.

6.8 Summary

In summary, our Higher Order Coherent Anti-Stokes Raman Scattering (HO-CARS) microscopy is a potent tool for label-free chemical discriminant imaging of cells. Our system uses dual-wavelength femtosecond pulsed beams to enable higher-order multi-photon excitation, which significantly enhances the spatial resolution to 216nm.

The HO-CARS system is capable of exciting and measuring Raman shifts from 400 cm^{-1} to 3200 cm^{-1} , covering the entire range of interest for cell samples. This broad detection capability allows for the simultaneous transfection and study of multiple drugs, providing unique chemical imaging opportunities.

The total imaging area ($200\text{ }\mu\text{m} \times 200\text{ }\mu\text{m}$) consists of 666×666 individual scanning spots. This large area ensures that the entire sample is within the field of view, regardless of the position of the mechanical stage. The imaging time can be reduced by focusing on areas of interest rather than scanning the entire area.

Lastly, the HO-CARS imaging system is designed to minimize the risk of photodamage. The current design limits the peak intensity to 2 TW cm^{-2} . The intensity can be easily adjusted by the operator using a polarizing beamsplitter, making the system suitable for long-term studies of living cells.

7 XY Control - Tom Sharrock

7.1 Design Objectives of XY Control

The purpose of the stage control is to position the cells correctly relative to the laser focal point, quickly and accurately. Each cell to be operated on is attached to the bottom of the petri dish, which is divided into $50 \times 50\mu m$ squares containing a cell each. The ablation laser and imaging systems have no movement capability, so the stage must move the sample with sufficient spatial resolution. Widefield imaging provides the coordinates of cells to be input into the control system, which has been designed cover an area of $100mm \times 100mm$, which gives full access to a variety of sample dish sizes. The smallest particles to be tweezed are $2\mu m$ in diameter and must be inserted through a $3\mu m$ hole, so the precision of the stage must be $< 0.5\mu m$.

Covering up to $100mm^2$ with sub-micrometer accuracy is very difficult to achieve with a single control mechanism¹. Therefore, a hybrid system is used which combines coarse and fine control to give high precision over a large range. The coarse control is used to place the sample within $50\mu m$ of the desired position; subsequently, the fine control mechanism adjusts the final position with sub-micrometer accuracy. This combination is shown with scale in Figure 79. Stacking stages with a duel-stage setup is ideal for this purpose, but moving the entire fine control stage reduces the dynamic response of the coarse motion. However, the dynamic response of the entire system is not a key consideration here. We will operate on 9 cells at a time (3×3 grid) as discussed in Section 5.0.1, and setting the range of the fine stage to be $1mm \times 1mm$ allows it to access 324 cell locations before the coarse controller is needed again. Therefore, although the coarse control moves longer distances, its infrequent use means that the compromise on its performance is negligible.

One of the key design features for the stage control is the repositioning time. Specifying this to be an order of magnitude smaller than laser operation time is reasonable, as it becomes negligible compared to the total operation time whilst avoiding excessive cost. Although the wide-field imaging Cell Edge Detection process determining the cell positions takes a few seconds, which is a long time compared to the ablation and tweezing processes, this only needs to be carried out once for each sample of cells. Once the image has been processed, the positions of each can be passed to the controller, and therefore the imaging

¹Long-distance and high accuracy sensors can be used with some stage designs that allow for large displacements over a large working space. However these are very expensive and require careful and delicate calibration. Furthermore, hysteresis becomes a big issue over larger ranges, as more non-linearities are introduced, and this causes many problems which are very difficult to account for.

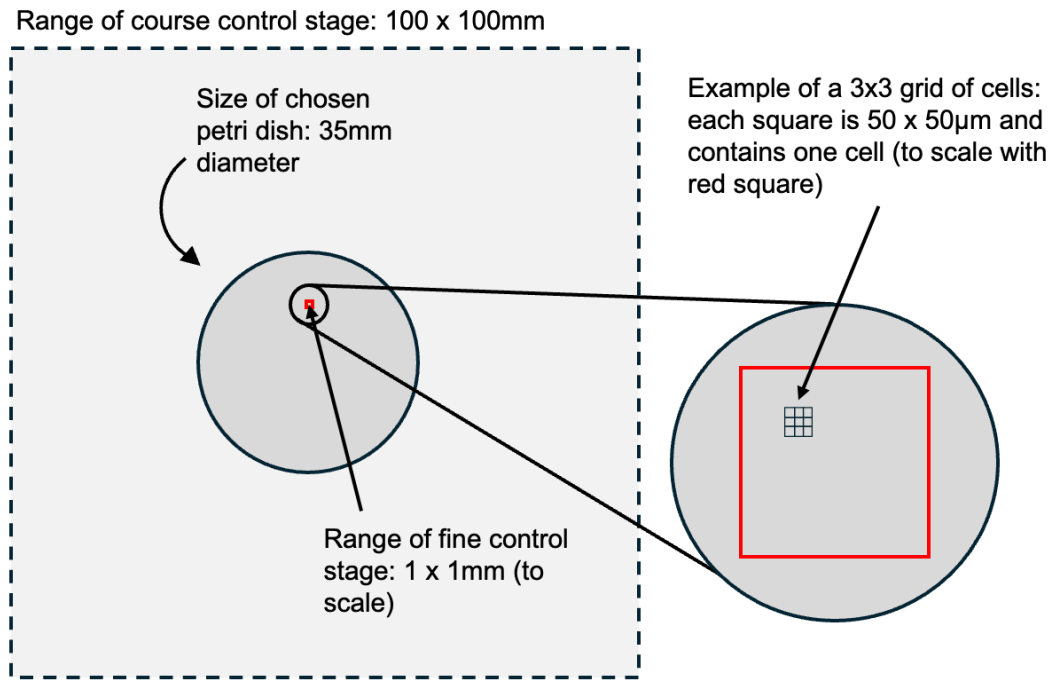


Figure 79: The relative ranges of each stage are shown to scale: the coarse control stage range is shown in the dotted region; our chosen petri dish (to scale with coarse range) is larger black circle; and the fine control stage range is also to scale and in red. This is magnified to show the relative size of the petri dish grid containing the cells.

does not slow down the operation any further. Chemical imaging is used as a post-processing technique to determine the success rate of operation, so does not need to be considered when calculating the process time per cell. Given the ablation process takes 100ms (Section 4.4.5) and the tweezing takes 540ms (Sections 3.5.4 and 3.5.4), a value of 60ms is used as the maximum repositioning time.

7.2 XY Coarse-Control

The range of the fine control stage is 1mm 7.3, so the responsibility of the coarse stage (at a minimum) is to place the fine stage within this distance of the required cell. This provides access to any cell in the dish with high-resolution positioning. However, in the worst case scenario, the coarse controller would be required to adjust position for every cell. To avoid this, the coarse resolution is increased (relatively easily) to 50 μm . This means it is possible to deliver the fine stage directly to the correct cell, minimising the number of times the coarse stage must be used. The measurement of the coarse stage position needs to be to the same precision as the fine stage in order to have a suitably precise reference position for the fine controller. The detailed analysis of the coarse aspect of the control is beyond the scope of this project, but an outline of how it would be carried out is given to provide context for the fine control analysis, which is subsequently provided in detail.

Many motor types on the market have the specified requirements. [99] uses a magnetic linear motor for their coarse actuation, and inspired by this we are using LinMot's synchronous linear motor, which has over a metre of range and resolution of $50\mu m$. For position measurement, a laser interferometer is needed to provide the required precision over the range, with the sensor attached to the stage. The Keysight 10715A sensor is chosen for its nanometer resolution [100]. To provide sufficient range in the coarse mechanism, long, leaf-type flexure hinges are used, similar to in [101].

One problem that is often encountered with dual-stage positioning systems is the combination of control performance when the stages are adjusted simultaneously [102]. However, this will not be an issue for our system: the coarse controller can be used in isolation to place the fine control stage on the grid, after which point the fine control mechanism can work in isolation as well. This justifies the fine control mechanism analysis without consideration of the coarse system.

7.3 XY Fine Control

As described in 7.1, the fine control system is required to position the sample with sub-micrometer accuracy over a range of $1mm$ after being roughly positioned by the coarse controller. $1mm$ is selected as it provides access to 36 of the 3×3 cell grids, with a $50\mu m$ boundary either side to allow for coarse positioning inaccuracies. Combining the stages in series leads to poor coarse control dynamics that are justified by the large range of the fine stage, as many cells can be accessed without addition coarse adjustment. On the other hand, making it larger still would require larger deformations and therefore higher stresses to be applied to the hinges 7.4.1. A range of $1mm$ allows access to many cells without placing too much stress on the hinges. The stage also needs to achieve each movement in under $60ms$, whilst maintaining stability and minimal overshoot to avoid disturbing the sample.

Most applications that require sub-micrometre accuracy cannot be achieved with conventional mechanisms using motors, gears and joints. This is mainly due to the associated hysteresis and friction and the geometric and dimensional errors of the components. Instead, flexure hinges are often used in stage designs where high precision positioning is required. These create hinges by varying the thickness of material to choose where it will bend under load. The material stiffness is exploited to produce controlled and stable movements. High precision actuators, such as electromagnetic and piezo motors, can be used to drive the stage motion and achieve high-accuracy, closed loop control.

7.3.1 Actuation

To meet the specifications outlined in 7.1, the actuator for the stage will need to following capabilities:

- **Quick-repositioning:** whole process under 60ms
- **Good stability:** must be able to hold in place for a significant time period whilst not varying by more than a few 10s of nanometers (a few % of the hole size).
- **Range of at least 1mm**
- **High precision positioning:** the ablation holes are intended to be $3\mu\text{m}$ in diameter, so positioning within 10% of this is reasonable.

With these factors in mind, an ultrasonic piezo motor developed by Xeryon is chosen as the actuator for the fine stage control. Piezo motors exploit the piezoelectric effect: a phenomenon that occurs as a result of the interactions between the mechanical and electrical states in some crystalline materials [103]. When force is applied to piezoelectric materials (structures including quartz, bone, and some ceramics), an electric current is generated. This can be very carefully controlled and used to drive actuators with great precision. Piezo motors are especially good at moving very short distances (down to nanometer scale) quickly and can do so in rapid bursts whilst remaining stable between. This is ideal for the needs of our platform, which will have to quickly move from cell-to-cell during operation.

The particular model chosen is the Xeryon XLA-10-55-312 [104], shown in Figure. It has a maximum force output of 10N , which is the highest in the range offered by Xeryon, and allows the stage design to be a bit stiffer and therefore more robust than weaker models. The 55 refers to the rod length, and this provides a 15mm stroke length (range). 312 specifies the closed loop encoder resolution, i.e. 312nm^2 . This allows for 312nm step sizes, which is around 10% of the hole as required. Xeryon do offer a model with a 78nm linear encoder, however the extra resolution is unnecessary for our purposes and would cost significantly more.

7.3.2 Position Measurement

The position sensor for the stage will be placed in the mechanism (detailed in section 7.4.2) such that it can measure the displacement of the moving part of the mechanism relative to the fixed part. This isolates the measurement of stage displacement from the coarse motion and provides position feedback to the controller. This is necessary because, although the piezo motor can be instructed to move in very precisely controlled steps, it has no absolute reference point. To provide precise and regular data to the controller, a CPL590 capacitive sensor from Lion Precision [105] is used. The extended model with

²The optical encoder comes with the motor as part of its own control system. It does not contribute to our feedback controller.

5.6mm sensing diameter is selected, as this has a $2000\mu m$ range. A resolution of $26nm$ at a sampling rate of $10kHz$ is quoted, which is sufficient to provide accurate and precise positioning feedback.

By combining measurements from the capacitive position sensor on the fine stage mechanism with the interferometer on the coarse mechanism, an accurate value of the absolute position of the stage can be given to the controller.

7.4 Fine-Control Stage Mechanism Dynamics

To achieve the necessary accuracy and precision motion in the XY stage, a novel, purpose-specific stage mechanism is designed. There are two basic structures for XY stages: series and parallel. Most series stages used two stacked, 1-degree-of-freedom (DOF) designs that combine to give well decoupled movement in 2DOF. Despite the benefits of simple design and decoupled movement, series stages suffer from a number of issues, such as error buildup and having to move heavy actuators. This increases the inertia of the system, decreasing the dynamic mobility, and making them more difficult to control.

By contrast, parallel stages use kinematic chains that have actuators attached to the same base. Closed kinematic loops give high rigidity, loading capacity and accuracy, and are therefore preferable to serial setups. However, some parallel stages still suffer from input and output coupling. Input decoupling can be defined as an actuator in the X-direction being affected by the actuation of another in the Y-direction. Although these unintentional displacements are quite small, they can damage the actuators with additional loads. Output decoupling can be defined as whether an actuator is able to drive the motion stage in the intended axial direction only. Coupled outputs complicate calculations of position, as displacements in both directions have to be considered for a force applied in a single direction. Both of these issues can be removed with careful design by exploiting the dynamics of compliant mechanisms: flexible structures that achieve force and motion transmission through elastic body deformation, often via the use of flexure hinges. The aim of the design presented here is to produce a stage with no input or output coupling, and is capable of positioning the cells with high precision and repeatability, whilst maintaining sufficient range to cover the entire workspace area.

Examples of parallel mechanisms that produce decoupling are shown in Figure 80. It can be seen that they allow motion of the stage only in the direction that the force is applied.

7.4.1 Flexure Hinges

The stage design is based on multiple compliant parallel mechanisms that are combined to produce entirely decoupled motion by exploiting flexure hinges. Theoretically, one could add more and more

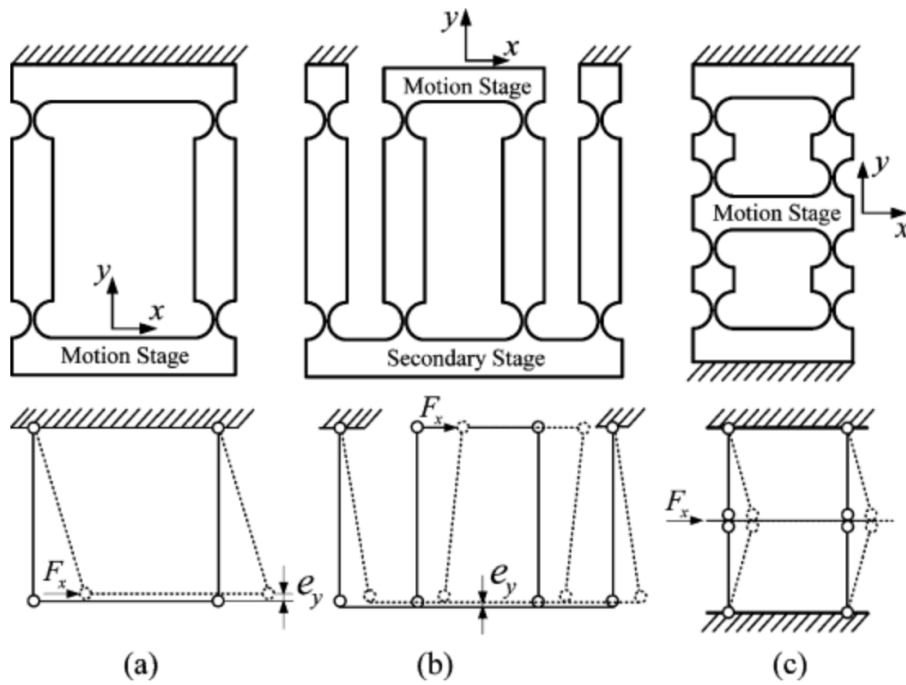


Figure 80: Three types of parallel flexure mechanisms [106], which are used to decouple motion in the different DOF. Combining many of them into a larger mechanism improves performance. (a) Conventional parallelogram. (b) Double parallelogram. (c) Double four-bar.

mechanisms in parallel and achieve better and better decoupling. However, each addition provides exponentially decreasing returns whilst significantly increasing the size and mass of the stage. For practicality, cost, and efficiency reasons, the design is chosen because it uses the minimum number of parts whilst still providing sufficient decoupling. The material choice for the stage is aluminium 7075-T6, as it is known for its large reversible strain [107], and therefore can deal with rapid bending well.

The choice of flexure hinge characterises the main performance markers of the stage, such as stiffness, precision, load carrying capacity, and workspace. Notch-type flexure hinges are used due to their high stiffness providing accurate motion. The material stiffness provides an inherent stability to the system; their elastic nature is not susceptible to perturbations and gives rise to a predictable restoring force back to a known equilibrium. This allows for accurate control, although it is compromised by a small range of motion. However, precision is the key performance marker for the fine stage control, making notch flexure hinges the best choice. There are many possible contours of notch, as shown in Figure 81. For reference, the dimensions are specified in 82.

Each contour has a different impact on hinge properties. In this design, circular notches are used for a number of reasons. Firstly, they have the highest stiffness, making precise deflections easier to control;

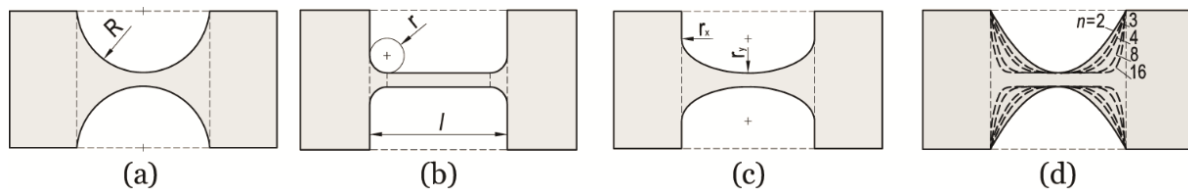


Figure 81: The shape of different types of notch hinge [108]. Each type has different motion characteristics. Circular notches are used in this design for their high stiffness, low axial shift, and manufacturing simplicity.

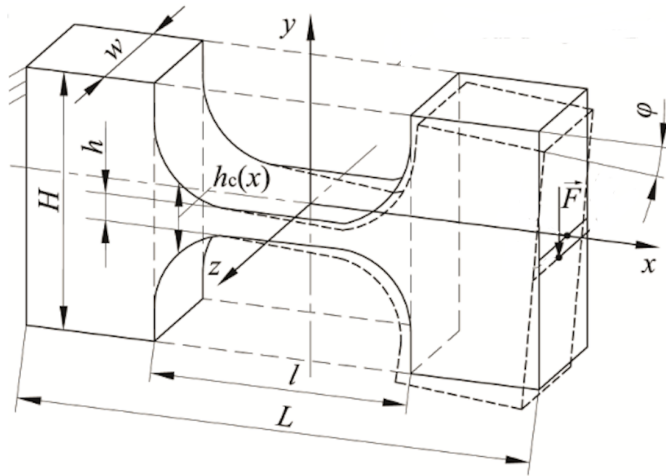
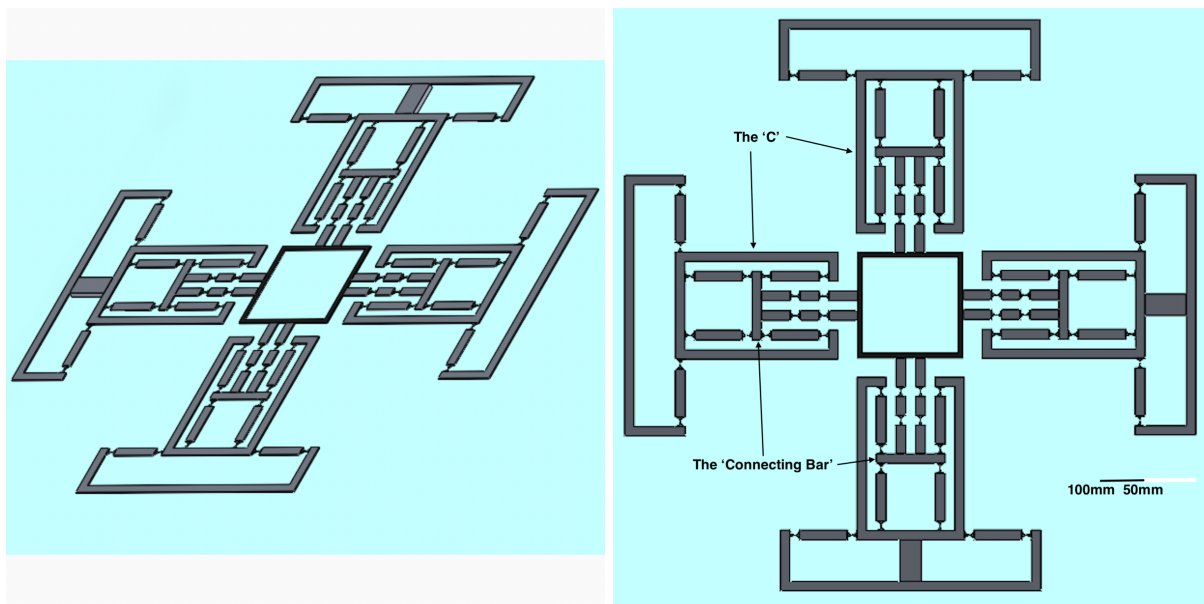


Figure 82: A circular-notched hinge with dimensions specified. These dimensions are optimised using the MATLAB model to produce the required stiffness and range of motion required by the mechanism. [108].

secondly, they have very little axis shift for a given angular deflection, facilitating motion modelling; lastly, this contour is easiest to manufacture due to its low complexity [108].

Once the hinge type is decided, the stage mechanism is designed using examples from 80 and principles inspired by [106], [109], [110].

The design (Figure 83) combines a double four-bar (Figure 80 with a double parallelogram to ensure that any force applied in a given direction is translated. Choosing these together provides the required decoupling without excessive over-design. This combination is then replicated three times and attached to each side of the (black) stage to provide stability. It can be seen that any force applied in, for example, the (in page) vertical direction by the bottom actuator will use the bottom-most and top-most hinges to shift both of vertical mechanisms and the stage. This displacement is accommodated for by the horizontal mechanisms: the central bar in each will be displaced in the direction of force application (vertically), and this combined with the flexure hinges results in a negligible displacement of the outer 'C', and therefore no unintended forces applied to the other actuator.



(a) Side angle view.

(b) Top view.

Figure 83: SolidWorks model of the final stage design. The black central platform supports the sample petri dish, with a transparent centre of $100\text{mm} \times 100\text{mm}$ and made of the same borosilicate as the base of the petri dish to ensure light can pass through unimpeded. Piezo motors are represented by boxes on two sides. The overall dimensions are 596mm in length and breadth, and the mass of the stage and mechanisms (excluding piezos) is 254.06g .

The output decoupling exploited by the design demonstrates why it is possible to treat each DOF independently when carrying out analysis: each actuator affects the stage position independently. This simplifies the analysis and demonstrates the importance of creating a new purpose-specific design.

7.4.2 Optimising Stage Design

In order to ensure the stage mechanism works as intended, two different modelling techniques are used.

Firstly, a MATLAB model is developed focusing on the deformation of each hinge in isolation [108], and combining them to simulate the behaviour of the mechanism as a whole. This identifies hinge dimensions for the desired displacement, and subsequently the optimal bar-lengths are found that allow the mechanism to deform in a way that maximises the decoupling. In order to check that the Matlab simulation correctly extrapolates the behaviour of individual hinges to the displacement of the stage as a whole, a finite element analysis (FEA) is conducted using Solidworks and the design is further refined. The output of satisfactory behaviour from both these models gives confidence that the design would work as intended if built.

The model is created using MATLAB, and formulae derived by Linß, Henning and Zentner in [108] are used to calculate the behaviour of the mechanism specified in Figure 84. Their research provides for-

Property	Bending moment	Transverse force
Bending stiffness	$\frac{M}{\varphi} = k_{M1} E \beta_w \beta_l^{(-k_{M2})} \beta_h^{(2+k_{M2})} H^3$ (9)	$\frac{F}{\varphi} = k_{F1} E \beta_w \beta_l^{(-k_{F2})} \beta_h^{(2+k_{F2})} H^2$ (10)
Maximum angular deflection	$ \varphi_{\max} = \frac{\epsilon_{\text{adm}}}{6 k_{M1}} \left(\frac{\beta_l}{\beta_h}\right)^{k_{M2}}$ (11)	$ \varphi_{\max} = \frac{\epsilon_{\text{adm}}}{12 (1-k_{\text{crit}}) k_{F1}} \left(\frac{\beta_l}{\beta_h}\right)^{k_{F2}}$ (12)
Rotational precision/axis shift	$\frac{v}{\varphi^2} = k_{vM1} \beta_l^{k_{vM2}} \beta_h^{(1-k_{vM2})} H$ (13)	$\frac{v}{\varphi} = k_{vF1} \beta_l^{k_{vF2}} \beta_h^{(2-k_{vF2})} H$ (14)

Figure 84: The table specifies the formulae used to calculate the stiffness of each hinge [108]. These are used to model the behaviour of each hinge in the MATLAB model. The β constants are calculated from the ratios between different hinge dimensions, and the k constants are determined from the analysis in [108]. φ_{\max} is the largest permissible angular deflection which is calculated from ϵ_{adm} , which is the highest admissible strain and a material property. v is the axis shift due to bending; E is Young's Modulus; F is applied transverse force; M is applied moment; and H is a hinge dimension defined in Figure 82

mulae for the calculations of bending stiffness and the maximum permissible angular deflection, among others. They also give values for the constants used in the formulae. Our model uses the stiffness of each hinge and the geometry of the bars between them to calculate the required force for a given displacement of the stage. When adjusting the design to achieve the desired stiffness, there were a number of design criteria that needed to be maintained:

- **Size of transparent gap:** must be maintained at $100mm \times 100mm$ to ensure light from imaging systems can pass through entire sample space.
- **Mechanism shape:** relative bar lengths must be maintained to allow mechanism to deform as intended.
- **Actuator space:** there must be $43mm$ between the outside, fixed part and the inner C to place the piezo motor
- **Maximum angular deflection of any hinge:** must be kept under 5° , as this is the limit to which the equations from [108] are valid. The range may have to be limited further if the calculated maximum angular deflection or admissible elastic strain are smaller than 5° , but this is the absolute upper limit.

These constraints left the following parameters as ones that could be varied to reduce the stiffness and optimise the design:

- **Depth of bars:** this affects the H dimension (shown in 82) of the hinges

- **Width of bars:** this affects the w dimension.
- **Minimum thickness of hinge:** this affects h dimension, and has greatest impact on bending stiffness of hinge.
- **Length of bars:** although the relative lengths must be maintained, they can be varied somewhat to change the moments applied to each hinge, and therefore which ones deflect more.
- **Overall size:** because the laser and imaging setup will be large (on the order of metres), the fact that the mechanism is quite large isn't an issue. However, given that it will be combined in series with a coarse control stage, reducing the mass (and therefore size) should be done if possible, but not at the expense of the performance of the fine stage.

Once the desired overall stiffness (so that the motor can displace displace the stage by $> 1mm$) is achieved, the deformation of the mechanism can be analysed. A key aspect of the mechanism function is how the central bar (CB) inside the C moves (both parts indicated on 83. Its purpose is to help decouple strain on its actuator from displacement of the stage in the perpendicular direction. To achieve this decoupling optimally, it should be displaced by half the amount that the stage moves. This requirement can be explained by considering the mechanisms that the system is based on (Figure 80 and the small angle approximations they exploit. Clearly, the larger the angular deflection of a hinge, the worse its ability to provide decoupled motion, and this relationship decays non-linearly as it is a trigonometric function. Therefore, each of the hinges involved in the decoupling should deform equally, and for this the CB has to move half as much as the stage.

A minimum energy approach is used in the MATLAB model to determine the equilibrium position of the CB when the stage is moved. The method iterates through each possible position of the bar for a stage displacement of $1mm$ (maximum that could be required) and calculates the force needed to deform all the hinges. It then sums the total force needed, and concludes that the bar will move to the position that requires the least total force. To adjust how much the bar moves, there are 2 options:

1. **Change relative hinge stiffness:** reducing the bending stiffness of the hinges attaching the CB to the C makes it easier for the CB to move with the stage.
2. **Change relative bar lengths:** changing the length of the bars inside the C compared to those connecting the CB to the stage affects how much the hinges bend respectively for a given CB displacement. Therefore, shortening the bars between the stage and CB facilitates the CB moving

with the stage.

The stiffness is changed by varying the h dimension of the hinge, as this has the greatest effect. However, if only the relative hinge stiffness is reduced ³, h has to become small to the point where the material would be too thin and delicate if produced. To avoid this, both parameters are optimised to ensure the bar moves correctly.

To find the optimum bending stiffness for the hinges connecting the CB to the C, different values of stiffness are iterated through to find the point at which it becomes energetically favourable for the CB to move. The results of varying the thickness are shown in Figure 85.

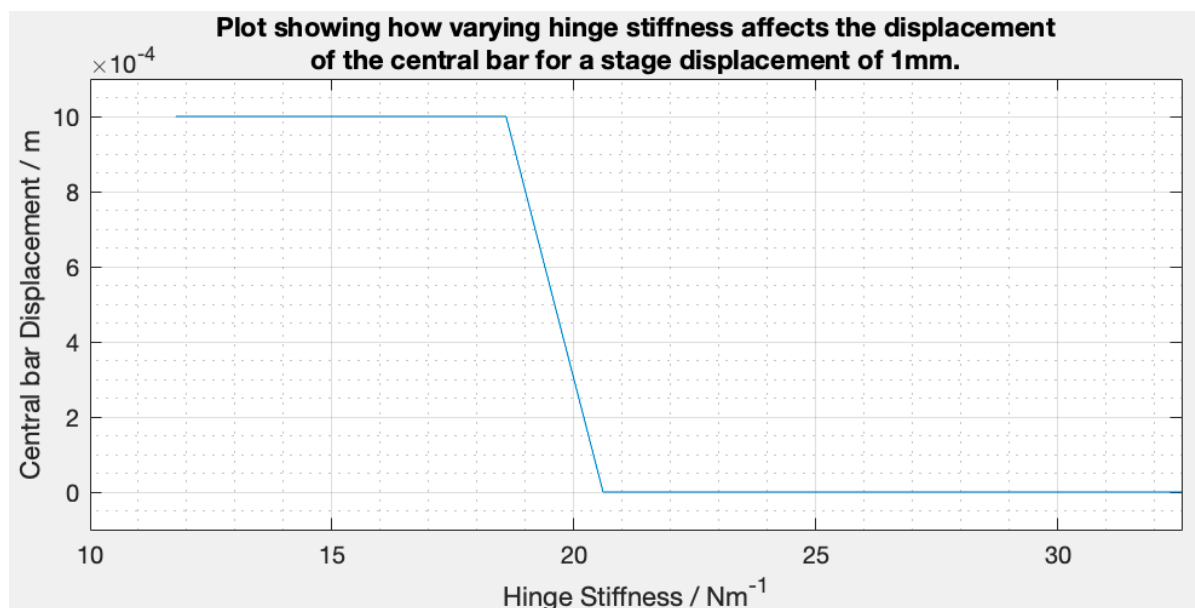


Figure 85: Plot showing how varying the stiffness (by changing the h dimension) of the hinges connecting the CB to the C affects the displacement of the CB. This is a key consideration of the system, as the mechanism must deform correctly for decoupled motion to be achieved.

Figure 85 shows the stiffness at which the CB will move with the stage, instead of remaining stationary. The switch from zero displacement to the same displacement as the stage is shown as very sharp, at about 19.5Nm^{-1} with the CB moving from one extreme of displacement to the other. This can be explained by considering the fact that the model assumes the hinges are entirely linearly elastic, and because this assumption is linear, it is always energetically favourable for the CB to move either the whole way across with the stage or not at all. It is therefore practically unfeasible to find the exact stiffness at which the CB would move halfway, as desired. However, obviously real materials are not truly linearly elastic, so the point of changeover is not as sharp as is suggested here. The deflections are

³it can't be increased as this would increase the overall stiffness of the mechanism past the capabilities of the motor

small enough that the assumption is valid for modelling the behaviour of individual hinges, but when the mechanism is considered as a whole, the assumption is too simplistic. It is likely the true behaviour will be more gradual. This idea can be tested using the Solidworks simulation, as it includes the non-linearities of material behaviour.

Once the different hinge stiffnesses have been established, the relative bar lengths can also be optimised to ensure correct deformation. These results are displayed in Figure 86.

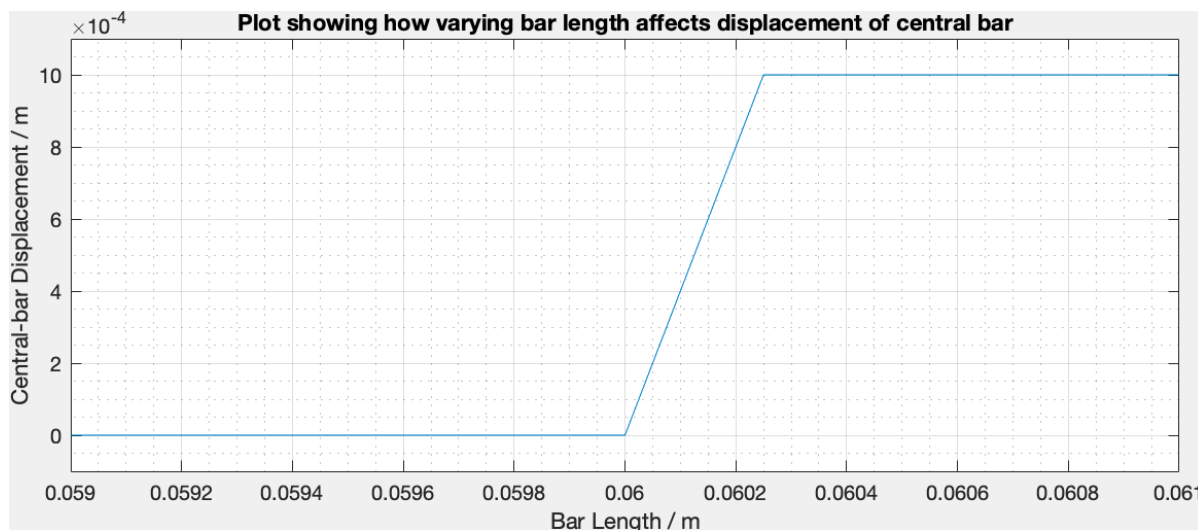


Figure 86: Plots showing how varying the length of the bars connecting the CB to the C affects the displacement of the CB and the total force needed to move the CB. The relative bar lengths determine the angular displacements required of their associated hinges, so this is optimised to ensure the hinges are all used similarly. The length at which the CB displacement switches is therefore the optimal length.

Figure 86 shows how both CB displacement and the total force required for deformation are affected by changing the length of the bars that connect the CB to the C. Again, for the same reasons discussed when varying hinge stiffness, there is a sudden point where increasing lengths causes the CB to go from zero to maximum displacement.

7.5 Finite Element (FE) Analysis of Stage Design

Section 7.4.2 makes a number of significant assumptions. These include the idea that the behaviour of one hinge in [108] can be extrapolated and applied to many hinges that make up a whole mechanism, and also the assumption that the deflection of the hinges is strictly linear elastic. To assess whether the design efforts made in section 7.4.2 were successful, a FE analysis is conducted using Solidworks. The outer parts of each of the four mechanisms are fixed, and a force of 10N is applied to the lowest edge of the C in the bottom mechanism, as shown in 87.

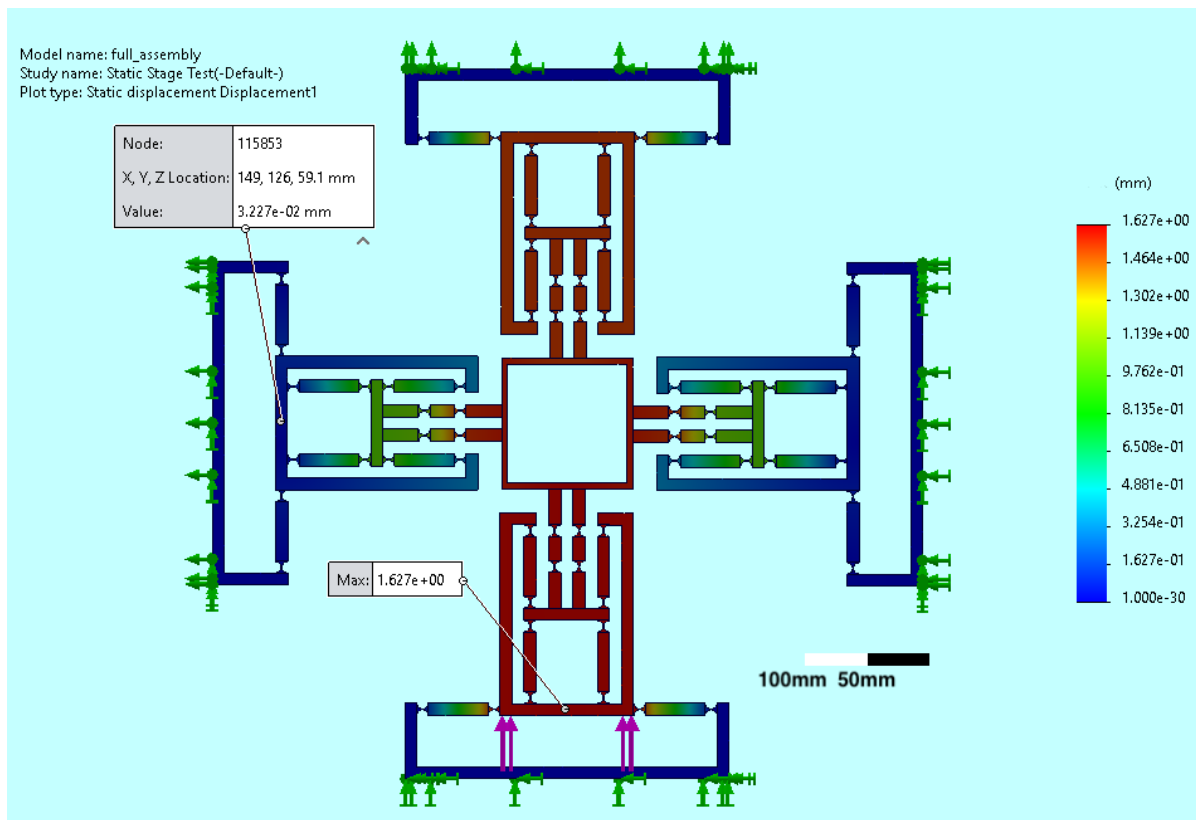


Figure 87: SolidWorks FEA model showing displacement of stage and mechanism after a 10N force is applied by piezo motor, with colour gradient representing displacement due to the force. The left-most probe shows the magnitude of the undesired displacement that will be experienced by the second piezo motor, after actuation of the first. This is less than 2% of the stage displacement demonstrating successful decoupling.

Figure 87 illustrates the deformation of the mechanism and stage under uni-axial loading. Probes on the Figure display the maximum displacement of the structure (labelled 'Max'; this is also the displacement of the stage itself), as well as the displacement at the base of the C on one of the side mechanisms (labelled 'Node: 115853'). As this is the point where the other motor would be attached, the success of the input decoupling can be assessed. Here, the displacement is less than 2% of the distance by which the stage is moved. This demonstrates that the input decoupling aspect of the design is working very well.

For the uni-axially applied force of 10N, the MATLAB model predicts a stage displacement of just over 1.2mm. This is about 25% lower than the value calculated by SolidWorks, although this discrepancy is not an issue as the limiting factor on displacement is the force provided by the piezo motor, and this can be reduced easily once the real stage is calibrated.

To identify the success of the central bar displacement optimisation, detailed in 7.4.2, a close-up image of the mechanism deformation is provided in Figure 88.

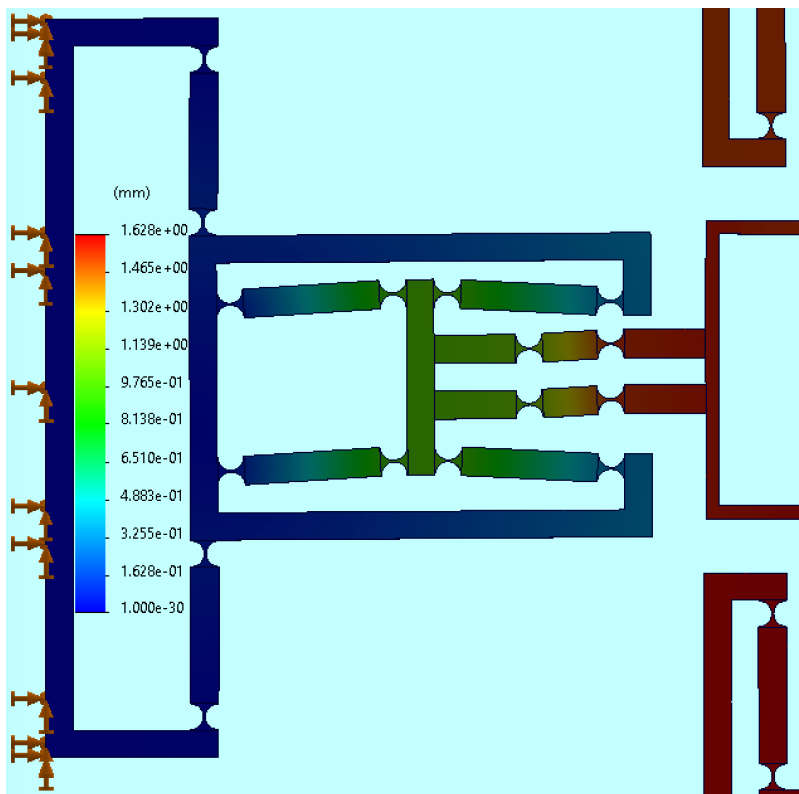


Figure 88: A zoomed-in image of the deformation shape of mechanism with $10N$ force applied. The shape is increased by a factor of 4 to display mechanism of deformation more clearly. The optimisation model developed in MATLAB designed the system such that the CB would move about half as much as the stage to ensure the decoupling is achieved, and this is shown to be successful through observation of the deformed shape and colour gradient.

To make it easier to see the displacement pattern of the mechanism, a deformation scale of four is applied. The key performance marker of the mechanism is the displacement of the central bar, which was designed to move about half as far as the stage in order to achieve successful decoupling. Visually, it is clear from the colour scale that the bar has moved as intended. This confirms that the MATLAB model of perfectly elastic hinges is an oversimplification, but combining it with intuition of how materials really behave provides a good predictor of the SolidWorks simulation. Although the SolidWorks is more accurate, the MATLAB model is much more efficient at optimising dimensions, as each simulation is fast to run and many combinations can be tested quickly, so it is worth using the MATLAB model first.

An area in which the models agree well is proximity to failure. The MATLAB model calculates the largest admissible angle of deflection as 3.07° , and for a stage displacement of $1.6mm$ the largest angular deflection is 1.53° , giving a safety factor of two. Similarly, SolidWorks calculates the highest stress as $307MNm^{-2}$, as shown in Figure 89, with the yield strength being $505MNm^{-2}$ hence giving a safety factor of 1.65. It is worth noting that these values are calculated based on the displacement resulting from

a $10N$ force applied by the piezo motor. This is the maximum force it is capable of and gives a stage displacement of $1.6mm$, whereas the mechanism is only intended to provide $1mm$ of stage motion in any direction, so during operation the highest stress will be much lower, and therefore further away from failure.

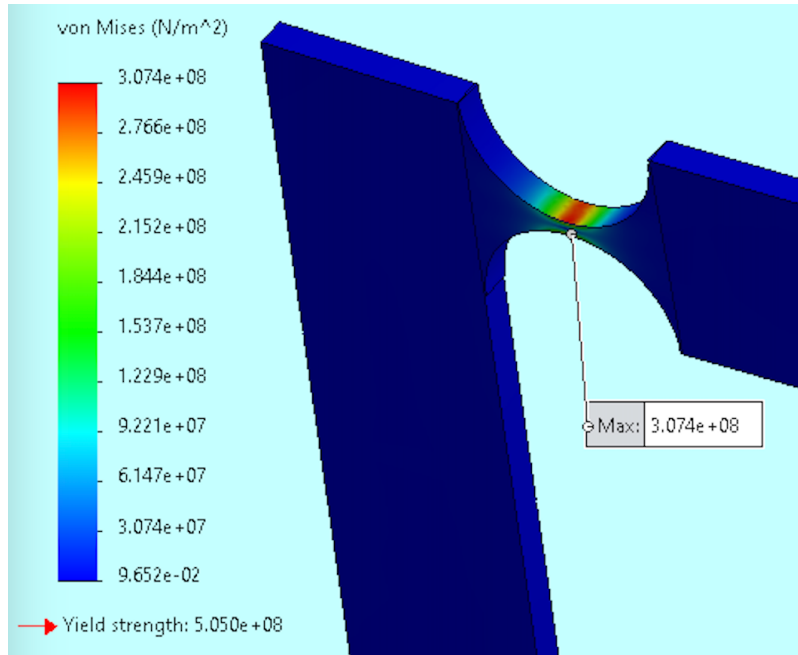


Figure 89: Close-up image of hinge stress distribution. The hinge displayed is one of the side hinges, connecting the C to the base. These have the greatest bending deflection, so the highest stress is found here. There is a safety factor of 1.6 at the peak stress.

7.6 XY Controller Design

In order to determine where the stage needs to be moved to, the position sensors measure the displacement of the stage from a known, calibrated zero, and compares this to the coordinates of the cells provided by the imaging system. The distance between the current and desired position is then calculated, and a signal is sent to the actuators to move the stage to the correct position.

For this process to occur smoothly and efficiently, a controller is designed which acts on the closed loop feedback. A model of the motor and stage is developed, from which a transfer function (TF) is derived to represent the dynamics of the system. Because of the successful decoupling of motion directions, all the modelling analysis can be conducted by only considering motion in one direction. The results can then be used with both motors to achieve the desired 2-DOF. Once the TF is found, a PID controller can be designed to ensure that the quick response time required, $< 60ms$, is achieved with minimal disturbance to the sample. Therefore, overshoot and oscillation should not be present in a step response.

Process and measurement noise are inevitable in any real world system, so these are added to the model to check its robustness. In order to deal with these effectively, a Kalman filter is designed, using an estimator to help reject the noise. This is then combined with the PID controller to give a satisfactory response to inputs, whilst also being robust to a noisy system.

7.6.1 Motor Model

The model of the motor is based on the Crossfixx™ piezo motor function described by Xeryon [111]. The analysis is inspired by [112], which goes into great detail about the functioning of different types of piezo motors, and [113], which discusses a walking piezo motor, similar in function to the one made by Xeryon.

Inside the motor, the piezo electric effect is actually exploited in reverse: an electric signal is applied to a piezo-electric material, which then deforms. This process is shown in Figure 90.

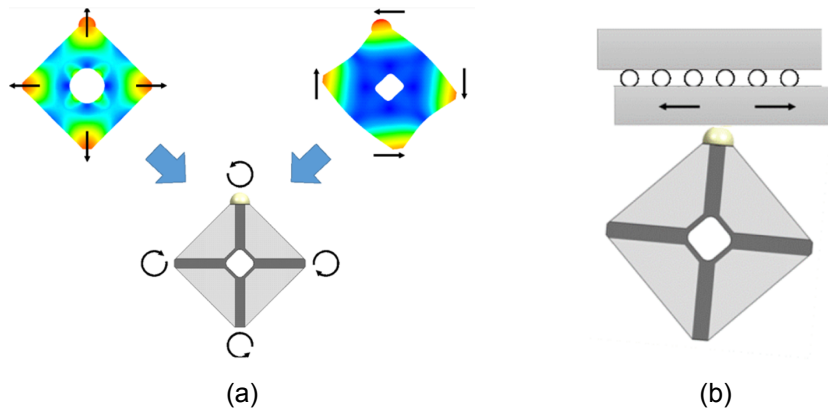


Figure 90: Figures show how different excitations of the piezo ceramic combine to move its tip and produce motion of the stage. (a) The combination of the expansion and bending modes are combined to produce rotational movement in the tip of the piezo ceramic, picture is from [111] (b) The component of the tip's motion parallel to the stage drags the stage with it, moving the stage in many small steps. The size and frequency of these steps can be controlled by changing the frequency and amplitude of the sinusoidal inputs.

The motor is divided up into four quadrants, each of which is an electrode. Electrodes diagonal to each other form motor phases, and excitation of each motor phase independently exploits the two resonant modes of the motor. The first mode is shown in the top left of Figure 90a, and produces a uniform radial expansion of the piezo-ceramic which results in the contact point moving perpendicular to the actuation bar. The second mode is shown in the top right of Figure 90a and is characterised by in-plane bending, causing the contact point to move parallel to the actuation bar. Combining both modes together allows for control of the tip in both directions. By applying sinusoidal excitations with different phase differences to each motor phase, different types of motion can be achieved. Exciting all four quadrants with the same signal induces the expansion mode, whereas using sinusoids that are

180° out of phase excites the bending mode. Most useful, however, is when the signals are applied 90° out of phase, as this produces elliptical motion, which is what is used during operation to move the bar. Varying the amplitude and phase difference of each signal allows the shape and size of the ellipse to be controlled. This in turns provides control over the driving force and speed of the motor. The motor can operate silently, as its resonant frequency is 166kHz, well above the audible limit for humans. This frequency is also high enough that it is significantly above the cutoff frequency of most mechanical systems, so that any disturbance to them is negligible.

7.6.2 Dynamic Model

Because of the elliptical motion of the contact point, the actuator effectively moves in many small steps. This is similar in concept to the 'walking piezomotors' described in [113], and forms the basis for the dynamic model.

Firstly, define the sinusoidal inputs as

$$u_1(t) = A \sin(\alpha(t))$$

and

$$u_2(t) = A \sin(\alpha(t) + \frac{\pi}{2})$$

where $u_1(t)$ and $u_2(t)$ are the inputs to each motor phase, and $\alpha(t)$ is the angle of the waveform. This is defined as

$$\alpha(t) = 2\pi \int_0^t f(\tau) d\tau$$

and takes into account all the past variations in frequency in order to calculate the current angle.

Because each full loop of the contact tip results in a 'step' of the actuator rod, the angular of the sinusoidal input is directly proportional to the velocity of the stage⁴. This also implies that the position of the tip can be modelled as

$$x_p(t) = \frac{c}{2\pi} \alpha(t) = c \int_0^t f(\tau) d\tau$$

, where c is a motor constant, representing a gain factor from the driving frequency to the position of the tip. Therefore, the velocity and, thus the position of the stage, are determined by controlling the angular velocity through the frequency of the waveforms. Applying a Laplace Transform to this relationship (assuming zero initial conditions) yields

⁴each step is so small and the frequencies are so high that the discrete nature of this can be well approximated by assuming the velocity is a continuous function

$$X_p(s) = c \frac{1}{s} F(s) \quad (100)$$

In order to determine how the position of the tip of the piezoceramic x_p is related to the position of the stage, a spring-damper system is used to model their interaction. Figure 91 shows the model used by Merry et al., with the obvious difference that their motor uses walking legs whereas ours has a single piece of piezoceramic material.

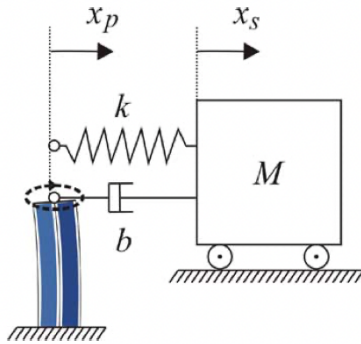


Figure 91: The mass-spring-damper stage model used to derive motion model is shown [113].

Using this model, a transfer function between the position of the stage x_s and the tip x_p is found. Firstly, the equation of motion for the spring, damper and stage mass is found:

$$M \ddot{x}_s(t) = k(x_p(t) - x_s(t)) + b(\dot{x}_p(t) - \dot{x}_s(t)) \quad (101)$$

M is the mass of the stage, and k and b are the spring and damping constants respectively. Because we are unable to build a physical model of the system, the constants for our model cannot be empirically determined, as is done in [113]. Instead, the values from [113] are used to allow calculations to be done, although these won't actually be accurate to our specific stage. Taking the Laplace Transform gives

$$s^2 M X_s(s) = k(X_p(s) - X_s(s)) + b(s X_p(s) - s X_s(s)) \quad (102)$$

Which can be rearranged to

$$\frac{X_s(s)}{X_p(s)} = \frac{bs + k}{Ms^2 + bs + k} \quad (103)$$

Equation 103 gives the TF from the piezoceramic tip position to the stage position. The TF relating input signal frequency and tip position has already been determined in Equation 100, and combining these produces

$$\frac{X_s(s)}{X_p(s)} = \frac{X_s(s)}{c_s^{\frac{1}{2}} F(s)} \quad (104)$$

and therefore

$$\frac{X_s(s)}{F(s)} = \frac{cbs + kc}{Ms^3 + bs^2 + ks} \quad (105)$$

which is the TF relating stage position and frequency. This can then be used with a controller to produce the desired response.

7.6.3 PID Controller

A controller is designed based on the TF derived in Section 7.6.2. A PID model is used. The gains are optimised using the Ziegler-Nichols method [114], which considers the affect of each gain value separately before adding a new one to the model, and the Simulink model in Figure 92 is achieved.

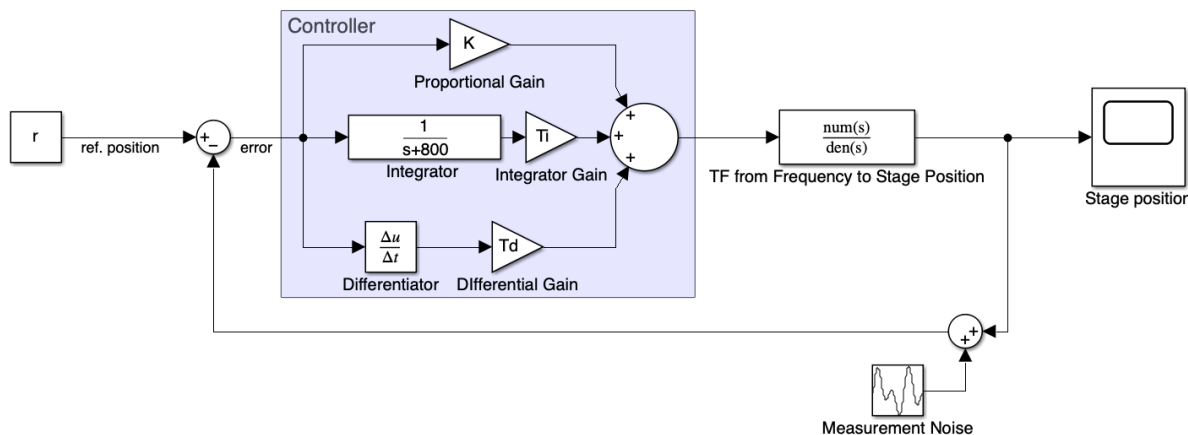


Figure 92: The PID controller, developed using the Ziegler-Nichols method, is modelled using Simulink, and is displayed here. A reference value is input, and this is passed to the controller and then through the TF of the system. Negative feedback is implemented to complete the loop.

Figure 93 shows the response to a step input with the noise powers set to zero. The reference position is set to 1mm, as this is the largest displacement that the system is designed to make. It takes less than 40ms to reach the desired position, and the response can be seen to be smooth and without oscillation or overshoot, as required. However, the real system will be affected measurement noise (and process

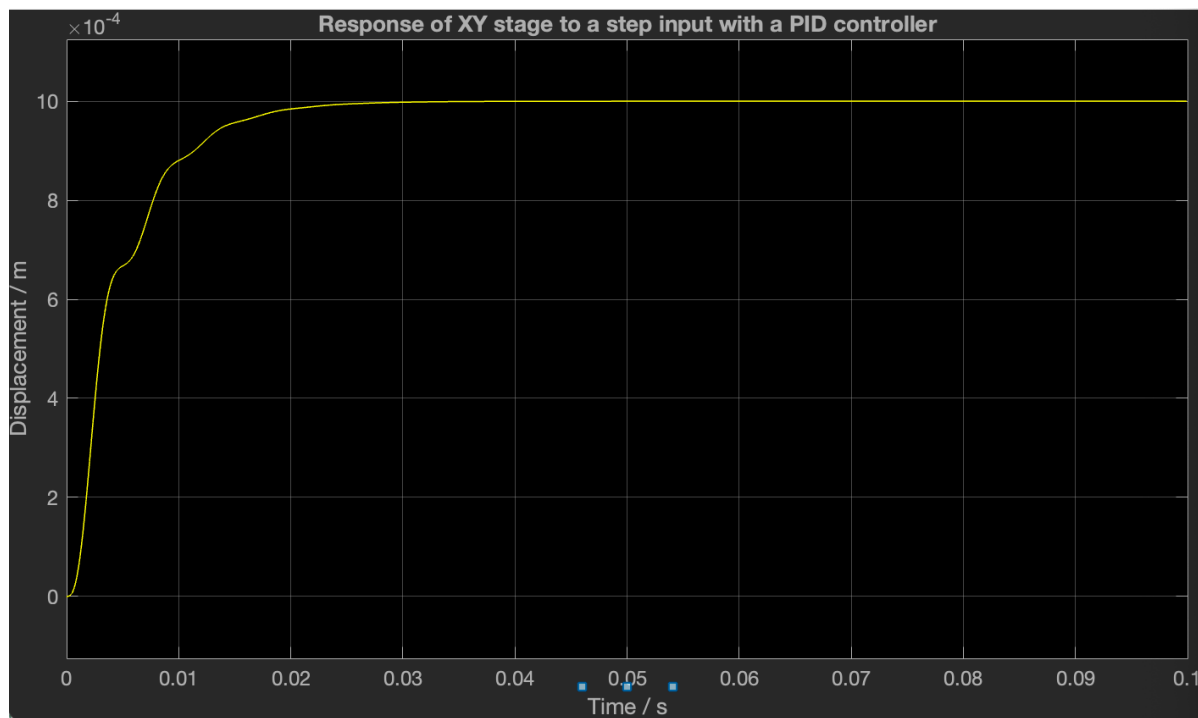


Figure 93: Closed loop response of stage position with the PID controller to a step input of 1mm, with no added noise. Settling within 30ms, this is well below the target of 60ms and is reached with very little oscillation and overshoot, minimising disruption of the sample.

noise in the estimator), as discussed in Section 7.6.4, so these need to be added to the model to ensure it is robust and to check it will provide sufficient stability in a real system.

7.6.4 Noise Modeling

Measurement noise represents the uncertainty in any measurement of the real system, and is expressed as random perturbations in the signal provided by the measurement device.

Process noise on the other hand is used to account for the uncertainties in motion in an estimation system, such as the Kalman filter used in Section 7.6.5. This is the result of unknown external forces affecting target motion, which makes exact prediction impossible.

In order to model the noise signals in Simulink, we need to convert manufacturers' data to noise powers. For zero-mean, white Gaussian noise, the signal's variance is equal to its noise power⁵. The resolution of Lion Precision's capacitive sensor [105] is specified as a root-mean-squared (RMS) value. Therefore, a relationship is found between the RMS and variance of the sensors noise signal: first, consider the

⁵These assumptions are valid because of the time invariance of the noise signal, and that it will be equally distributed over all frequencies.

definition of variance for a random variable

$$\sigma^2 = E[(X - \mu)^2]$$

Assuming zero-mean noise, this simplifies to

$$\sigma^2 = E[X^2]$$

Given that $E[X^2]$ is the expectation of the squares, the RMS value of a signal can be written as

$$RMS = \sqrt{E[X^2]} = \sqrt{\sigma^2} = \sigma \quad (106)$$

and therefore

$$N_0 = \sigma^2 = RMS^2 \quad (107)$$

For the capacitive sensor with RMS resolution of 26nm at 10kHz , this gives $N_0 = (26 \times 10^{-9})^2 = 6.76 \times 10^{-16}$.

Xeryon provides a resolution value of $\pm 312\text{nm}$ for their piezo motor. Without the ability to test the product ourselves to gain a better insight, the assumption is made that this is the upper limit on the resolution, and therefore almost all variation caused by noise is within this range. Because the noise is Gaussian, 99.73% of the values will be within 3σ of the mean. This implies that $3\sigma = 312\text{nm}$, so $\sigma = 104\text{nm}$ and $N_0 = \sigma^2 = 1.08 \times 10^{-14}$

The measurement noise signal is added into the Simulink model, and the results are examined again. On a large scale, the trace looks the same as 93, because the noise is relatively small. However, after zooming to look more closely in Figure , the noise has caused the response to be much less stable, with the stage position varying up to $\pm 2\mu\text{m}$. This is about the size of the particles that we are trying to tweeze, and therefore an unacceptable level of instability. In order to rectify this, a Kalman filter is designed to reject noise and increase the stability of the stage.

In the Kalman filter analysis, these noise signals are required in matrix form. The autocorrelations of each signal are defined as

$$R_w(\tau) = E[w(t)w(t + \tau)^T]$$

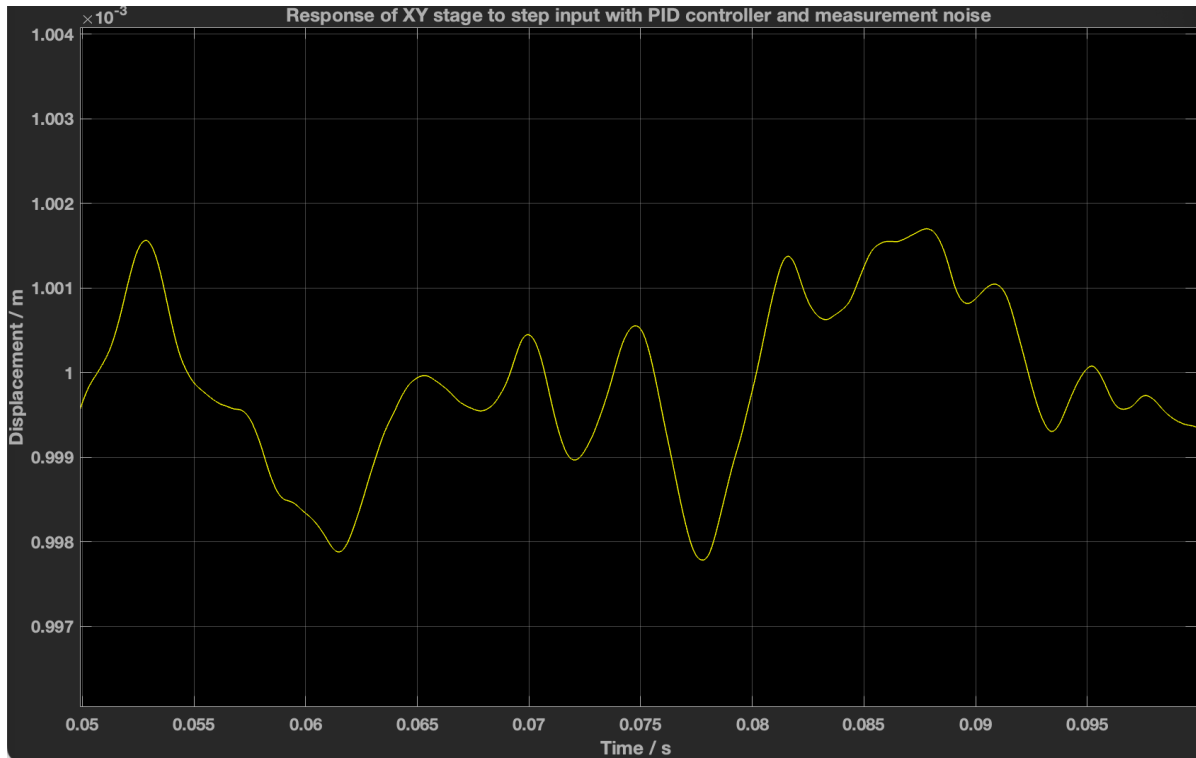


Figure 94: Closed loop response of stage position with the PID controller to a step input, with a measurement noise signal added. On the millimetre scale, the plot looks the same as 93, but zooming in reveals the effects of the noise on the stability of the system, once it has reached steady state. Micrometre variations in position would result in failed ablation of the cell membrane: the hole size is designed to be $3\mu\text{m}$ in diameter, so the cell must move significantly less than this. A Kalman filter is used to achieve this increased stability via better noise rejection.

and

$$R_v(\tau) = E[v(t)v(t + \tau)^T]$$

If the noise is stationary, zero-mean, Gaussian and white, as is assumed here, then the autocorrelation can be written as

$$E[w(t)w(t + \tau)^T] = R\delta(\tau)$$

where R is the covariance matrix for measurement noise, and the equivalent for state noise

$$E[v(t)v(t + \tau)^T] = Q\delta(\tau)$$

, where Q is the covariance matrix for the state noise. Because the autocorrelation of a signal is also equal to half its noise power, the covariance matrices can then be found.

7.6.5 Kalman Filter

A Kalman filter is an algorithm that is used to estimate and predict the state of a system, based on estimations from the previous time step and measurements from the current one. They use the combination to optimise the state estimation when noisy measurements are involved, as is the case here. This is then combined with the PID controller, similarly to [101], which tries to drive the estimation to a reference state to provide much more robust control. Process noise is used to model the uncertainty in the state resulting from the piezo motor, and is added to the model.

In order to implement a Kalman filter, the system is put into state space form. Equation 105 can be transformed back into the time domain as:

$$M \ddot{x}(t) + b\ddot{x}(t) + k\dot{x}(t) = bc\dot{f}(t) + ckf(t) \quad (108)$$

where the variables and constants are the same as in Section 7.6.2. This is then put into state space form:

$$\frac{d}{dt} \begin{bmatrix} x(t) \\ \dot{x}(t) \\ \ddot{x}(t) \end{bmatrix} = \underbrace{\begin{bmatrix} 0 & 1 & 0 \\ 0 & 0 & 1 \\ 0 & \frac{-k}{m} & \frac{-b}{m} \end{bmatrix}}_A \begin{bmatrix} x(t) \\ \dot{x}(t) \\ \ddot{x}(t) \end{bmatrix} + \underbrace{\begin{bmatrix} 0 & 0 & 0 \\ 0 & 0 & 0 \\ \frac{ck}{m} & \frac{bc}{m} & 0 \end{bmatrix}}_B \begin{bmatrix} c\dot{f}(t) \\ ckf(t) \\ 0 \end{bmatrix} \quad (109)$$

Adding in noise signals:

$$\dot{x}(t) = Ax(t) + Bf(t) + v(t) \quad (110)$$

$$y(t) = \underbrace{\begin{bmatrix} 1 & 0 & 0 \\ 0 & 0 & 0 \\ 0 & 0 & 0 \end{bmatrix}}_C + w(t)$$

Where $v(t)$ is the process noise, and $w(t)$ is the measurement noise. $y(t)$ is the output signal and is simply the state with measurement noise added.

The key to a Kalman filter's function is the observer, which provides the estimation step of the algorithm.

This is implemented using the observer gain matrix, $L(t)$. The Kalman filter for this system is therefore

$$\dot{\hat{x}}(t) = A\hat{x}(t) + Bf(t) + L(t)[y(t) - \hat{y}(t)] \quad (111)$$

$$\hat{y}(t) = C\hat{x}(t)$$

where variables with a 'hat' on indicate estimations from the observer. The observer matrix is calculated using the solution to the Riccati equation $P(t)$

$$\dot{P}(t) = AP(t) + P(t)A^T + Q - P(t) \quad (112)$$

The observer gain matrix is then found from

$$L(t) = P(t)C^T R^{-1} \quad (113)$$

Equations 110 111 are input to Simulink, and the full system, with PID controller, is shown in Figure 95.

Because we only want to control the position of the stage, the selecting block is used to isolate only the first element of the state vector, and this is what is input to the PID controller. The output is displayed in Figure 96. The trace can be seen to be much more stable, with the position not vary by more than a few 10s of nanometers. This demonstrates that the Kalman filter is performing as desired, and the system is now suitably robust to noise signals, as this stability is well within the requirements.

7.7 Z Control

The Z-axis control of the system ensures the focus of the laser is in the correct position on the cell. This is necessary as the particles to be tweezed are suspended in solution, and although the cells are attached to the bottom of the petri dish, their depth is not negligible and has to be accounted for. Furthermore, the tweezing system can only move microparticles in the XY plane, but the ablation laser punctures the cell membrane from above. Therefore, in order to place the particles into the cell, the focal point of the optical trap (Section 2.1.1) itself must be moved in the Z-direction. This is achieved by controlling the objective lens itself with a separate motor, meaning the stage stays in the same plane throughout operation. However, detailed analysis of this aspect of control is not within the scope of this project. An overview of its function is provided here.

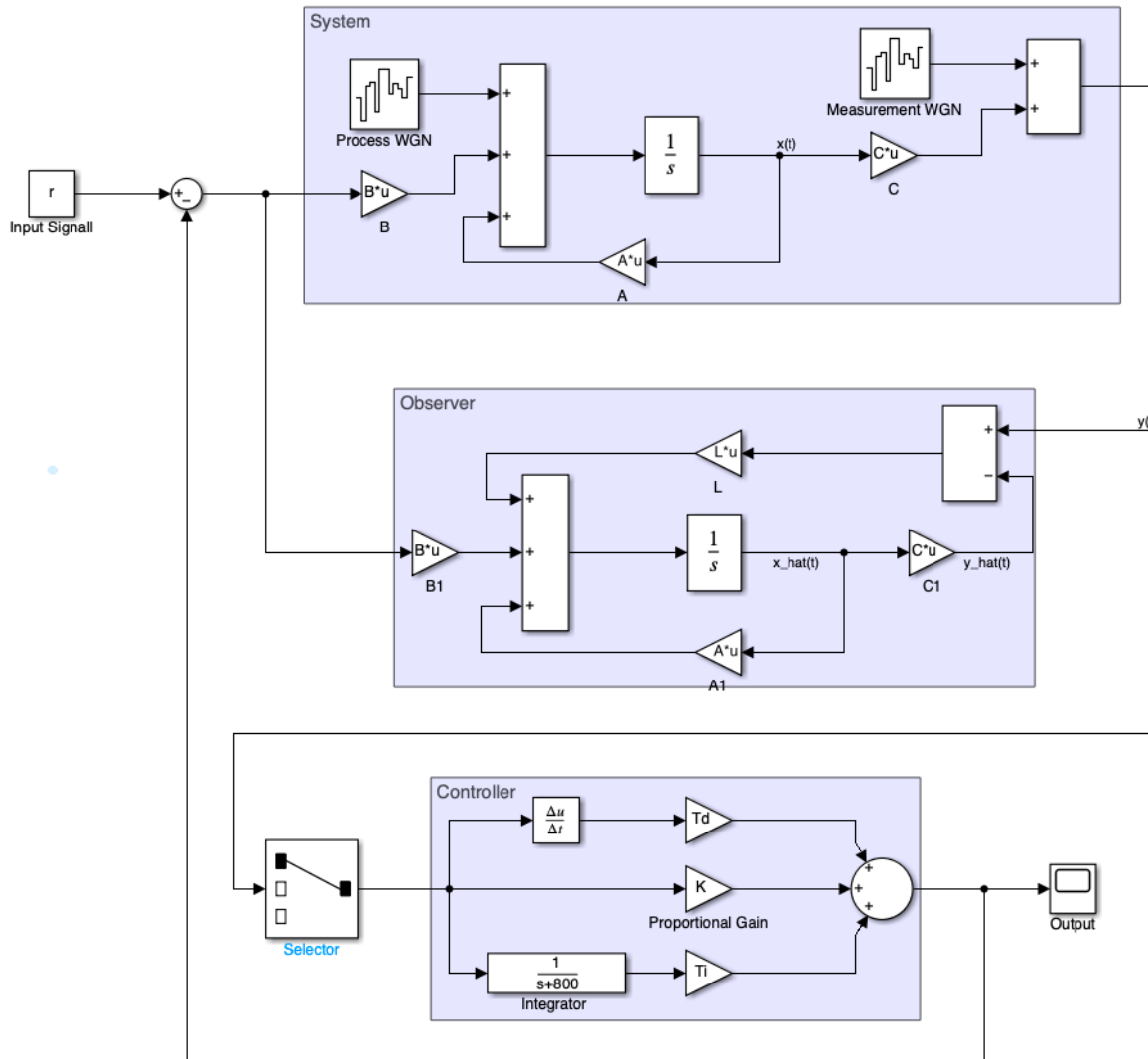


Figure 95: Simulink realisation of the Kalman filer, combined with the PID controller to provide feedback on the position state of the stage. The observer produces an estimate of the state and is combined with the measured state to provide an output that is more robust to noise.

One of the most important considerations for controlling the objective lens is making sure to conserve its numerical aperture (NA). Due to the requirements of the optical tweezing system described in Section 2.1.3, we are using a lens with an NA of 1.1, which is significant as it is higher than the NA of air. Therefore, the laser cannot pass through air after exiting the objective lens. A straightforward solution would be to immerse the lens directly into the liquid containing the cells, however doing this would result in complex fluid dynamics around the lens as it moved through the solution, making it very difficult to predict the motion of the particles. To account for this, a cover slip is placed over the cell sample to hold them in place as the lens moves, and a liquid layer is added on top of the cover slip. This allows the lens to be placed into liquid without disturbing the sample. Commonly used liquids for immersion lenses are

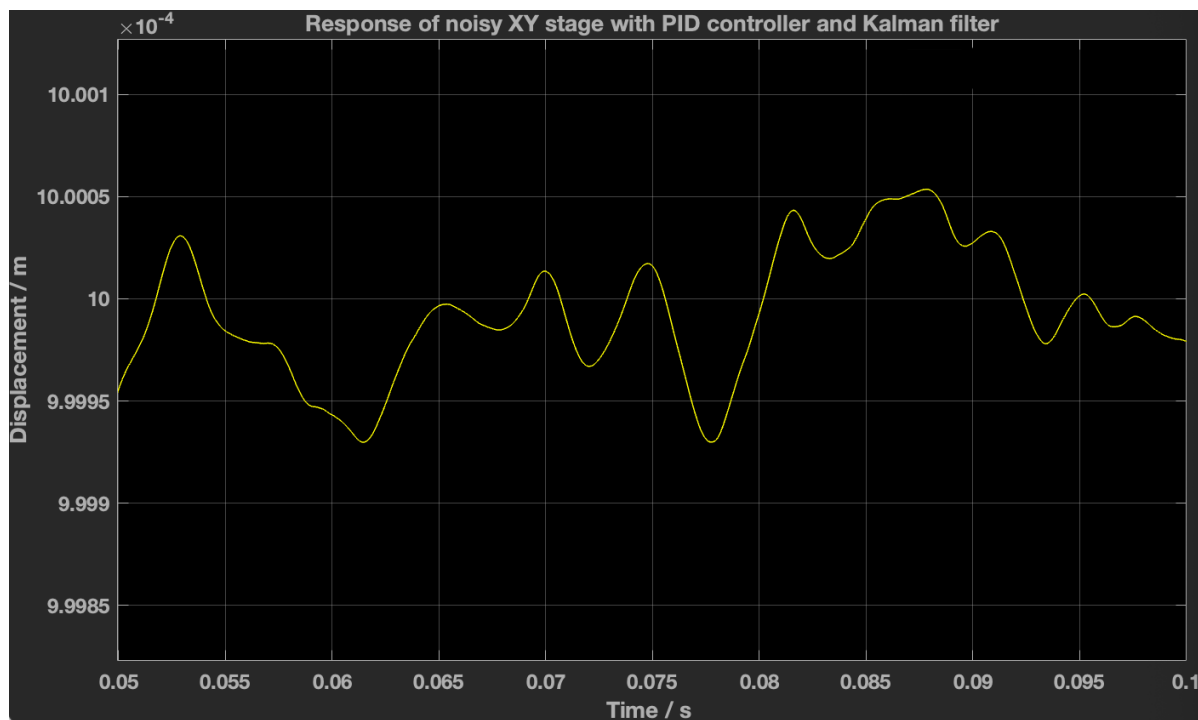


Figure 96: Response of Kalman filter combined with PID controller to the same step input as previously, but the position variation is now a few 10s of nanometres. Therefore the laser focus will be maintained on the cell.

water and oil, as they have appropriate NAs. However, the Ramen spectrum of oil is very similar to the spectrum of the cells that we want to observe, so using oil as the immersion would ruin the function of the chemical imaging system. Therefore water is used as the immersion fluid.

The necessary specifications for the z-control are limited by the tweezing process and discussed in Section 3.5, but are summarised here: the system needs a minimum range of $50\mu\text{m}$ at a minimum speed of $200\mu\text{ms}^{-1}$, but ideally closer to $1000\mu\text{ms}^{-1}$. It also needs a stability of $< 100\text{nm}$ in order to ensure the particles stay within the optical trap. A multi-criteria analysis (MCA) of some industry options for micro-motors is shown in Table 12 to inform the decision on the best choice. Resolution and range are both weighted the highest as they are requirements of the motor from other parts of the project. Cost and settling time are both important to consider, but can be compromised on so have lower weightings. Through the use of the MCA, Dover Motion's DOF-5 is selected for the z-control as it has the highest combined score. It performs similarly well to the others in resolution (5nm), range (5mm) and settling time (15ms), but has the distinguishing advantage of significantly lower cost.

Z-motion Stage	Motor Type (N/A)	Resolution (35%)	Range (35%)	Settling Time (10%)	Cost (20%)	Total
Dover Motion (DOF-5)	Linear servo	9	10	7	6	8.55
PI V-308	Voice coil	9	10	7	3	7.95
PI ND72Z2LAQ	Piezo ceramic	10	8	6	2	7.3
MS nPFocus10	Piezo	8	5	8	3	5.95

Table 12: MCA of different Z-control stages. Each stage is rated on a scale from 1 – 10 for each specification. Weightings are applied based on importance of criterion and the stage with highest total score is chosen.

Component	Quantity	Price (£)
Xeryon XLA-10-55-312	1	500
LionPrecision CPL590	1	100
LinMot PS01	1	2400
DoverMotion DOF-5	1	5000
Keysight 10715A	1	800
Control system total price: £16,450		

Table 13: Costs of each component in control section.

7.8 Control Costs

An estimation of the total cost of the main components is provided in Table 13. Prices for individual components weren't always available, even after quote enquiries to the manufacturer, so in these cases best guesses were used based on the information available.

7.9 Control System Summary

In summary, the control system combines a dual-stage XY positioning system, made up of coarse and fine stages, with an objective lens that has Z motion capabilities. A novel fine stage mechanism design provides decoupled input and output motion, which not only avoids any unintended and potentially damaging loads being placed on the actuators, but also allows the motion in each direction to be considered independently, therefore greatly simplifying the dynamics of the system. Without complicated coupled equations of motion, a transfer function for the system can be developed, and a PID controller is optimised and applied to produce quick and stable responses. System noise is dealt with by a Kalman filter, providing sufficient stability for the cells in the laser focal region. Overall, the system achieves a spatial resolution of 312nm over a range of $100 \times 100\text{mm}$ in both the X and Y directions, with a repositioning time of $< 30\text{ms}$ when responding to a step input. These abilities allow it to precisely and rapidly reach every cell in a sample.

8 Conclusion - Xianming Liu

The photonics fabrication and imaging platform we have developed costs £206,194 and is a comprehensive solution for single cell surgery. Unlike many previous systems, our platform integrates all essential functionalities into a single, cohesive unit. The platform is designed to perform laser ablation on the target cell, and then optically tweeze drug-coated microparticles into the cell. The entire process takes 718ms per cell and is continuously monitored and studied using the widefield microscopy and chemical imaging system. This conclusion summarizes the key features of our platform.

The optical tweezing system is designed to capture and precisely manipulate multiple microparticles at once. The system utilizes a 975nm continuous wave laser for maximum trapping force while minimizing photodamage. The optical traps generated are able to confine the microparticle within a radius of less than 100nm, even in the presence of Brownian motion. One key feature of the optical tweezing system is the use of a spatial light modulator. This setup enables simultaneous and dynamic manipulation of up to 9 particles. The tweezing system is able to reach a speed of $190 \mu\text{m/s}$ in the x-y plane, ensuring that multiple microparticles can be quickly inserted into target cells, and hence greatly increasing the efficiency of our platform.

The laser ablation system uses a femtosecond pulsed laser to ablate a $3 \mu\text{m}$ diameter pore in cell membranes. The femtosecond pulsed laser allows for multiphoton absorption processes to take place, minimizing collateral damage and increasing cell viability. The use of a Bessel beam profile, achieved through an axicon, ensures that the laser maintains a tight focus over a longer axial range, therefore maximizing ablation success rate. Moreover, the system's versatility extends to potential applications beyond membrane ablation, such as intracellular dissection and chromosome ablation.

The widefield imaging system provides crucial data input to other systems: microparticle position data for the dynamic optical tweezing, and cell position data for membrane ablating. The system utilizes phase contrast microscopy to localize the cells and microparticles. The widefield imaging system has a field of view of $180\mu\text{m}$ by $180 \mu\text{m}$, and resolution of 305nm. The system also integrates several image processing algorithms to robustly locate cells and microparticles for tweezing control.

The chemical imaging system is used to verify the successful delivery of the microparticle and the subsequent drug-uptake process. The system utilizes higher-order Coherent Anti-stokes Raman Scattering microscopy for chemical discriminant imaging capability. The system's performance is greatly increased

at minimum cost by sharing the same femtosecond pulsed laser between the chemical imaging system and laser ablation system. Overall, the system has a resolution of 316nm with a scanning area of $200\mu m$ by $200\mu m$. The hyperspectral imaging capability allows the system to discriminate between different drug particles and types of cells. Thus, this gives the platform the ability to simultaneously operate with multiple different drugs cells.

The mechanical stage, shared by all the systems in our platform, controls the position of the transparent petri dish containing the sample. It offers coarse control covering an area up to $100mm$ by $100mm$, allowing the use of various sample dish sizes. Through the use of innovative flexure hinges, the XY motions are entirely decoupled. By using a PID controller combined with a Kalman Filter, the fine control provides a precision on the order of one hundredth of a nanometre.

In conclusion, the advanced photonics platform represents a significant leap forward in the field of single cell surgery and imaging. By combining cutting-edge optical tweezing, laser ablation, and imaging technologies into a single, cohesive system, the platform opens new avenues for research and treatment in the field of biomedical sciences. The work presented in this report lays a solid foundation for future innovations and applications in cancer cell research, genetic engineering, and much more.

References

- [1] Shuxun Chen, Jinping Cheng, Chi-Wing Kong, Xiaolin Wang, Shuk Han Cheng, Ronald A. Li, and Dong Sun. Laser-induced fusion of human embryonic stem cells with optical tweezers. *Applied Physics Letters*, 103, 7 2013.
- [2] Adnan Shakoor, Bin Wang, Lei Fan, Lingchi Kong, Wendi Gao, Jiayu Sun, Kwan Man, Gang Li, and Dong Sun. Automated optical tweezers manipulation to transfer mitochondria from fetal to adult mscs to improve antiaging gene expressions. *Small*, 17, 9 2021.
- [3] Aisada Uchugonova. Nanosurgery of cells and chromosomes using near-infrared twelve-femtosecond laser pulses. *Journal of Biomedical Optics*, 17:101502, 5 2012.
- [4] Giuseppe Pesce, Philip H. Jones, Onofrio M. Maragò, and Giovanni Volpe. Optical tweezers: theory and practice. *The European Physical Journal Plus*, 135:949, 12 2020.
- [5] Keir C. Neuman and Steven M. Block. Optical trapping. *Review of Scientific Instruments*, 75:2787–2809, 9 2004.
- [6] N Malagnino, G Pesce, A Sasso, and E Arimondo. Measurements of trapping efficiency and stiffness in optical tweezers. *Optics Communications*, 214:15–24, 12 2002.
- [7] Alexander Rice and Robert Fischer. Calibration of optical tweezers.
- [8] Mark Williams. Optical tweezers: Measuring piconewton forces. 2002.
- [9] Hu Zhang and Kuo-Kang Liu. Optical tweezers for single cells. *Journal of The Royal Society Interface*, 5:671–690, 7 2008.
- [10] Phillip Jones H and Onofrio Marago M. *Optical Tweezers: Principles and Applications*. Cambridge University Press, 2015.
- [11] Agnese Callegari, Mite Mijalkov, A. Burak Gököz, and Giovanni Volpe. Computational toolbox for optical tweezers in geometrical optics. *Journal of the Optical Society of America B*, 32:B11, 5 2015.
- [12] Van Thuy Hoang, Grzegorz Stępniewski, Karolina H. Czarnecka, Rafał Kasztelanic, Van Cao Long, Khoa Dinh Xuan, Liyang Shao, Mateusz Śmiertana, and Ryszard Buczyński. Optical properties of buffers and cell culture media for optofluidic and sensing applications. *Applied Sciences*, 9:1145, 3 2019.

- [13] Arthur Ashkin. Forces of a single-beam gradient laser trap on a dielectric sphere in the ray optics regime. *Biophysical journal*, 61(2):569–582, 1992.
- [14] Meng Bing-Huan, Zhou Jin-Hua, Zhong Min-Cheng, Li Yin-Mei, Wu Jian-Guang, and Ren Hong-Liang. Improvement of transverse trapping efficiency of optical tweezers. *Chinese Physics Letters*, 25:2300–2302, 6 2008.
- [15] E Martín-Badosa, M Montes-Usategui, A Carnicer, J Andilla, E Pleguezuelos, and I Juvells. Design strategies for optimizing holographic optical tweezers set-ups. *Journal of Optics A: Pure and Applied Optics*, 9:S267–S277, 8 2007.
- [16] N. B. Simpson, D. McGloin, K. Dholakia, L. Allen, and M. J. Padgett. Optical tweezers with increased axial trapping efficiency. *Journal of Modern Optics*, 45:1943–1949, 9 1998.
- [17] S.P. Walborn, C.H. Monken, S. Pádua, and P.H. Souto Ribeiro. Spatial correlations in parametric down-conversion. *Physics Reports*, 495:87–139, 10 2010.
- [18] H. Liang, K.T. Vu, P. Krishnan, T.C. Trang, D. Shin, S. Kimel, and M.W. Berns. Wavelength dependence of cell cloning efficiency after optical trapping. *Biophysical Journal*, 70:1529–1533, 3 1996.
- [19] Keir C. Neuman, Edmund H. Chadd, Grace F. Liou, Keren Bergman, and Steven M. Block. Characterization of photodamage to escherichia coli in optical traps. *Biophysical Journal*, 77:2856–2863, 11 1999.
- [20] Steven P. Gross. [8] Application of optical traps in Vivo, pages 162–174. 2003.
- [21] Giorgio Volpe and Giovanni Volpe. Simulation of a brownian particle in an optical trap. *American Journal of Physics*, 81:224–230, 3 2013.
- [22] Manuel Pancorbo, Miguel A. Rubio, and P. Domínguez-García. Brownian dynamics simulations to explore experimental microsphere diffusion with optical tweezers. *Procedia Computer Science*, 108:166–174, 2017.
- [23] Max Born, Emil Wolf, A. B. Bhatia, P. C. Clemmow, D. Gabor, A. R. Stokes, A. M. Taylor, P. A. Wayman, and W. L. Wilcock. *Principles of Optics*. Cambridge University Press, 10 1999.
- [24] R. Paschotta. *Fourier Optics - an encyclopedia article*. RP Photonics AG, 2019.
- [25] Ashis Gopal Banerjee, Andrew Pomerance, Wolfgang Losert, and Satyandra K. Gupta. Developing a stochastic dynamic programming framework for optical tweezer-based automated particle transport operations. *IEEE Transactions on Automation Science and Engineering*, 7(2):218–227, 2010.
- [26] Hu S and Sun D. Automatic transportation of biological cells with a robot-tweezer manipulation system. *The International Journal of Robotics Research*, 30(14):1681–1694, 2011.
- [27] Eric Lauga and Thomas R Powers. The hydrodynamics of swimming microorganisms. *Reports on Progress in Physics*, 72(9):096601, 2009.
- [28] R. C. Gauthier and S. Wallace. Optical levitation of spheres: analytical development and numerical computations of the force equations. *J. Opt. Soc. Am. B*, 12(9):1680–1686, Sep 1995.
- [29] Karel Svoboda, Christoph F. Schmidt, Bruce J. Schnapp, and Steven M. Block. Direct observation of kinesin stepping by optical trapping interferometry. *Nature*, 365(6448):721–727, Oct 1993.
- [30] Yanhua Wu, Dong Sun, Wenhao Huang, and Ning Xi. Dynamics analysis and motion planning for automated cell transportation with optical tweezers. *IEEE/ASME Transactions on Mechatronics*, 18(2):706–713, 2013.
- [31] Yanhua Wu, Dong Sun, and Wenhao Huang. Mechanical force characterization in manipulating live cells with optical tweezers. *Journal of Biomechanics*, 44(4):741–746, 2011.
- [32] J W Shaevitz. A practical guide to optical trapping. *Shaevitz Lab Web Site*, 2006.
- [33] K. Visscher, S.P. Gross, and S.M. Block. Construction of multiple-beam optical traps with nanometer-resolution position sensing. *IEEE Journal of Selected Topics in Quantum Electronics*, 2(4):1066–1076, 1996.
- [34] Jing Zhao, Hui Hou, Qi-Yu Huang, Xun-Gao Zhong, and Peng-Sheng Zheng. Design of optical tweezers manipulation control system based on novel self-organizing fuzzy cerebellar model neural network. *Applied Sciences*, 12(19), 2022.
- [35] Paul Campbell David J. Stevenson, Frank J. Gunn-Moore and Kishan Dholakia. Transfection by optical injection. In V. V Tuchin, editor, *Handbook of Photonics for Biomedical Science*, chapter 3, pages 87–113. CRC Press, 210.
- [36] David J Stevenson, Frank J Gunn-Moore, Paul Campbell, and Kishan Dholakia. Single cell optical transfection. *J. R. Soc. Interface*, 7(47):863–871, June 2010.
- [37] Craig McDougall, David J. Stevenson, Christian T. A. Brown, Frank Gunn-Moore, and Kishan Dholakia. Targeted optical injection of gold nanoparticles into single mammalian cells. *Journal of Biophotonics*, 2(12):736–743, 2009.

- [38] A Vogel, J Noack, G Hüttman, and G Paltauf. Mechanisms of femtosecond laser nanosurgery of cells and tissues. *Appl. Phys. B*, 81(8):1015–1047, December 2005.
- [39] Xanthi Tsampoula. *Femtosecond Cellular Transfection using Novel Laser Beam Geometries*. PhD thesis, University of St Andrews, 2009.
- [40] Application note-variable attenuator for lasers. *Newport Corporation Web Site*, 2006.
- [41] Laser lab source. *Laser Diode Source Web Site*, 2024.
- [42] J. Baumgart, W. Bintig, A. Ngezahayo, S. Willenbrock, H. Murua Escobar, W. Ertmer, H. Lubatschowski, and A. Heisterkamp. Quantified femtosecond laser based opto-perforation of living gfshr-17 and mth53a cells. *Opt. Express*, 16(5):3021–3031, Mar 2008.
- [43] Dr. Rüdiger Paschotta. Numerica aperture. *RP Photonics Encyclopedia*, 2020.
- [44] C A Sacchi. Laser-induced electric breakdown in water. *J. Opt. Soc. Am. B*, 8(2):337, February 1991.
- [45] Muhammad Waleed, Sun-Uk Hwang, Jung-Dae Kim, Ir-fan Shabbir, Sang-Mo Shin, and Yong-Gu Lee. Single-cell optoporation and transfection using femtosecond laser and optical tweezers. *Biomed. Opt. Express*, 4(9):1533–1547, August 2013.
- [46] D. Stevenson, B. Agate, X. Tsampoula, P. Fischer, C. T. A. Brown, W. Sibbett, A. Riches, F. Gunn-Moore, and K. Dholakia. Femtosecond optical transfection of cells:viability and efficiency. *Opt. Express*, 14(16):7125–7133, Aug 2006.
- [47] Maciej Antkowiak, Maria L Torres-Mapa, David J Stevenson, Kishan Dholakia, and Frank J Gunn-Moore. Femtosecond optical transfection of individual mammalian cells. *Nature Protocols*, 8(6):1216–1233, May 2013.
- [48] Jochen Arlt, Kishan Dholakia, Josh Soneson, and Ewan M. Wright. Optical dipole traps and atomic waveguides based on bessel light beams. *Phys. Rev. A*, 63:063602, May 2001.
- [49] C A McQueen, J Arlt, and K Dholakia. An experiment to study a “nondiffracting” light beam. *Am. J. Phys.*, 67(10):912–915, October 1999.
- [50] Occupational Health and University of Cambridge Safety Service. Hsd013r (rev 5) safe use of lasers. 2016.
- [51] Public Health England. Laser radiation: safety advice. 2017.
- [52] London British Standards Institution. D iec tr 60825-14:2004. safety of laser products - part 14: A user's guide. 2004.
- [53] Christoph Greb, James DeRose, and Martin Wilson. Introduction to widefield microscopy, 2017. <https://www.leica-microsystems.com/science-lab/microscopy-basics/introduction-to-widefield-microscopy/>.
- [54] F. Zernike. Phase contrast, a new method for the microscopic observation of transparent objects. *Physica*, 9(7):686–698, 1942.
- [55] Douglas B. Murphy, Ron Oldfield, Stanley Schwartz, and Michael W. Davidson. Introduction to phase contrast microscopy, 2019. <https://www.microscopyu.com/techniques/phase-contrast/introduction-to-phase-contrast-microscopy>.
- [56] Eugene Hecht. *OPTics*. Pearson, Harlow, 2017. ISBN:978-1-292-09693-3.
- [57] P. Y. Liu, L. K. Chin, W. Ser, H. F. Chen, C.-M. Hsieh, C.-H. Lee, K.-B. Sung, T. C. Ayi, P. H. Yap, B. Liedberg, K. Wang, T. Bourouina, and Y. Leprince-Wang. Cell refractive index for cell biology and disease diagnosis: past, present and future. *Lab Chip*, 16:634–644, 2016.
- [58] Teledyne Photometrics. Phase contrast microscopy, Mar 2020. <https://www.photometrics.com/learn/microscopy-basics/phase-contrast-microscopy>.
- [59] Zhaozheng Yin, Takeo Kanade, and Mei Chen. Understanding the phase contrast optics to restore artifact-free microscopy images for segmentation. *Medical Image Analysis*, 16(5):1047–1062, 2012.
- [60] Joseph W Goodman. Introduction to fourier optics. *Introduction to Fourier optics*, 3rd ed., by JW Goodman. Englewood, CO: Roberts & Co. Publishers, 2005, 1, 2005.
- [61] Christoph Greb Martin Wilson, James DeRose. Microscope resolution: Concepts, factors and calculation. <https://www.leica-microsystems.com/science-lab/life-science/microscope-resolution-concepts-factors-and-calculation/>.
- [62] Tatsuro Otaki. Halo reduction technique in phase contrast microscopy. *Optical Review*, 8(4):284–286, 2001.
- [63] Mikhail E. Kandel, Michael Fanous, Catherine Best-Popescu, and Gabriel Popescu. Real-time halo correction in phase contrast imaging. *Biomed. Opt. Express*, 9(2):623–635, Feb 2018.
- [64] Michael W. Davidson Rudi Rottenfusser, Tadja Dragoo. Basic principles of infinity optical systems. <https://zeiss-campus.magnet.fsu.edu/mobile/tutorials/basics/-objectivemagnification>.
- [65] Nicolas Blanc. Ccd versus cmos – has ccd imaging come to an end? 12 2003.

- [66] Youngjin Yoo, Seongdeok Lee, Wonhee Choe, and Chang Yeong Kim. Cmos image sensor noise reduction method for image signal processor in digital cameras and camera phones - art. no. 65020s. *Proceedings of SPIE - The International Society for Optical Engineering*, 6502, 02 2007.
- [67] Ettore Masetti, Mario Ettore Giardini, Marco Ruggeri, and Luigi Rovati. Laplacian-based focus measure allows rapid focus estimation of annular regions in gray-scale images. In *2023 IEEE International Instrumentation and Measurement Technology Conference (I2MTC)*, pages 1–6, 2023.
- [68] Austin C. Bergstrom, David Conran, and David W. Messinger. Gaussian blur and relative edge response, 2023.
- [69] Stoyan Tanev, Valery Tuchin, and James Pond. Simulation and modeling of optical phase contrast microscope cellular nanobioimaging. *Proceedings of SPIE - The International Society for Optical Engineering*, 7027, 12 2008.
- [70] MathWorks. <https://uk.mathworks.com/help/images/detecting-a-cell-using-image-segmentation.html>.
- [71] Yuliang Wang, Zaicheng Zhang, Huimin Wang, and Shusheng Bi. Segmentation of the clustered cells with optimized boundary detection in negative phase contrast images. *PLOS ONE*, 10:e0130178, 06 2015.
- [72] T.F. Chan and L.A. Vese. Active contours without edges. *IEEE Transactions on Image Processing*, 10(2):266–277, 2001.
- [73] Si Yong Yeo, Xianghua Xie, Igor Sazonov, and Perumal Nithiarasu. Segmentation of biomedical images using active contour model with robust image feature and shape prior. *International Journal for Numerical Methods in Biomedical Engineering*, 30(2):232–248, 2014.
- [74] Gang Chen, Haiying Zhang, Iron Chen, and Wen Yang. Active contours with thresholding value for image segmentation. pages 2266–2269, 08 2010.
- [75] Stanley Schwartz Michael W. Davidson Douglas B. Murphy, Ron Oldfield. Introduction to phase contrast microscopy. <https://www.microscopyu.com/techniques/phase-contrast/introduction-to-phase-contrast-microscopy>.
- [76] Alejandro Flores-Mendez and Angeles Suarez-Cervantes. Circular degree hough transform. In Eduardo Bayro-Corrochano and Jan-Olof Eklundh, editors, *Progress in Pattern Recognition, Image Analysis, Computer Vision, and Applications*, pages 287–294, Berlin, Heidelberg, 2009. Springer Berlin Heidelberg.
- [77] David E. Benn, Mark S. Nixon, and John N. Carter. Robust eye centre extraction using the hough transform. In Josef Bigün, Gérard Chollet, and Gunilla Borgefors, editors, *Audio- and Video-based Biometric Person Authentication*, pages 1–9, Berlin, Heidelberg, 1997. Springer Berlin Heidelberg.
- [78] Carmen & Mirabelli Peppino & De Luca Anna Chiara. Managò, Stefano & Valente. Discrimination and classification of acute lymphoblastic leukemia cells by raman spectroscopy. *Proceedings of SPIE - The International Society for Optical Engineering*, 2015.
- [79] Frederic & Ameer-Beg Simon & Richards David. Littleton, Brad & Festy. Broadband coherent raman imaging for multiplexed detection. *Multiphoton Microscopy in the Biomedical Sciences Xi*, 2011.
- [80] Herman L. Offerhausb Maike Windbergsa-Cees Ottod Birthe Kanna. Raman microscopy for cellular investigations — from single cell imaging to drug carrier uptake visualization. *Advanced Drug Delivery Reviews*, 2015.
- [81] Ying Ma & Zhiwei Huang Li Gong, Wei Zheng. Higher-order coherent anti-stokes raman scattering microscopy realizes label-free super-resolution vibrational imaging. *Nature Photonics*, 2019.
- [82] Elmira Farrokhtakin Gianni Ciofani Virgilio Mattoli Vincenzo Piazza, Giuseppe de Vito. Femtosecond-laser-pulse characterization and optimization for cars microscopy. *PLOS ONE*, 2016.
- [83] Prof. Tina Potter, *Feynman Diagrams Particle and Nuclear Physics*.
- [84] Clark, S. J.; Segall, M. D.; Pickard, C. J.; Hasnip, P. J.; Probert, M. J.; Refson, K.; Payne, M. C. "First principles methods using CASTEP", *Zeitschrift fuer Kristallographie*, 220 (5-6), 567-570 (2005).
- [85] Plastic Raman Spectra. Polymer analysis using raman spectroscopy. *Physics Open Lab*, 2022.
- [86] PhD Sunil Kalia MD MHSc Harvey Lui MD Jianhua Zhao, PhD Haishan Zeng. Using raman spectroscopy to detect and diagnose skin cancer in vivo. *Dermatologic Clinics*, 2017.
- [87] Water Raman Spectra. Water molecule vibrations with raman spectroscopy. *Physics Open Lab*, 2022.
- [88] Hanna Iitti Per Stenius J. Vyörykkä, M. Halttunen. Characteristics of immersion sampling technique in confocal raman depth profiling. *Applied Spectroscopy*, 2002.
- [89] Chameleon Discovery NX Dual-Output, Widely-Tunable Femtosecond Laser Data Sheet.
- [90] Thorlabs Shortpass Dichroic Mirror/Beamsplitter: 1020 nm Cutoff Wavelength,DMSP1020B.

- [91] NFD01-1040 Searchlight, <https://searchlight.idex-hs.com/?sid=053347a5-1f78-42a0-b7d3-753018ed34f9>.
- [92] Thorlabs - DMLP650 Ø1" longpass dichroic mirror, 650 nm cut-on. <https://www.thorlabs.com>.
- [93] Nikon mrl07920 <https://www.microscope.healthcare.nikon.com/products/optics>.
- [94] König, K., Becker, T. W., Fischer, P., Riemann, I. & Halbhüter, K. J. Pulse-length dependence of cellular response to intense near-infrared laser pulses in multiphoton microscopes. *Opt. Lett.* 24, 113–115 (1999).
- [95] *PDXR1(M) Piezo Inertia Drive Rotation Stage with Optical Encoder*.
- [96] *SMALL BEAM DIAMETER SCANNING GALVO MIRROR SYSTEMS*. www.thorlabs.us/NewGroupPage9_PF.cfm?ObjectGroup_ID=3770.
- [97] Thin Lens, [https://phys.libretexts.org/Bookshelves/University_Physics/University_Physics_\(OpenStax\)/University_Physics_III_-_Optics_and_Modern_Physics_\(OpenStax\)/02_Geometric_Optics_and_Image_Formation/2.05_Thin_Lenses](https://phys.libretexts.org/Bookshelves/University_Physics/University_Physics_(OpenStax)/University_Physics_III_-_Optics_and_Modern_Physics_(OpenStax)/02_Geometric_Optics_and_Image_Formation/2.05_Thin_Lenses).
- [98] *Hamamatsu R2066 Photomultiplier tube Datasheet*.
- [99] Haiyue Zhu, Chee Khiang Pang, and Tat Joo Teo. Integrated servo-mechanical design of a fine stage for a coarse/fine dual-stage positioning system. *IEEE/ASME Transactions on Mechatronics*, 21(1):329–338, 2016.
- [100] Keysight Technologies. 10715a differential interferometer, 2024. Accessed on 19/02/24.
- [101] Q Xu. Design and development of a flexure-based dual-stage nanopositioning system with minimum interference behavior. *IEEE transactions on automation science and engineering*, 9(3):554–563, 2012.
- [102] Qingsong Xu. A novel compliant micropositioning stage with dual ranges and resolutions. *Sensors and Actuators A: Physical*, 205(1):6–14, 2014.
- [103] Science Notes. Piezoelectricity and the piezoelectric effect, 2024. Accessed on 10/04/24.
- [104] Xeryon Precision. Xla-10, 2024. Accessed on 30/01/24.
- [105] Lion Precision. Capacitive sensors, 2024. Accessed on 10/04/24.
- [106] Yangmin Li and Qingsong Xu. A novel piezoactuated xy stage with parallel, decoupled, and stacked flexure structure for micro-/nanopositioning. *IEEE Transactions on Industrial Electronics*, 58(8):3601–3615, 2011.
- [107] Xavier Herpe, Mathew Walter Dunnigan, and Xianwen Kong. Design, fabrication and testing of a dual-range xy micro-motion stage driven by voice coil actuators. *Advances in Science, Technology and Engineering Systems Journal*, 2(3):498–504, May 2017.
- [108] Henning S Linß S and Zentner L. *Kinematics - Analysis and Applications*, chapter Modeling and Design of Flexure Hinge-Based Compliant Mechanisms. IntechOpen, 2019.
- [109] Yanling Tian Dawei Zhang Yanding Qin, Bijan Shirinzadeh. Design issues in a decoupled xy stage: Static and dynamics modeling, hysteresis compensation, and tracking control. *Sensors and Actuators A: Physical*, 194:95–105, 2013.
- [110] Yangmin Li, Jiming Huang, and Hui Tang. A compliant parallel xy micromotion stage with complete kinematic decoupling. *IEEE Transactions on Automation Science and Engineering*, 9(3):538–553, 2012.
- [111] Xeryon. Crossfixx™ piezo motor, 2024. Accessed on 12/02/24.
- [112] Mouhanned Brahim. *Modeling and Position Control of Piezoelectric Motors*. PhD thesis, Université Paris Saclay (COmUE), 2017.
- [113] Roel J. E. Merry, Niels C. T. de Kleijn, Marinus J. G. van de Molengraft, and Maarten Steinbuch. Using a walking piezo actuator to drive and control a high-precision stage. *IEEE/ASME Transactions on Mechatronics*, 14(1):21–31, 2009.
- [114] Emerson. The pid controller & theory explained, 2024. Accessed on 12/02/24.